UTS UNIVERSITY OF TECHNOLOGY SYDNEY

# Research on control systems for high-speed, high-overload permanent magnet synchronous motors

**by Hongtai Ma**

Thesis submitted in fulfilment of the requirements for the degree of

**Doctor of Philosophy**

under the supervision of A/Prof. Li Li and Prof. Youguang Guo

University of Technology Sydney
Faculty of Engineering and Information Technology

03/2025

# Certificate of Original Authorship

I, Hongtai Ma, declare that this thesis is submitted in fulfilment of the requirements for the award of Doctor of Philosophy, in the School of Electrical and Data Engineering, Faculty of Engineering and Information at the University of Technology Sydney.

This thesis is wholly my own work unless otherwise referenced or acknowledged. In addition, I certify that all information sources and literature used are indicated in the thesis.

I certify that the work in this thesis has not previously been submitted for a degree nor has it been submitted as part of the requirements for a degree at any other academic institution except as fully acknowledged within the text. This thesis is the result of a Collaborative Doctoral Research Degree program with Shanghai University.

This research was supported by an Australian Government Research Training Program (RTP) Scholarship doi.org/10.82133/C42F-K220.

Signature: Production Note:
Signature removed prior to publication.

Date: 12/01/2025

# ACKNOWLEDGEMENT

At the completion of this thesis, I would like to express my heartfelt gratitude to all the teachers, classmates, and family members who have supported and helped me throughout this journey.

First and foremost, I extend my deepest thanks to my supervisor, A/Prof Li. A/Prof. Li's broad academic vision, rigorous scholarly attitude, and dedication to hard work have greatly benefited me. Throughout the research process, A/Prof. Li provided me with patient guidance, professional advice, and thoughtful support, enabling me to overcome challenges, break through bottlenecks, and continuously improve. His generosity in sharing his expertise and extensive engineering experience has had a profound impact on my academic growth.

Moreover, I would like to express my sincere gratitude to my principal supervisor, Prof Jian Luo at Shanghai University. Prof. Luo provided me with the opportunity for collaborative training at UTS and showed great care for my life in Australia. I am also deeply grateful to him for his invaluable advice on my future career development.

Besides, I would like to thank our team members Jiexiang Wu, Forrest Lin, Tianling Shi and Jiwen Qi, for their assistance in both academic projects and daily life. The discussions and exchanges with them broadened my horizons, and the days we spent studying and working together were both enriching and joyful.

Finally, I owe my deepest gratitude to my parents, who have been a constant source of encouragement and support throughout this arduous and long academic journey. Their care and support allowed me to focus on my research and successfully complete my studies.

# List of Publications

**Journal:**

Ma H, Li L, Fan Y, et al. A discrete current controller for high power-density synchronous machines[J]. Energies, 2022, 15(17): 6396.

Ma H, Li L, Fan K, Guo Y, et al. A Novel Programmed Hybrid Modulation for EMI Mitigation and Current Ripple Control in Miniaturized Synchronous Machine Drives[J]. IET Electric Power Applications, 2024,1-16.

**Conference:**

Ma H, Luo J, Fan Y, et al. A traction control arithmetic verified on a novel HIL platform[C]//2018 Australian & New Zealand Control Conference (ANZCC). IEEE, 2018: 145-147.

**Collaborative works:**

Luo Y, Ma H, Xu G, et al. A new type of motor load model for vehicle TCS/ABS test[C]//2017 IEEE International Conference on Information and Automation (ICIA). IEEE, 2017: 165-170.

Fan Y, Ma H, Zhu G, et al. Improved MTPA and MTPV Optimal Criteria Analysis Based on IPMSM Nonlinear Flux-Linkage Model[J]. Energies, 2024, 17(14): 3494.

# List of Acronyms

ADC (Analog to Digital Converter)

AZSPWM (Active Zero State PWM)

CAN (Controller Area Network)

CCS (Code Composer Studio)

CE (Conducted Emission)

CM (Common Mode)

CMTI (Common Mode Transient Immunity)

CMV (Common Mode Voltage)

CSFPWM (Constant Switching Frequency PWM)

CVC (Complex Vector Controller)

DIMC (Diagonal Internal Model Control)

DM (Differential Mode)

DMA (Direct Memory Access)

DPWM (Discontinuous PWM)

DSDU (Dual Sampling and Dual PWM Duty Ratios Updating)

FFT (Fast Fourier Transform)

IA (Impedance Analyzer)

IGBT (Insulated Gate Bipolar Transistor)

IMC (Internal Model Control)

JTAG (Joint Test Action Group)

LISN (Line Impedance Stabilization Networks)

MAZSPWM (Modified AZSPWM)

MTPA (Maximum Torque Per Ampere)NA (Network Analyzer)

NSPWM (Near State PWM)

SISO (Single Input Single Output)

SSSU (Single Sampling and Single PWM Duty Ratios Updating)

VSFPWM (Varying Switching Frequency PWM)

# List of Tables

# List of Figures

# Abstract

Battery-powered intelligent equipment has stringent power density requirements for power electronic drive systems. The design of high-power density equipment poses significant challenges to the current loop and electromagnetic interference performance of motors. Under high-intensity magnetic fields, the motor core will experience saturation, and the combined effect of motor slots introduces nonlinearity to the motor model. The classic linear control of motors at high speeds would result in decoupling failure of the current loop control and even decreased stability. Moreover, the utilization of wide-bandgap devices and dense layout wiring can worsen the electromagnetic environment, thereby reducing system reliability.

The main research objectives and innovative contributions of this thesis are as follows:

1) For permanent magnet synchronous motors, a nonlinear model based on data considering cross-coupling and slotting effects is established, and a distributed parameter high-frequency system model is developed for the drive system.

2) The latch and delay of inverters in digital control systems are modeled. Based on the model, a flux-based complex vector controller is proposed based on the motor's nonlinear model to improve the bandwidth and stability of saturated motors under low modulation ratio.

3) Harmonics analysis is performed for active zero vector pulse width modulation and near state pulse width modulation. Then, a hybrid spread spectrum modulation method is proposed based on the motor's nonlinear model, which could extend the current spectrum, maintain current harmonics, and reduce electromagnetic conducted emission.

4) To validate the proposed control strategies, an experimental prototype is designed and fabricated. The prototype adopts a layered design, resembling the shape of the motor, allowing heat dissipation through the motor casing to reduce volume and weight. Additionally, a set of control software is developed, and human-machine interface software is written to control the high-power density motor developed in the laboratory, verifying the effectiveness of the proposed highly saturated permanent magnet synchronous motor current control and spreading control algorithms.

These innovative contributions enhance the control performance of high-power density power electronic drive systems, mitigate electromagnetic interference to external systems, and improve the stability and reliability of the system itself. This research significantly contributes to the enhancement of power density in battery-powered power electronic devices, such as electric vehicles, biomimetic robots, and electric aircraft.

**Keywords**: Cross-Saturation; Slotting Effects; High-Frequency Model; Complex Vector Control; Spread Spectrum

# Table of Contents

# Chapter 1: Introduction

## 1.1 BACKGROUND

With the continuous advancement of power electronics and modern control theory, coupled with the increasing maturity of motor manufacturing processes and significant improvements in battery performance, motors, as core energy conversion devices, have found increasingly widespread applications in electric drive systems such as electric vehicles, electric aircraft, and bionic robots. In scenarios where space is limited, weight is minimized, and cost control is critical, the power density of electric drive systems becomes a key consideration. This has driven current research to focus on the miniaturization, high-speed operation, and high-overload capacity of motors and inverters.

Compared to the response times of approximately 100–500 milliseconds in electronic fuel injection and hydraulic braking systems of traditional internal combustion engine vehicles, motor-driven and auxiliary braking systems can reduce response times to 1% of the original duration. This improvement allows for significantly more effective control of vehicle dynamics and safety, attracting widespread attention [1-2]. During rapid acceleration, it is essential to maximize the utilization of tire-ground contact force while maintaining vehicle stability. This requires not only maintaining high torque output but also achieving precise and rapid torque control. For distributed-drive vehicles, which lack a differential, there are even stricter requirements for power distribution to the steering wheels [3-4].

For instance, BYD's distributed-drive electric vehicle, Yangwang U8, showcases advanced applications of this technology. Equipped with four wheel-hub motors, each providing a maximum output of 220 kW and 320 Nm of torque, the system achieves a total power output exceeding 1,195 horsepower, enabling 0–100 km/h acceleration in just 3.6 seconds. The ‘e4’ platform utilizes independent vector control for each motor, allowing precise torque control at 1,000 Hz. This technology enables the vehicle to rapidly adjust the torque of the remaining wheels in the event of a single tire blowout, helping the driver stabilize the vehicle. Even after a blowout, the vehicle can maintain a speed of 120 km/h for a short duration, significantly reducing the risk of secondary accidents.

Electric aircraft have been widely applied in industrial inspections, agricultural operations, firefighting, and parcel delivery, becoming indispensable in modern life. Among these, multirotor drones, due to their vertical takeoff, landing, and hovering capabilities, are the most extensively used. Leading domestic companies such as DJI and Autel Robotics dominate this field [5-6]. However, extreme weather conditions or collisions with obstacles may still lead to drone failures or crashes, resulting in personal injury or property damage. To achieve emergency landing or limp flight in the event of single-motor failure, the functioning motors must possess sufficient overload

capacity and responsiveness to provide necessary lift and maintain stability by adjusting roll, pitch, and yaw angles [7-8].

On the other hand, bionic robots, as advanced forms of intelligent robots, represent the deep integration of biology and robotics [9]. Compared to wheeled and tracked robots, bionic robots can navigate complex terrains and have broad applications in high-risk environments such as space exploration, military reconnaissance, and disaster rescue. Boston Dynamics leads this field with its Atlas humanoid robot, which achieves hip joint torque of up to 840 Nm through an advanced hydraulic system. However, hydraulic systems are associated with high noise, leakage risks, and cost. In contrast, semi-direct drive systems using joint motors combined with planetary gear reducers or harmonic drives offer lower costs, higher control precision, and transmission efficiency [10]. In such systems, motor controllers and motors function as the "heart" and "muscles" of the robot, serving as key components of the robot's power system. They must meet short-term high overload demands during actions like jumping and obstacle crossing [11].

In summary, whether in scenarios such as emergency acceleration or high-speed blowout of electric vehicles, dual-axis lockup failure in electric aircraft, or obstacle crossing by bionic robots, electric drive systems under extreme conditions require motors to operate at high speeds within a short time frame and withstand overloads exceeding three times their rated torque. Considering the saturation effects on torque output, the current overload factor may be even higher. When the motor operating point is on the right side of the knee of the magnetic material characteristic curve, inductance values significantly decrease [12]. Additionally, high rotational speeds reduce the decoupling effect of currents. Traditional current control methods struggle to adapt to parameter variations and inverter output delays, thereby affecting dynamic response and stability in current control.

In the pursuit of miniaturization and lightweight design of electric drive systems, challenges extend beyond motor core saturation to include the deteriorating electromagnetic environment of motor controllers. Firstly, the application of wide-bandgap switches with high voltage tolerance and low losses significantly increases the dV/dt, exacerbating high-frequency electromagnetic interference (EMI) emissions from inverters. Secondly, the compact layout of components, laminated PCB designs, and high-density wiring, commonly adopted for lightweight and compact designs, provide pathways for crosstalk within the controller. Additionally, the trend towards distributed drive architectures, which reduce the weight of EMI filters and shielding enclosures, further intensifies electromagnetic interference with peripheral devices. Finally, the high standards for performance, comfort, and safety necessitate a large number of integrated circuits in electric drive systems, increasing the number of sensitive devices. These factors collectively pose new challenges for electromagnetic compatibility (EMC) design.

In motor design, high-speed and high-torque motors are two technical directions to improve power density. To increase torque density, optimization of the magnetic circuit design and the use of non-saturable magnetic materials such as amorphous silicon steel can be employed to increase the stator’s flux linkage density, thereby obtaining greater permanent magnet torque and reluctance torque [13,14]. In the past, the use of materials with low magnetic energy density, such as magnetite, aluminium-nickel-cobalt, and ferrite, resulted in a large volume of PMSMs. However, with the application of new rare-earth materials such as samarium-cobalt and neodymium-

iron-boron, the rotor volume of permanent magnet motors has been significantly reduced, thereby promoting the widespread use of PMSMs. Various approaches can be implemented to increase the speed, such as increasing the mechanical strength of the rotor, enhancing the fixation of the permanent magnet and winding, reducing high-frequency harmonic losses and eddy current losses, and using high-speed bearings [15,16].

Regarding controlling high-speed operating machines, current loop performance deteriorates with the speed increase due to the computation and modulation delays. In order to improve the stability of the current loop controller at high speed, the time-lag issue can be addressed by improving the switching frequency and sampling frequency. However, the switching frequency and sampling frequency have limitations due to switching losses and computing resources, and they cannot be increased indefinitely. One solution is dual current sampling and dual pulse width modulate duty ratio update (DSDU) mode. Compared to synchronous single current sampling and single pulse width modulate duty ratio update (SSSU) control mode, synchronous DSDU is able to double the sampling frequency without increasing the switching frequency [17]. Modelling the sampling-updating time lag to develop a more accurate controller is another solution [18,19]. Predictive control systems, such as deadbeat control and finite control set model, can also deal with the high-speed operation mode [20]

At the same time, the dq-frame machine model introduces a speed-proportional cross-coupling term, which deteriorates the control performance. Incomplete decoupling can cause current oscillation and even instability, particularly in high-speed regions. Various decoupling methods, such as feedforward, feedback, and complex vector decoupling, have been developed to achieve better results. However, all these decoupling methods rely on accurate d-q flux parameters. In peak-torque mode, the current is several times the rated value, resulting in the parameter change. When motors work beyond the knee point, the saturation of iron cores will significantly reduce inductance, leading to excessive cross-coupling compensation.

Modern and intelligent control methods have been developed to address time-varying and nonlinear problems posed by saturation. Adaptive control [21], sliding mode control [22,23], fuzzy control, and artificial neural network control [24], have been proposed for handling these issues without requiring precise model parameters, although their effectiveness may have limitations.

The internal model control (IMC) principle uses the inverse of the plant model and a low-pass filter to design the controller. The only tuning parameter is the filter bandwidth, making the control system easy to design. When the inductance and resistance are known, the response follows the instruction, and the system can be regarded as an open-loop control system. Nevertheless, the response will deteriorate when the inductance and resistance are inaccurate. It may even result in divergence when the magnetic circuit is highly saturated. In engineering practice, piecewise linearization is frequently adopted. The IMC controller parameters depend on the current interval partitioned for linearization. However, there is no theoretical support for choosing the partition, and it is difficult to guarantee system stability. Thus, to guarantee the control performance, IMC should be based on an accurate model and appropriate parameter selection.

The concept of the complex vector was first introduced by Waldo V. Lyon in 1954 as a coordinate transformation. It has been expanded for modelling of nonsalient machines to simplify voltage equations. The

complex vector model transfers the multiple inputs multiple outputs (MIMO) system into a single input single output (SISO) system, with which the classical analytical tools of root locus and frequency response can be applied. However, both complex vector control and IMC require accurate motor models for their implementation.

Similar to motor miniaturization, downsizing of inverters can also result in performance degradation [25,26]. With the increased power levels, the electromagnetic emission power of various electronic devices is also increasing. At the same time, with the annual 10% cost reduction of wide bandgap devices such as SiC/GaN [27], high-speed devices will be more widely used in products. Wide-band-gap devices exhibit characteristics such as high breakdown voltage, low on-resistance, high switching speed, and high operating temperature. The application of wide-band-gap devices can improve inverter efficiency, reduce thermal management pressure, and decrease inverter volume. The widening of the emission frequency band caused by the increased switching speed makes the impact of parasitic parameters on reliability more prominent. Furthermore, to achieve greater control flexibility, these devices often employ distributed drive architectures. At the same time, due to the performance characteristics of energy storage components, the power density within the power chain is further escalating. This is compounded by stacked design, dense layouts and wiring configurations, as well as the reduced volume of electromagnetic interference filters and shielding. All these factors contribute to increased system sensitivity. Consequently, these aspects present challenges to the existing electromagnetic compatibility design of power electronics equipment.

The three elements of EMC are classified as the source, propagation path, and susceptible equipment, as shown in Figure 1.1. Therefore, there are three approaches to prevent interference: (1) suppress the emission at the source, (2) make the propagation path ineffective as much as possible, and (3) make the susceptible equipment insensitive to EMI [28].

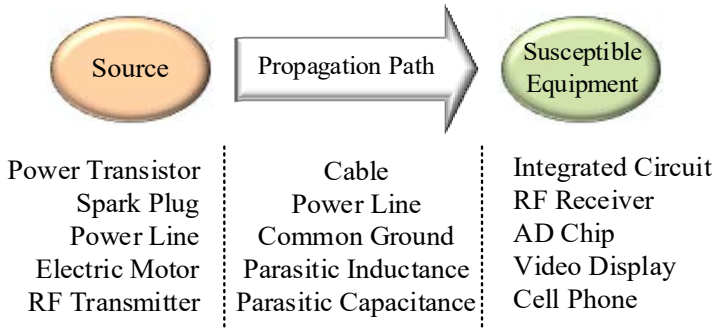


Figure 1.1 Examples of the three elements of electromagnetic compatibility.

To enhance electromagnetic immunity for vulnerable devices, several techniques can be employed. These include substituting common-mode analog signals with differential digital signals, optimizing circuit layouts, and utilizing decoupling capacitors. However, it is important to note that product designers may not always be able to prevent the occurrence of susceptible equipment. Therefore, the two main approaches are to suppress interference at the source and block propagation paths, as illustrated in Figure 1.2.

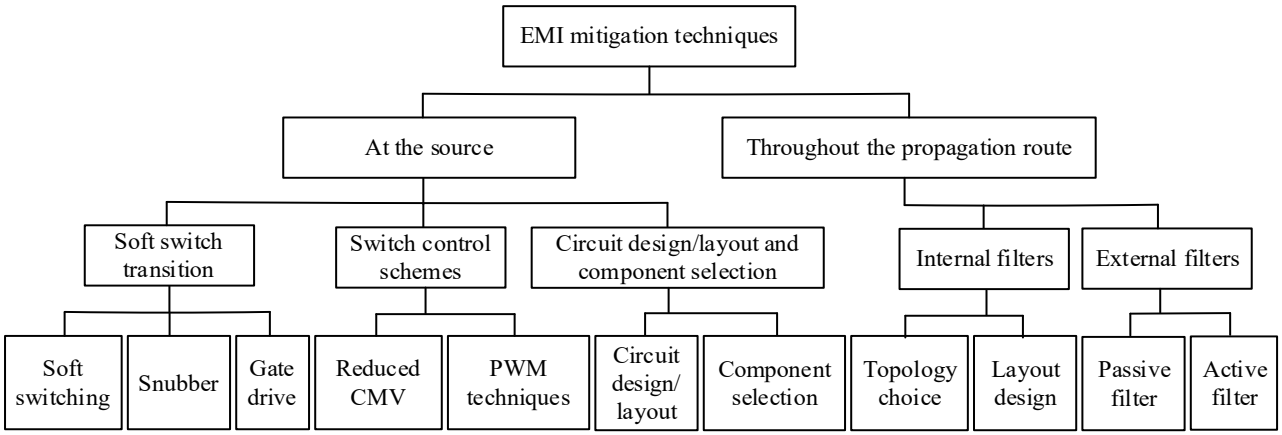


Figure 1.2 Categorization of suppressing electromagnetic interference techniques.

There are two types of coupling paths: conducted coupling and radiated coupling. For the convenience of analysis and filter design, conducted interference can be further divided into common mode interference and differential mode interference. During the rectification process, the differential and common mode signals can be separated, and the filters can be designed to block conducted coupling paths effectively. To prevent coupling in the radiated path, device shielding and grounding is a commonly used technique.

Compared to susceptible devices and propagation paths, controlling the interference source is particularly important as the 'first line of defense' [29]. Generally speaking, noise sources can be classified into three categories based on their frequency characteristics. The first category consists of pulse sequences, with a time scale around above microseconds. The second category is determined by the current and voltage step slope and falls within the mid-frequency range, with a time scale usually below microseconds. The third category encompasses high-frequency components caused by transient oscillations when switch devices are turned on and off, with a time scale usually in the tens of nanoseconds, which is especially prominent when employing wide-band banned power electronic devices [30].

To mitigate the emission intensity of noise sources, various hardware measures can be employed, e.g., reducing the switching speed, using snubber circuits/soft switching, and adopting new topologies such as inverters with auxiliary legs. On the other hand, software measures can be used to address noise emissions, such as removing zero vectors to reduce CM voltage and changing the switching frequency. The technique of changing the switching frequency is also known as spectrum spreading technology, which is effective in practice.

## 1.2 RESEARCH OBJECTIVES

(1) Investigating control algorithms addresses performance degradation in current and torque control under high overload conditions, ensuring precise and efficient motor control. This research also focuses on

improving the stability and reliability of motor operation under high-speed scenarios, aiming to optimize system output performance and dynamic response capability.

(2) Designing a miniaturized controller with optimized control algorithms to minimize electromagnetic interference, reduce motor current fluctuations and harmonics, and improve power density and system reliability.

(3) Overcoming challenges such as motor core saturation and electromagnetic compatibility, providing theoretical and technical support for the miniaturization of future electric drive equipment.

## 1.3 THESIS OUTLINE

This dissertation focuses on the control of high-speed and high-overload electric drive systems. The research encompasses mathematical model derivation, theoretical analysis, computer simulations, and experimental studies to investigate nonlinear current control of high-overload motors and electromagnetic interference suppression in high-speed, high-overload electric drive systems. The research approach outline is shown in Figure 1.3.

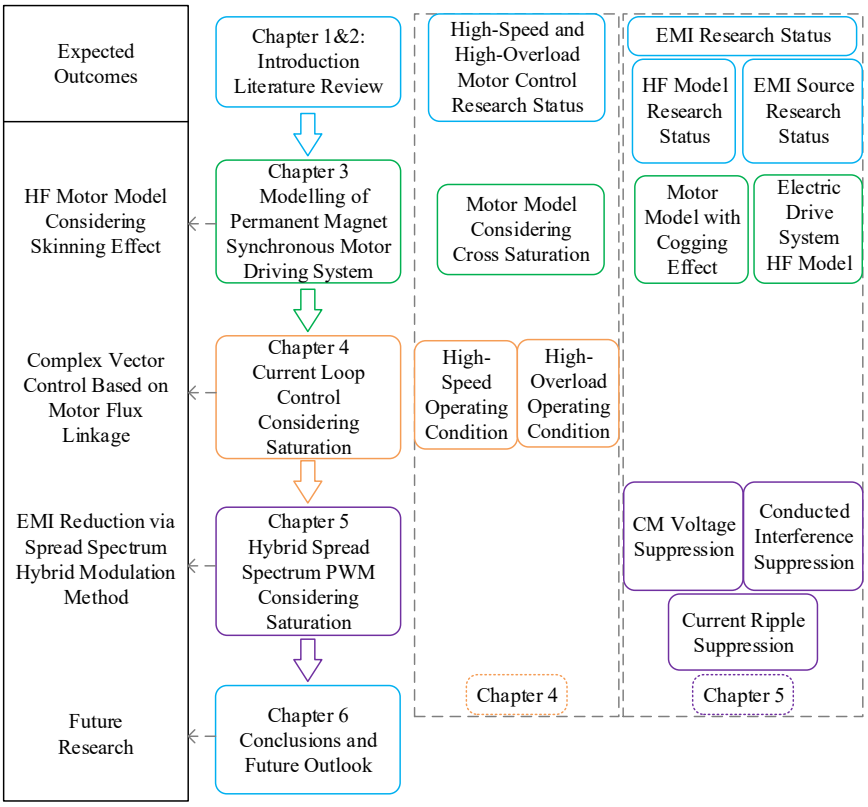


Figure 1.3 Research approach outline.

Chapter 3 presents the modeling work for high-speed, high-overload permanent magnet synchronous motor drive systems. To address current loop control under high-overload conditions, a nonlinear motor mathematical model that considers cross-saturation is established. Additionally, to tackle current harmonics caused by common-mode voltage reduction modulation, a nonlinear motor model that accounts for slotting effects is

developed. A high-frequency model of the drive system is constructed to investigate EMI issues due to controller miniaturization, and a high-frequency motor model that considers the skin effect is proposed.

Chapter 4 provides an in-depth analysis of the impact of sample-output delay on inverter output voltage under high-speed conditions. The influence of cross-saturation on the internal model-based controller under high-overload conditions is discussed, highlighting the limitations of designing frequency-domain internal model current controllers using classical control theory for high-overload operations. A complex vector control algorithm based on flux linkage data is proposed, with compensation for amplitude and phase errors due to controller output delays. Simulation results demonstrate that the proposed discrete complex vector controller based on flux linkage data significantly enhances current loop bandwidth and extends the stable operating range, making it particularly suitable for high-speed and high-overload PMSM control. Experiment confirms the effectiveness of the proposed current control method under conditions of locked-rotor high overload, high-speed light load, and high-speed high overload. Compared to the proportional-integral controller based on the internal model, the proposed discrete complex vector controller achieves higher bandwidth, better decoupling performance, effectively expands the stable output range of peak current, and increases the maximum stable output power by 39% under high-speed conditions.

Chapter 5 analyzes the flux linkage ripple patterns of SVPWM, DPWM, AZSPWM, and NSPWM, deriving the calculation formula for the normalized RMS value of flux linkage ripple within sub-switching cycles. Based on this formula, a spread spectrum hybrid modulation algorithm is proposed. After analyzing the nonlinear characteristics of the voltage equation of high-overload motors and their impact on current ripple, a hybrid spread spectrum modulation algorithm considering motor saturation and slotting effects is proposed. Simulation results indicate that the proposed method effectively suppresses common-mode voltage, reduces current harmonic distortion, mitigates current ripple caused by motor saturation, and lowers EMI common-mode conducted current. Finally, an EMI testing platform was established in accordance with GJB-151B CE102 standards to experimentally verify the proposed spread spectrum control algorithm for high-overload PMSM. Experimental results show that the proposed method has low computational complexity, demonstrates significant harmonic suppression, and reduces EMI conducted current peak by approximately 13 dB.

Chapter 6 summarizes the main contributions and work of this thesis and provides an outlook for future research.

# Chapter 2: Literature Review

To address challenges related to current control and electromagnetic interference (EMI) caused by the miniaturization and lightweighting of electric drive systems, approaches such as system modeling, current loop optimization, and PWM modulation techniques for common-mode voltage suppression are essential. This chapter provided a comprehensive review of these methods, demonstrating how they collectively enable the achievement of low harmonic distortion, high bandwidth, and reduced EMI. These advancements play a critical role in enhancing the operational efficiency and performance of devices such as electric vehicles, electric aircraft, and bionic robots.

## 2.1 CURRENT LOOP CONTROL

In battery-powered automated devices, motor control systems should be able to work at high-speed and peak-torque operating modes shortly to provide higher output power, which presents a challenge in the design of the current loop.

For the high-speed operating mode, the current loop performance deteriorates with the speed increase due to the computation and modulation delay. In order to improve the stability of the current loop controller at high speeds, the time-lag issue can be addressed by improving the switching frequency and sampling frequency. Compared to synchronous single current sampling and single pulse width modulate duty ratio update control mode, synchronous dual current sampling and dual pulse width modulate duty ratio update is able to double the sampling frequency without increasing the switching frequency [31].

Essentially, switching frequency and sampling frequency are limited by switching loss and computing resources. Modeling the sampling-updating time lag so as to develop a more accurate controller is another solution [32-33]. Predictive control systems such as deadbeat control and finite control set model can also deal with the high-speed operation mode [34,35,36].

At the same time, the dq-frame machine model introduces the cross-coupling term, which deteriorates the control performance. Incomplete decoupling can cause current ringing and even instability, especially in high-speed regions. There are feedforward decoupling, feedback decoupling, and complex vector decoupling, which achieve a better effect [37]. Taking saturation into consideration, all of these decoupling methods depend on precise d-q flux parameters.

However, in peak-torque mode, the current is several times the rated value, resulting in the parameter change. When motors work beyond the knee point, the saturation of iron cores will lead to severe inductance reduction [38]. Additionally, stator resistance and permanent magnet flux vary with temperature. These parameter mismatches will influence the stability and fast response of the current loop.

Many modern or intelligence control methods are capable of dealing with time-varying and nonlinear problems caused by saturation. For example, adaptive control, sliding mode control, fuzzy control, and artificial

neural network control work well without requiring the exact model parameters. Since the 1960s, adaptive control has been well developed. By adaptive law, which can be proved Lyapunov stable, the parameter in the controller is tuned in real time. It can deal with feedback errors and parameter changes, but the computation is extensive, and the convergence rate cannot be guaranteed. Hence, it is not suitable for the rapidly changing current loop [39,40]. Fuzzy control uses fuzzy logic and experts' experience rather than specific parameters and a detailed model. It realizes robust controllers in certain nonlinear circumstances. However, it relies too much on engineers' experience, which may be inaccurate [41]. The widely used sliding mode control changes the control loop structure to make the error signal converge to zero. It does not require specific model parameters and can achieve high robustness and good dynamics. However, the current chattering in steady state is severe [42,43].

There are also some control methods based on machine parameters. A unifying review of the internal model control type schemes was published by Garcia and Morari first in 1982. The IMC principle uses the inverse of the plant model and a low-pass filter to design the controller. The only tuning parameter is the filter bandwidth, making the control system easy to design. When the inductance and resistance are known, the response follows the instruction, and the system can be regarded as an open-loop control system. Nevertheless, the response will deteriorate when the inductance and resistance are inaccurate. It may even result in divergence when the magnetic circuit is highly saturated [44,45]. IMC can also be applied to nonlinear and time-variant systems. However, it involves seeking analytically the inverse of those plant models, and it contains higher-order derivatives and is therefore sensitive to noise and numerical errors. Hence, it cannot provide a satisfactory outcome [46].

In engineering practice, piecewise linearization is frequently adopted. The IMC controller parameters depend on the current interval partitioned for linearization. However, there is no theoretical support on how to choose the partition, and it is difficult to guarantee the system stability. Essentially, IMC is based on the accurate model and appropriate parameters [47].

The concept of complex vector control was regarded as a coordinate transformation initially. The successive scholars expanded it to model nonsalient machines, which simplify voltage equations [48]. The complex vector model transfers the multiple input multiple output system into a single input single output system, with which the classical analytical tools of root locus and frequency response can be applied [49].

As for machines with salient poles, such as synchronous reluctance motors and interior permanent magnet synchronous motors, they can be modeled using flux vector state variables to replace the current vector ones due to their naturally symmetric characteristic. This modeling method can achieve good control performance even for high-saliency machines [50,51].

In summary, based on the current state of research on current loop control, significant challenges remain, whether in error modeling caused by inverter sampling and output delays or in achieving precise decoupling of motor cross-saturation effects. These challenges are particularly pronounced under high-speed and high-overload operating conditions, adversely affecting the performance of current controllers. Accurate modeling of the motor and controller, coupled with the design of high-performance control strategies that account for cross-saturation and discrete delays, is key to improving system bandwidth and stability under such demanding conditions.

## 2.2 PWM METHODS WITH LOW ELECTROMAGNETIC INTERFERENCE

Various techniques can be employed to suppress EMI emissions at the source, and one such method involves optimizing the hardware design of the system. In the case of motor drive systems with distributed parasitic parameters, as shown in Figure 2.1, several measures can be taken to reduce EMI emissions at the source. These include modifying the circuit topology, selecting suitable switching transistors and insulating pads, strategically arranging components in the circuit, optimizing power circuit routing, and grounding cables and heat sinks.

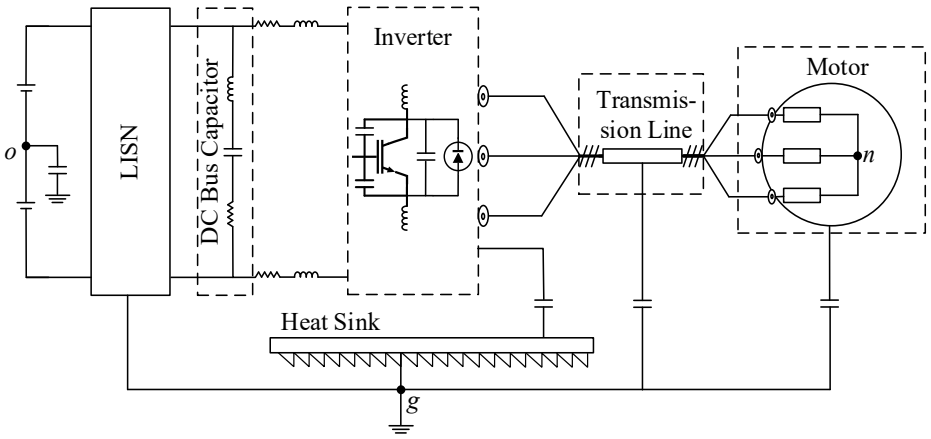


Figure 2.1 Hardware configuration and parasitic parameter distribution of motor drive systems.

In addition to hardware optimization, parameter optimization of the drive circuit can also be used to reduce EMI emissions. For example, changing the gate resistance can alter the switching speed of the switching transistors; using an RC snubber circuit or a soft switch can optimize the transient waveform of the turn-on/turn-off process; and using an active gate drive circuit with negative feedback can accurately control the waveform of the driving signal. All of these techniques can effectively reduce EMI emissions at the source [52].

Moreover, software optimization is a cost-effective method to reduce EMI emissions at the source [53]. As shown in Figure 2.2, software optimization can be broadly categorized into two types: spreading the spectral and reducing the common mode voltage amplitude. Pulse width modulation adjusts the duty cycle and outputs a high-frequency square wave to make the output voltage vector follow the reference value. According to the principle of area equivalence, a fixed duty cycle $D = \alpha_k/T_k$ ensures that the average output voltage remains constant, while the pulse position $\varepsilon_k$ and the carrier period $T_k$ can vary within a certain range without affecting the output voltage. Changing the pulse position and the carrier period can alter the current ripple and the output voltage spectrum [54,55,56]. Modulating the carrier period of PWM while keeping the pulse position unchanged is a potential method that does not affect the symmetry of the output voltage pulse.

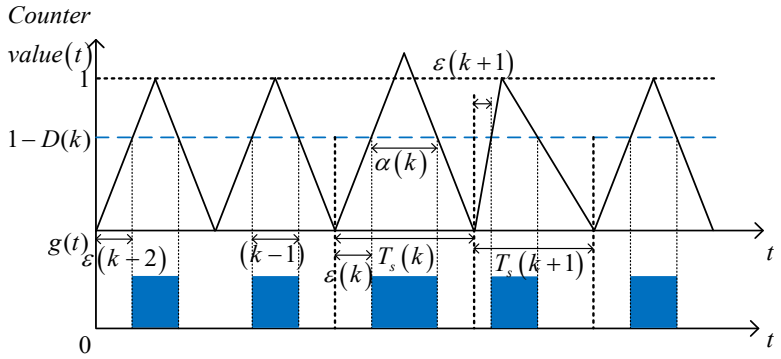


Figure 2.2 The two degrees of freedom of the modulation signal.

As shown in Figure 2.3, based on the method used to determine the carrier frequency, variable frequency modulation methods can be classified into four categories: random PWM, periodic PWM, chaos PWM, and programmed PWM [57].

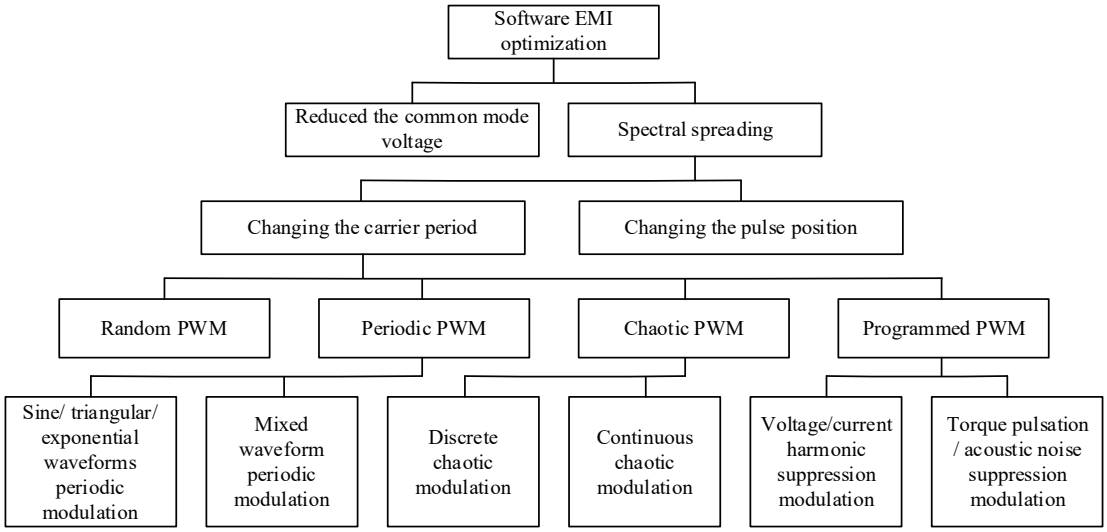


Figure 2.3 Classification of software-based EMI emission suppression methods.

Random PWM was first proposed by Andrzej M. Trzynadlowski and Stanislaw Legowski in 1987, which generated carrier waves of variable switching frequency using analog circuits. At present, the technology for random PWM is relatively mature [58,59].

Periodic PWM generates the carrier frequency by using a periodically varying function, avoiding the problem of generating pseudo-random numbers in digital circuits, and it is easy to implement. Common periodic carrier frequency functions include sine, triangular, exponential waveforms, and a mixture of the above three functions [60,61].

Chaotic PWM uses the chaotic algorithm to produce switching frequency and can be categorized into discrete chaotic modulation and continuous chaotic modulation. The carrier frequency of chaotic PWM possesses sufficient randomness, yet there is currently no standard for accurately measuring the spectrum distribution

characteristics. In addition, the performance, loss, and stability analysis of the chaotic PWM-based power converter still needs further research [62,63].

The programmed PWM utilizes the mathematical model of the controlled object to predict the control effect. It optimizes control by changing the switching frequency. It can effectively use the changing of the switching frequency to improve equipment performance. For example, the programmed PWM can suppress the inverter losses, output current ripple, motor noise, and torque pulsation [64,65].

The programmed PWM modulation can improve control performance by using additional degrees of freedom. Jiang D and Wang F analyzed the typical pattern of voltage ripple in [66] and calculated the average and maximum load current values using voltage equations in the three-phase stationary coordinate system, duty cycle, and load inductance. The research used variable switching frequency to maintain the average or peak current ripple value while reducing the number of switching actions and, thus, inverter switching losses. In addition, this method can also reduce the peak value of the EMI emission spectrum in the frequency domain. Ref. [67] used the torque equation of a permanent magnet synchronous motor to calculate the torque ripple and proposed variable switching frequency PWM (VSFPWM) to reduce motor torque ripple. The results of simulation and experiments showed that this method could decrease the average switching frequency and maintain the same motor torque ripple as when using constant switching frequency PWM (CSFPWM).

Fei Yang, Taylor A R, et al. derived the current ripple of a saturated salient pole motor using voltage equations in the synchronous rotating coordinate system in [68]. They stabilized the current ripple by using variable switching frequency. However, this method requires substantial integration calculation, which introduces integration errors and significantly increases computational complexity, making it challenging to implement with conventional control microchips.

Ref. [69] considers the saturation of powder cores-based inductors and their impact on the current ripple in grid-connected inverters. The relationship between three-phase static inductance and the current was utilized to adjust the switching frequency. Simulation and experiments confirmed the significant role of inductance variation in the current ripple analysis, which should be considered in the design of VSFPWM. Ref. [70]found a decrease in the current loop bandwidth caused by variable switching frequency and variable sampling frequency. The impact of the latching effect on current decoupling in the $DQ$-axis digital control of the inverter was analyzed. Then, a compensation method for eliminating the varying phase lag of output voltages was proposed, which reduced the six times grid frequency current ripple and finally improved dynamic and steady-state performance.

Ref. [71] studied the ripple of electromagnetic torque, ignoring the ripple of reluctance torque, and adopted the frequency modulation PWM (FMPWM). The study found that the torque ripple control effect deteriorated when the surface-mounted motor operated in the flux-weakening region, and the reason for the instability of the PI regulator in the flux-weakening region was identified. The authors designed a penalty function to characterize the system's stability. They used a genetic algorithm to optimize the design of the PI regulator, achieving satisfactory torque ripple for the studied surface-mounted permanent magnet synchronous motor under a high modulation index.

Ref. [72] investigated the effectiveness of reducing the acoustic noise of asynchronous motors by varying the switching frequency. The motor current and acoustic noise of conventional space vector PWM (CSVPWM)

and VSFPWM were extensively measured. It was confirmed that VSFPWM technology could spread the current and acoustic noise spectrum and reduce the magnitude of the dominant acoustic noise components. It was also found that random pulse positioning is not effective in high-speed regions. To solve this problem, the periodical variable switching frequency was improved to avoid harmonics in the narrow band around the integral multiples of the switching frequency. The proposed algorithm reduced the dominant noise components without significantly increasing the computational burden.

In [73], Chang L and Jahns T M suggested that the above method only applies to power electronics equipment such as inverters and uninterruptible power supplies with merely changed loads; however, for motor applications, the fluctuation of modulation coefficient caused by different speeds and loads will influence the ripple pattern, making it challenging to ensure the accuracy of ripple calculation when voltage equations are used to predict ripple. Therefore, it is more feasible to analyze the problem from the perspective of the voltage harmonics of the inverter output. In subsequent research [74], another mode of ripple pattern is demonstrated for the case of line voltage being higher than $U_{dc}/3$. It's also disclosed that the distribution of the current spectrum is related to the modulation factor. When the output voltage is higher, the frequency of harmonics decreases from multiples of $2 * f_{sw}$ to multiples of $f_{sw}$. This emphasizes the merit of analyzing from the perspective of output voltage harmonics because it can accurately predict current ripples regardless of the modulation factor. The research provides a valuable tool for studying PWM induction iron losses.

The total harmonic distortion (THD) of voltage is a critical indicator for evaluating the performance of various modulation methods. The amplitude and distribution of harmonics are the core concerns for EMI testing. Furthermore, in motor control, using voltage harmonics to calculate current harmonics is applicable to different operating conditions. In [75], Narayanan G, Zhao D, et al. proposed two new modulation methods, 1012 and 2721. The voltage harmonics of all possible PWM sequences, including the proposed two, were calculated under the same equivalent switching frequencies for three-phase voltage source inverters (VSI). Hybrid PWM techniques (three-zone PWM, five-zone PWM, and seven-zone PWM) were then proposed. The hybrid PWM switch switching sequences adopt three, five, and seven different PWM sequences in each 60-degree sector, according to the voltage harmonic. It achieves a reduction in total voltage harmonic distortion.

A variable switching frequency hybrid PWM (VSF-HPWM) method was proposed in [76], which uses CSVPWM and discontinuous PWM (DPWM) modulation methods and calculates the switching frequency based on the voltage harmonic amplitude. Simulation results showed that the proposed VSF-HPWM method reduces the switching loss by 53.7% compared to the conventional constant switching frequency method, CSVPWM, in moderate and high modulation index. The experiment carried out on an RL load verified that the proposed method could reduce the number of switching times while maintaining the current ripple's peak value.

Refs. [77] and [78] studied the two- and three-level inverters and proposed a new variable switching frequency hybrid modulation method. As for the two-level inverter, CSVPWM and DPWM012 modulation methods are adapted, and their corner points are calculated in the two-phase stationary coordinate system. The relationship between voltage harmonics and modulation degree/voltage vector angle is derived and stored in the offline lookup table. To prevent the system's response decay due to the possibility of extremely low switching frequency, an adjustment factor is proposed to limit the range of switching frequency variation. Experimental results on a surface-mounted permanent magnet synchronous machine showed that this method could reduce the

switching loss while keeping the peak-to-peak current ripple unchanged without imposing a heavier computation burden on the microcontroller.

The spectrum spread technique disperses the voltage/current EMI harmonic, which is originally concentrated at $N * f_c$, into sidebands. It can reduce the amplitude of EMI emissions and conform to the mandatory electromagnetic compatibility certification requirements. However, this method does not diminish the actual interference with other electronic devices or communication networks, as the total energy emitted by the unintentional network remains the same. Another method to reduce EMI emissions from the source is to reduce common mode voltage modulation, and this technique not only reduces the amplitude of EMI emissions but also reduces the total energy emitted.

Ref. [79] proposes a novel cascaded multi-level circuit topology named interleaved parallel cascaded three-level structure. This structure adopts two interleaved parallel power factor correction units and decouples the interleaved bridges. As a result, the inductor current ripple is significantly reduced by eliminating the circulating current. By operating one of the bridge legs alternately, the common-mode noise source varies with the line frequency, and common-mode noise can be suppressed without relying on the impedance balance.

Ref. [80] develops three new modulation methods for dual three-phase (DT) voltage source inverters to reduce the peak magnitude of the common-mode voltage (CMV). Compared to existing techniques, the proposed methods are simple in software implementation and can also reduce the CMV peak amplitude by 66.8% when applied to the DT asymmetrical induction motor.

Ref. [81] analyzes the generation mechanism of bearing current in the open winding permanent magnet synchronous machine. A new SVPWM strategy for the dual three-phase two-level inverter with a common DC bus is proposed. The proposed method can eliminate uncontrollable zero-sequence current problems in the over-modulation region by optimizing the selection of switch combinations. The proposed method can eliminate CMV variation and suppress full frequency ZSC harmonics in both linear and over-modulation areas. Furthermore, this method can reduce low-frequency as well as high-frequency current harmonics.

Due to the odd number of legs in the three-phase two-level voltage source inverter, only one leg state can be reversed during each switching cycle, resulting in an unavoidable CMV in this topology. A three-phase inverter with an auxiliary four-leg is used in [82] to reduce the CMV. The additional leg flips in coordination with the main leg. The $4^{th}$ leg does not output power to the load, so the switching devices of the leg require a low rated current. Theoretically, simultaneous reversal using this topology can completely eliminate the CMV. However, due to the transistor's dead-time effect and inconsistent dynamic performance, the six times switching frequency pulse CMV would appear, causing the CMV spectrum to shift to higher frequency bands. To solve this problem, Ref. [83] proposes a compensation method for the dead-time effect, effectively reducing the amplitude of six times switching frequency CMV. However, the CMV problem remains unresolved due to the inconsistency of the transistors that occurred during the manufacturing process.

A feasible solution to reduce the CMV amplitude in the three-phase two-level voltage source inverter is to use active vectors instead of zero vectors. In [84], Hava A M and Ün E adjust the vector distribution symmetry of active-zero-state PWM (AZSPWM) about the midpoint of the switching period and propose a modified AZSPWM(MAZSPWM) method. It takes effect at a low modulation index region by avoiding outputting

reversal line voltage. Experiments with a 70-meter cable connecting the motor and inverter confirmed that MAZSPWM could reduce ringing on transmission lines while reducing the CMV.

In [85], a combination of near-state PWM(NSPWM) and MAZSPWM is proposed to reduce the CMV amplitude by 66% in the linear modulation region by avoiding the use of zero vectors. The voltage harmonics are also effectively reduced compared to using either modulation method alone.

While the aforementioned studies have improved EMI performance by spreading the spectrum and suppressing common mode voltage, they have not explored the combined use of these two methods for EMI suppression control. Moreover, although the study mentions the potential current harmonics caused by motor saturation and slotting effects, these factors have not been taken into account in EMI suppression control.

Although the above studies address interference sources from the perspectives of spectrum spreading and common-mode voltage suppression, they do not combine these two methods for EMI suppression control. For example, based on the mathematical models of the motor and controller, programmable frequency-spreading algorithms can be used to plan the switching frequency. Different modulation methods can be applied for various voltage references to reduce low-frequency voltage harmonics, thereby simultaneously reducing common-mode interference while optimizing torque ripple and core losses. While existing research has mentioned that motor saturation and cogging effects induce current harmonics, these factors have not been incorporated into EMI suppression algorithms. To mitigate EMI conduction currents and suppress low-frequency current harmonics in high-overload motors, in addition to spectrum spreading and common-mode voltage reduction, inductance fluctuations caused by cross-saturation and cogging effects should also be taken into account.

## 2.3 HIGH-FREQUENCY SYSTEM MODELING

As power electronics technology continues to evolve, the electromagnetic environment inside and outside motor drive systems has become increasingly complex, leading to more prominent EMC issues. Moreover, the increasing stringency of EMC regulations has significantly raised the cost of traditional EMC trial-and-error methods. Thus, it is important to take EMC requirements as a crucial factor in the early product design stage. The earlier the EMC department intervenes, the more measures can be taken. The conventional approach involves conducting EMC tests once the product design of the electrical and mechanical parts has been completed. In the event of failure, corrective actions are then implemented. However, this method can lead to significant investments in terms of both time and cost.

Forward development refers to considering EMC issues during the early stages of product design. EMC simulation of motor drive systems is one of the critical tools for forward development. EMC simulation is an electromagnetic field simulation, essentially, with the mathematical model as its core component. Lumped parameter models can be utilized when the wavelength of the underlying electromagnetic field is more than ten times the physical dimensions of the studied object. However, as the frequency of the electromagnetic waves increases, lumped parameter models are insufficient, and high-frequency models should be used for more accurate calculations and simulations.

There are several methods for high-frequency modeling of motors, including the finite element method, analytical calculation method, data modeling method, and their combinations. Among them, the finite element

method is based on the four Maxwell's equations (Gauss's law for electric fields, Gauss's law for magnetic fields, Faraday's law of electromagnetic induction, and Ampere's circuital law) and uses the Dirichlet and Neumann boundary conditions to simulate the partitioned regions.

Ref. [86] proposes a novel high-frequency (HF) model for PMSM, which consists of a low-frequency (LF) model and an HF winding branch connected in parallel. The resistance and inductance of each winding turn are calculated using time-harmonic finite element analysis (FEA). In contrast, the self-capacitance and mutual capacitances between turns are evaluated using electrostatic FEA. With the use of Kron reduction technique, the distributed parameter circuit is transformed into a lumped circuit. The proposed model was implemented on a 2-hp PMSM, and simulation results demonstrate its validity for examining machine design, providing a numerical alternative to actual measurements.

To accurately model HF characteristics of electrical machines, both copper and iron losses must be considered within the constraints of limited computational resources. Ref. [87] focused more on copper losses. With 2D finite element method (FEM), the paper investigates the impact of different levels of copper losses due to AC effects, such as skin/proximity effects and circulating currents. The research provides insights into the influence of various model parameters on copper loss considering AC effects and finds that using single-slot models is sufficient for distributed windings. Based on this, a modeling method is proposed to reduce computational time.

2D FEM simulation cannot simulate the end effects, flux leakage and fringing of windings. 3D FEM should be considered in the iron loss simulation. Ref. [88] proposes a new method for calculating eddy current losses in windings of axial flux PMSM. The process takes the eddy current, field fringing and leakage of end turns into consideration using 3D FEM simulation. The proposed method achieves a trade-off between speed and precision. The accuracy of the method is confirmed through tests on a PMSM prototype.

To calculate the parasitic capacitance between the windings and the casing of the motor, it is necessary to model the motor structure in detail. Since HF currents are mainly confined to the surface of conductors, the mesh size used in FEA should be smaller than the skin depth to ensure accuracy. For automotive electric machine systems, the International Special Committee on Radio Interference concerns conducted emissions from 150 kHz to 108 MHz and radiated emissions from 150 kHz to 1 GHz [89]. Corresponding to the skin depth at those frequencies, the mesh sizes with sub-2 μm resolution of conductors made of copper are required.

Besides, in [90], the impact of the mesh size on simulation accuracy is analysed. The results show that at least two mesh layers should be defined between conductors to achieve accurate results. All in all, FEM tools are suitable for conducting detailed HF models of electric machines during the design stage. If the geometry and mesh are defined properly, FEM tools can consider all HF phenomena and provide extremely accurate results.

Compared with FEM simulations, analytical methods often involve making simplifications under a set of assumptions to calculate the resistance, inductance, and capacitance of the motor. Although these calculations are generally less precise than FEM simulations due to the simplifications, they require significantly fewer computational resources.

Ref. [91] presents a three-phase induction motor model that covers a wide range of frequencies, namely from 10 Hz to 10 MHz. The model is unique in combining common mode (CM), differential mode (DM), and

bearing circuit into a three-phase equivalent circuit model. The proposed model is an extension of the LF IEEE Standard 112 circuit model. The experimental results presented in this paper demonstrate the model's suitability for long cable applications on adjustable speed drives.

Ref. [92] addresses the bearing current problems arising from using HF power electronic devices in wind power generation systems. A common mode model is proposed, which takes into account the inner structure of the induction motor. The emphasis was placed on the analytical calculation formula for distributed capacitance in the model.

For analytical methods, computation time can often be reduced by making assumptions and simplifications according to the structure of the motor. For example, the skin effect can be easily calculated analytically by reducing the effective cross-section area of the conductors. For capacitance, geometric simplifications are often made to simplify calculations, e.g., winding-to-rotor capacitance simplified to plate capacitors, and stator-to-rotor capacitance to cylindrical ones. However, the proximity effect is difficult to simplify due to the non-uniform distribution of the magnetic field in the slot. Furthermore, although various methods can be used for simplifying turn-to-turn capacitance calculations, the specific disposition of the winding must be taken into account, or large errors may occur.

Establishing the HF model by using measurement-based methods measures both DM and CM impedance and gets the circuit parameters from the measured results. Measurement-based methods can achieve accurate results by adjusting model parameters across the entire frequency range. However, it's important to note that this approach is not suitable for the design stage of the motor, as it requires the prototype to be built to perform experimental impedance measurements. Rather than for predicting the behaviour of the motor during the design process, this approach is more appropriate for predicting the performance of the overall electric drive system, including the inverter, EMI filter, and control method. There are two technical strategies to build the measurement-based model. The first involves deciphering the physical meaning of each parameter and identifying it with the impedance curve. The second approach uses parameter fitting techniques without considering the physical meaning, which can result in negative parameters. The measurement-based models obtained by both strategies can provide excellent accuracy throughout a wide frequency range.

Ref. [93] proposes an HF model for a 3 kW series winding PMSM with a star connection. Separate analysis for each phase of the three-phase windings is conducted. The model for each phase is then divided into HF, LF, CM, and DM parts. Then, the above individual models are combined to form the complete model. This model considers the inter-turn effects of the windings and the leakage inductance effect of the first few turns of the winding. All the parameters have physical meaning. The model accurately depicts both CM and DM impedances of the motor, particularly in the middle-frequency range, namely 10kHz to 1MHz.

Ref. [94] presents a novel modelling approach for analysing conducted EMI in PMSM drive systems. The approach employs three-phase circuits to represent the DM and CM behaviours of PMSM and AC cables. The parameters of the model can be determined using CM and DM measurements by Inductance, Capacitance, and Resistance (LCR) meter regardless of the physical motor’s winding configuration. Experimental results are presented to validate the accuracy of the proposed models in a frequency range of up to 10 MHz.

Ref. [95] proposes an improved HF IPM model for drive systems. The HF motor model is based on a conventional IPM motor model and is augmented to represent the HF transients. The DM and CM impedance data are measured by an impendence analyser. With the data, the model parameters can be identified using a population-based optimization method, such as a genetic or particle swarm algorithm. The complete motor drive simulation system is established using LTspice. This model can predict transient overvoltage and conduct EMI and system losses to facilitate performance verification and system design.

Ref. [96] presents an HF model of the motor in EVs without considering the physical meaning of parameters. The CM impedance data of the motor are measured. Then, a vector fitting technique is adopted to identify the model parameters. Although the resistance and capacitance of the model are negative, the HF motor modelling method is pragmatic and effective. The simulation and experiment results show that the proposed model effectively describes the CM EMI levels of the motor drive system from 150 kHz to 30 MHz. The obtained model is used to predict and compare CM conducted emission and can be used to design a CM filter for reducing conducted EMI.

Ref. [97] introduces another HF parametric model for electrical machines. The model is represented by lumped equivalent circuits and the corresponding complex impedance equations. The differential evolution algorithm is employed to parameterize the models according to the measured CM and DM impedance data. The complex and negative real values are excluded to ensure physical meaningfulness. The impedance predicted by the model is compared to the measured impedance of a series of electrical machines. The results show that the model can predict EMI emission and facilitate the development of EMI filters and inverters.

The finite element method, analytical calculation method, measurement-based modeling method, and their combinations can be used for high-frequency modeling of motors. The measurement-based modeling method is more appropriate for predicting the performance of the overall electric drive system, and it is suitable to be adopted in EMC forward development.

There are two technical strategies to build the measurement-based model. The first involves deciphering the physical meaning of each parameter. The second approach uses parameter fitting techniques without considering the physical meaning. The measurement-based models obtained by both strategies can provide excellent accuracy throughout a wide frequency range.

The measurement-based approach, which takes into account the physical meaning, attempts to explain the formation of measured data but currently cannot accurately reveal the mechanism behind the formation of high-frequency resonance points. Moreover, the data model considering the physical significance can predict the impedance characteristics in untested frequency ranges and provide more precise interpolation results. On the other hand, for data models that do not consider the physical meaning, model accuracy can be improved by expanding the measuring frequency range and increasing the density of measuring points.

Considering finite element methods, analytical calculation methods, and external characteristic-based modeling approaches, each has its unique strengths and limitations. External characteristic-based high-frequency modeling is well-suited for predicting the overall performance of electric drive systems and for forward EMC design of controllers and algorithms, making it an appropriate choice for this study. Although existing models can simulate the high-frequency impedance through iterative adjustments, the process is complex, and the

reproducibility of the modeling results is challenging. Additionally, the frequency-dependent variation of component parameters in the model poses difficulties for time-domain simulations. Therefore, developing a high-frequency time-domain model is an urgent problem that needs to be addressed.

With the increasing complexity of the electromagnetic environment in motor drive systems and the tightening of EMC regulations, the traditional trial-and-error approach to EMC design is no longer sufficient to meet the demands of efficient and cost-effective development. High-frequency modeling, as a key technique in forward EMC design, plays a crucial role in predicting and optimizing the electromagnetic performance of motor systems at the early design stage. Current mainstream modeling approaches include the finite element method (FEM), analytical methods, measurement-based modeling, and their combinations—each with its own strengths and limitations. FEM offers high accuracy but requires intensive computation; analytical methods are efficient but limited in applicability; measurement-based approaches are more suitable for system-level EMI prediction. Overall, modeling based on external characteristics aligns better with the requirements of controller and system-level EMC design and thus represents a key focus of this study.

## 2.4 SUMMARY

In summary, the current research on motor control and modulation faces significant challenges in several areas, including error modeling due to inverter sampling output delays, precise decoupling of the motor under cross-saturation conditions, and electromagnetic interference issues. These challenges are particularly pronounced under high-speed, high-overload operating conditions.

(1) To enhance the performance of current controllers, it is crucial to develop high-performance control strategies that accurately model the motor and controller while considering cross-saturation and discrete delays. This is key to improving the system's bandwidth and stability under high-speed, high-overload conditions.

(2) Regarding the high-frequency modeling of motors, existing methods each have their strengths and weaknesses. Among them, those based on external characteristics have advantages in EMC-forward design of controllers and algorithms, making them suitable for application in this study. However, current models use trial-and-error methods to characterize the second resonance point of high-frequency impedance, a process that is complex and difficult to ensure repeatability. Therefore, there is an urgent need to develop a time-domain high-frequency model that can precisely characterize the second resonance point to address this critical issue.

(3) As for EMI suppression modulation algorithms, current research primarily focuses on spectrum spreading and common-mode voltage suppression to mitigate interference sources, but has yet to combine these two approaches for collaborative suppression control. Additionally, while studies have pointed out that motor saturation and cogging effects induce current harmonics, these factors have not been adequately addressed in existing EMI suppression algorithms. Therefore, incorporating the impact of saturation and cogging effects on inductance fluctuations is essential for optimizing EMI suppression algorithms.

# Chapter 3: Modeling of Permanent Magnet Synchronous Motor Driving System

The downsizing of motors and controllers has resulted in the deterioration of motor currents and electromagnetic environments. Optimization can be carried out through hardware and software to achieve low harmonics, high bandwidth, and reduced electromagnetic interference. Accurate system modeling serves as the fundamental foundation for effective optimization.

When the wavelength of the electromagnetic field of interest is much larger than the physical size of the drive system, a lumped parameter model of the system can be employed. In this case, it is assumed that no electric and magnetic fields are present in the external environment of the controller, connecting wires, and the motor. The inverter can be considered as an ideal pulse voltage source, and the wires can be modeled using ideal resistance elements, while a lumped parameter model can represent the motor. However, as the frequency of the electromagnetic waves of interest increases, specifically when the wavelength is smaller than ten times the system size, the lumped parameter model is no longer applicable [98]. To assist in the design of the current loop controller and validate the effectiveness of spread spectrum PWM control, this chapter will focus on modeling both lumped parameter and distributed parameter systems separately.

## 3.1 LUMPED PARAMETER MODEL OF PMSM

Lumped parameter modelling adopts a group of differential equations, including voltage equations, flux linkage equations, torque equations, and motion equations, etc. These equations are often simplified by coordinate transformations and combined with power electronic converters to provide a basis for designing motor controllers.

Depending on the assumptions made for the modelling, the lumped parameter model can be categorized as small-signal linear models, nonlinear models considering saturation, nonlinear models considering cross-saturation, models considering spatial harmonics caused by slotting, and nonlinear models considering temperature[99]. In contrast to industrial motors, high power density motors exhibit varying load and operating conditions, along with non-uniform temperature distribution. In this research, the nonlinear effects caused by temperature changes are neglected. The motor under research is assumed to operate at 25°C. The following section will introduce three types of lumped parameter motor models.

### 3.1.1 Small-Signal Linear Model of PMSM

The small-signal model is a method that linearizes a nonlinear system at a specific operating point to assist system analysis and design in its vicinity. In the case of a PMSM, the small-signal model typically adopts the parameters at the rated operating point as system parameters.

To simplify the model, the small-signal linear model of a PMSM is based on the following assumptions:

1. Neglecting the saturation effect of the iron core.

2. Ignoring eddy current losses and hysteresis losses.

3. Assuming no damping winding on the rotor and no damping effect from the permanent magnet.

4. Assuming the main magnetic field generated by the permanent magnet and the armature reaction magnetic field excited by the winding current have a sinusoidal distribution in the air gap.

5. Neglecting changes in electromagnetic properties of materials due to temperature.

Figure 3.1 illustrates commonly used coordinate systems. In the analysis of a PMSM, the a-b-c coordinate system is often employed as a three-phase stationary coordinate system, where the abc axes align with the actual three-phase stator winding central axes, with a phase difference of 120 degrees between them. The α-β coordinate system is a two-phase stationary coordinate system, with the α-axis coinciding with the a-phase axis and the β-axis leading the α-axis by 90 electrical degrees. By utilizing the property that the sum of three-phase currents in a three-phase motor is zero, the two-phase stationary coordinate system reduces the number of variables, simplifying the model. The d-q coordinate system is a two-phase synchronous rotating coordinate system, where the d-axis is aligned with the direction of the N-pole of the rotor's permanent magnet, and the q-axis is positioned 90 electrical degrees ahead of the d-axis. By introducing the two-phase synchronous rotating coordinate system, the rotating magnetomotive force can be replaced with a stationary one. This replacement eliminates the time-varying coefficients in the voltage equations, simplifying analysis and calculations [100].

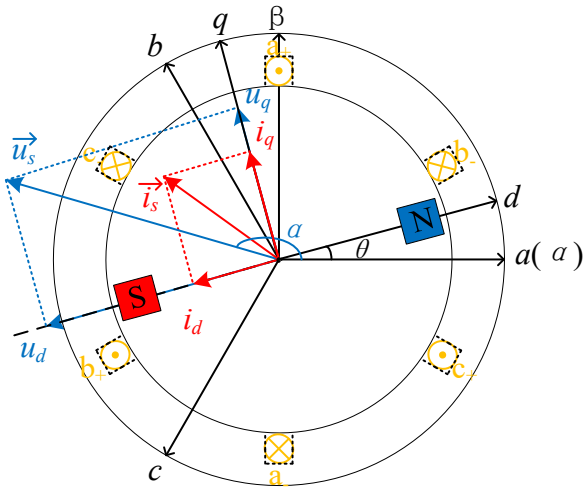


Figure 3.1 The physical model and reference coordinate system for a dual-pole PMSM.

The voltage equations of PMSM in the *d-q* synchronous rotating frame are first-order differential equations with constant coefficients. The voltage can be described as follows:

$$\begin{bmatrix} u_d \\ u_q \end{bmatrix} = R \begin{bmatrix} i_d \\ i_q \end{bmatrix} + \frac{d}{dt} \begin{bmatrix} \psi_d \\ \psi_q \end{bmatrix} + \omega_e \begin{bmatrix} -\psi_q \\ \psi_d + \lambda_{pm} \end{bmatrix} \tag{3.1}$$

where $u_d$ and $u_q$ are the stator voltages of direct and quadrature axes, $i_d$ and $i_q$ are the stator currents of direct and quadrature axis, $R$ is stator winding resistance, and $\omega_e$ is the electrical rotational speed. $\psi_d$ and $\psi_q$ are the flux linkages of direct and quadrature axes due to the stator current excitation. For PMSM, $\lambda_{pm}$ represents

permanent magnet flux linkage, which is excited by the permanent magnet.

The voltage equations of PMSM in the *d-q* synchronous rotating frame are shown in (3.2), where $L_d$ and $L_q$ are the inductance of direct and quadrature axis.

$$\begin{bmatrix}\psi_d\\ \psi_q\end{bmatrix}=\begin{bmatrix}L_d & 0\\ 0 & L_{\mathrm{q}}\end{bmatrix}\begin{bmatrix}i_d\\ i_q\end{bmatrix} \tag{3.2}$$

The electromagnetic torque $T_e$ can be calculated using (3.3), where $p$ is the pole paires of PMSM.

$$T_e=\frac{3}{2}p\left[\left(\psi_d+\lambda_{pm}\right)i_q-\psi_q i_d\right]=\frac{3}{2}p\left[\lambda_{pm}i_q+\left(L_d-L_q\right)i_d i_q\right] \tag{3.3}$$

The motion equation is shown in (3.4).

$$T_e-T_l=J\frac{d\omega_m}{dt}+B_\omega\omega_m \tag{3.4}$$

where $T_l$ is the load torque, $J$ is the moment of inertia of the motor shaft, $B_\Omega$ is the damping coefficient, which incorporates factors such as aerodynamic drag and bearing friction. Typically, $B_\omega$ is a nonlinear function of the rotational speed. $\omega_m$ is the mechanical angular velocity of the rotor, and its relationship with the electrical angular velocity $\omega_e$ is given by (3.5)

$$\omega_m=\frac{\omega_e}{p} \tag{3.5}$$

### 3.1.2 Nonlinear Model of PMSM Considering Cross-Saturation

The small-signal linear model of PMSM has simple structures, making it well-suited for controller design using classical control theory when the motor works near the rated current. However, the magnetoconductivity $\mu$ of the ferromagnetic material is influenced by the magnetic field intensity *H* and magnetic induction intensity *B*. As the magnetic field intensity increases rapidly, $\frac{dB}{dH}$ of the iron core decreases by several hundred times compared to the state without excitation. Once the iron core reaches saturation, $\frac{dB}{dH}$ ultimately approaches the magnetoconductivity of vacuum $\left(\frac{dB}{dH}\approx\mu_0=4\pi\times10^{-7}\,H/m\right)$. The inductance would experience a significant reduction to one-tenth of its initial magnitude, according to the finite element simulation result in this study. For highly overloaded motors, neglecting the nonlinear effects of inductance becomes inadequate for achieving good current control and voltage output[101].

As the *dq*-axis magnetic circuits of the PMSM have a common portion, the magnetic saturation induced by $i_d$ will also influence the *q*-axis flux. Likewise, $i_q$ will affect the *d*-axis flux. Accounting for the presence of cross-saturation, the flux linkage components on the *d* and *q*-axes of the PMSM are respectively denoted as $\Psi_d\left(i_d,i_q\right)$ and $\Psi_q\left(i_d,i_q\right)$, in which the flux linkages induced by current excitation are denoted as $\psi_d\left(i_d,i_q\right)$ and $\psi_q\left(i_d,i_q\right)$, while the flux linkage from the permanent magnet is denoted as $\lambda_{pm}\left(i_d,i_q\right)$. The relationship of the above flux linkage can be expressed as:

$$\begin{bmatrix}\Psi_d\left(i_d,i_q\right)\\ \Psi_q\left(i_d,i_q\right)\end{bmatrix}=\begin{bmatrix}\psi_d\left(i_d,i_q\right)\\ \psi_q\left(i_d,i_q\right)\end{bmatrix}+\begin{bmatrix}\lambda_{pm}\left(i_d,i_q\right)\\ 0\end{bmatrix} \tag{3.6}$$

By substituting $\psi_d(i_d, i_q)$ and $\psi_q(i_d, i_q)$ for $\psi_d$ and $\psi_q$ in (3.6), the voltage equation considering cross-saturation can be obtained.

$$\begin{bmatrix} u_d \\ u_q \end{bmatrix} = R\begin{bmatrix} i_d \\ i_q \end{bmatrix} + \frac{d}{dt}\begin{bmatrix} \Psi_d(i_d, i_q) \\ \Psi_q(i_d, i_q) \end{bmatrix} + \omega_e \begin{bmatrix} -\psi_q(i_d, i_q) \\ \psi_d(i_d, i_q) + \lambda_{pm}(i_d, i_q) \end{bmatrix} \tag{3.7}$$

Considering cross-saturation, the static inductance on the $dq$-axis can be denoted as $L_d(i_d, i_q)$ and $L_d(i_d, i_q)$, respectively, as shown in (3.8). The flux equation is given in (3.9).

$$L_d(i_d, i_q) = \frac{\psi_d(i_d, i_q)}{i_d}, L_q(i_d, i_q) = \frac{\psi_q(i_d, i_q)}{i_q} \tag{3.8}$$

$$\begin{bmatrix} \psi_d(i_d, i_q) \\ \psi_q(i_d, i_q) \end{bmatrix} = \begin{bmatrix} L_d(i_d, i_q) & 0 \\ 0 & L_q(i_d, i_q) \end{bmatrix}\begin{bmatrix} i_d \\ i_q \end{bmatrix} \tag{3.9}$$

Compared with $\psi_d$ and $\psi_q$, the variation of $\lambda_{pm}$ with respect to $(i_d, i_q)$ is negligible. To simplify the analysis, it is assumed that $\lambda_{pm}$ remains constant. The voltage equation is expressed as in (3.10):

$$\begin{bmatrix} u_d \\ u_q \end{bmatrix} = R\begin{bmatrix} i_d \\ i_q \end{bmatrix} + \begin{bmatrix} \frac{d\psi_d(i_d, i_q)}{di_d}\frac{di_d}{dt} + \frac{d\psi_d(i_d, i_q)}{di_\mathrm{q}}\frac{di_\mathrm{q}}{dt} \\ \frac{d\psi_d(i_d, i_q)}{di_d}\frac{di_d}{dt} + \frac{d\psi_d(i_d, i_q)}{di_\mathrm{q}}\frac{di_\mathrm{q}}{dt} \end{bmatrix} + \omega_e \begin{bmatrix} -L_q(i_d, i_q)i_q \\ L_d(i_d, i_q)i_d + \lambda_{pm}(i_d, i_q) \end{bmatrix} \tag{3.10}$$

Defining the dynamic inductances $L_{dd}(i_d, i_q)$, $L_{dq}(i_d, i_q)$, $L_{qd}(i_d, i_q)$, $L_{qq}(i_d, i_q)$ as shown in (3.11) and (3.12)

$$L_{dd}(i_d, i_q) = \frac{\partial\psi_d(i_d, i_q)}{\partial i_d}, L_{dq}(i_d, i_q) = \frac{\partial\psi_d(i_d, i_q)}{\partial i_q} \tag{3.11}$$

$$L_{qd}(i_d, i_q) = \frac{\partial\psi_q(i_d, i_q)}{\partial i_d}, L_{qq}(i_d, i_q) = \frac{\partial\psi_q(i_d, i_q)}{\partial i_q} \tag{3.12}$$

Then we have,

$$\begin{bmatrix} u_d \\ u_q \end{bmatrix} = R\begin{bmatrix} i_d \\ i_q \end{bmatrix} + \begin{bmatrix} L_{dd}(i_d, i_q) & L_{dq}(i_d, i_q) \\ L_{qd}(i_d, i_q) & L_{qq}(i_d, i_q) \end{bmatrix}\frac{d}{dt}\begin{bmatrix} i_d \\ i_q \end{bmatrix} + \omega_e \begin{bmatrix} -L_q(i_d, i_q)i_q \\ L_d(i_d, i_q)i_d + \lambda_{pm}(i_d, i_q) \end{bmatrix} \tag{3.13}$$

The relationships between the $dq$-axis flux $\psi_d(i_d, i_q)$, $\psi_q(i_d, i_q)$ and the currents $i_d, i_q$ are influenced by the magnetic circuit structure and the magnetoconductivity of the medium. So, obtaining an analytical solution is challenging, and numerical computation methods are typically employed. By employing finite element simulations to scan the electromagnetic transient field, tables containing the values of $\psi_d(i_d, i_q)$, $\psi_q(i_d, i_q)$ for various $i_d, i_q$ combinations can be obtained. Equations (3.8), (3.11), and (3.12) can be utilized to calculate the dynamic and static inductance data based on the flux, and the results can be stored in the form of a three-dimensional table for the controller to access. The relationship between the current and nonlinear parameters is depicted in the following figure.

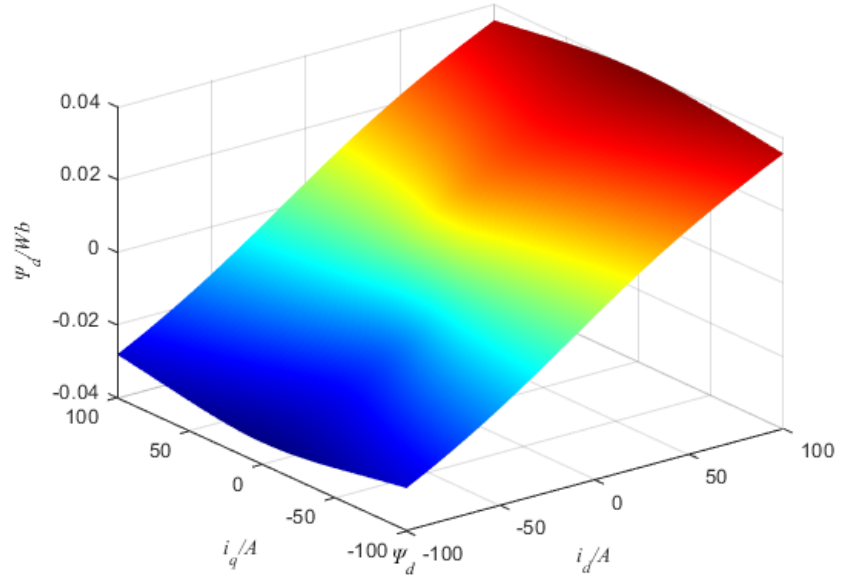


(a) Diagram of flux linkage $\psi_d$ as a function of current $(i_d, i_q)$.

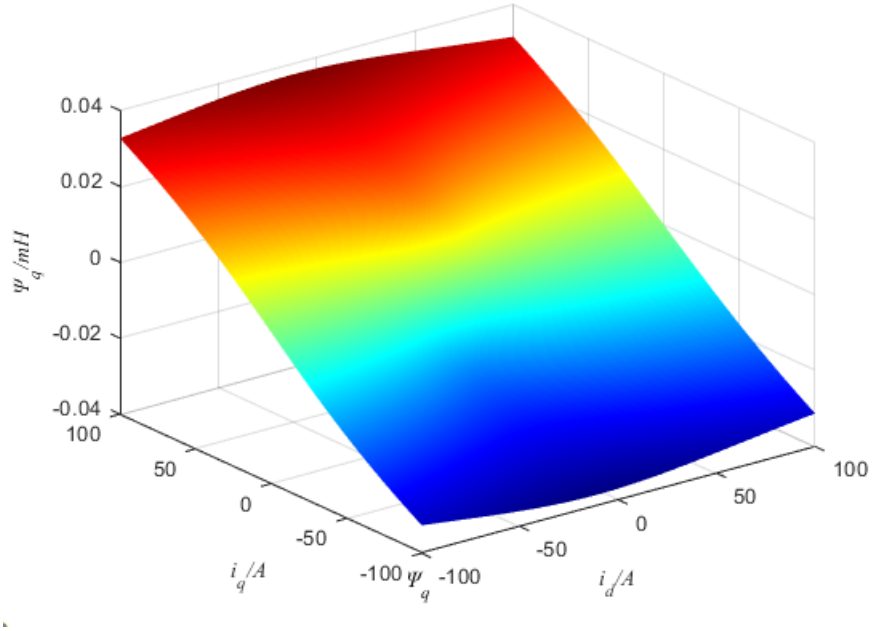


(b) Diagram of flux linkage $\psi_q$ as a function of current $(i_d, i_q)$.

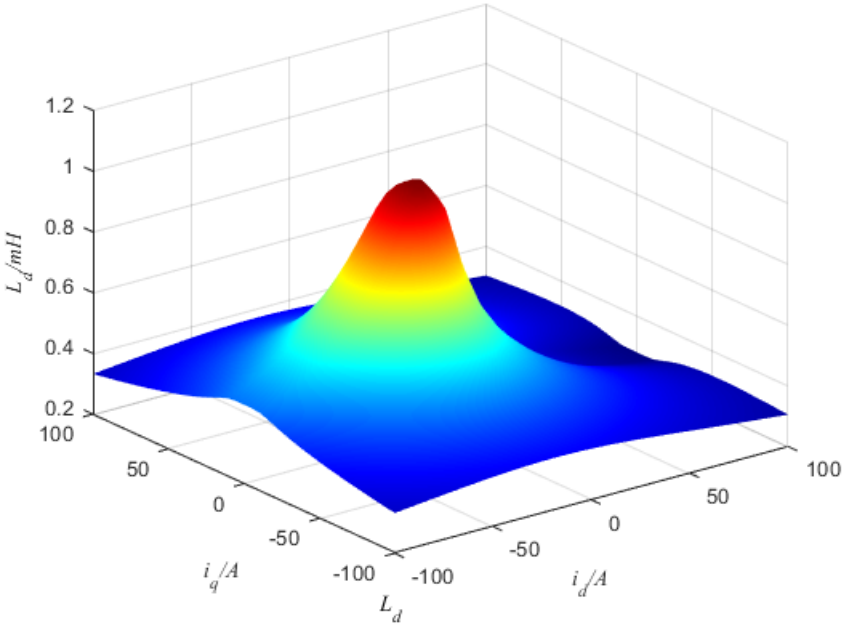


(c) Diagram of static inductance $L_d$ as a function of current $(i_d, i_q)$.

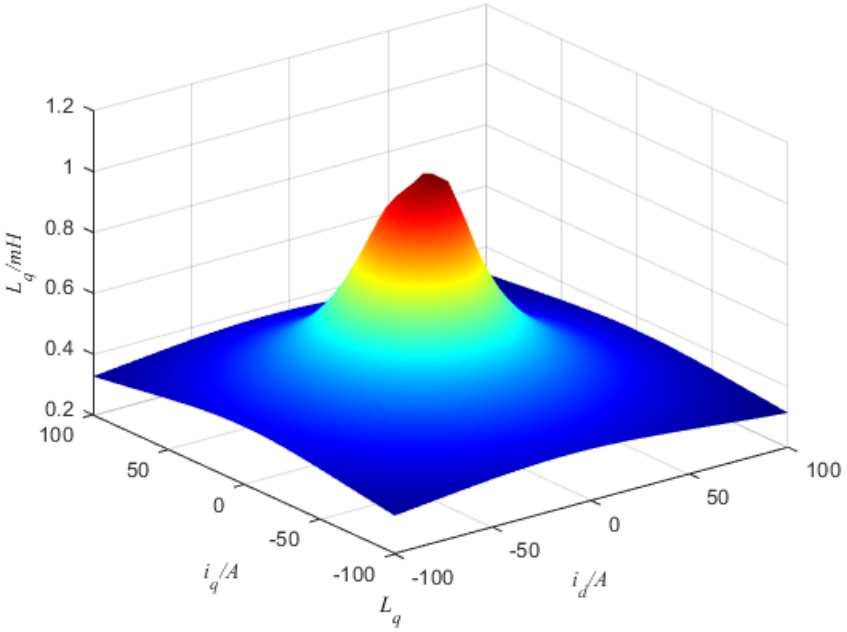


(d) Diagram of static inductance $L_q$ as a function of current $(i_d, i_q)$.

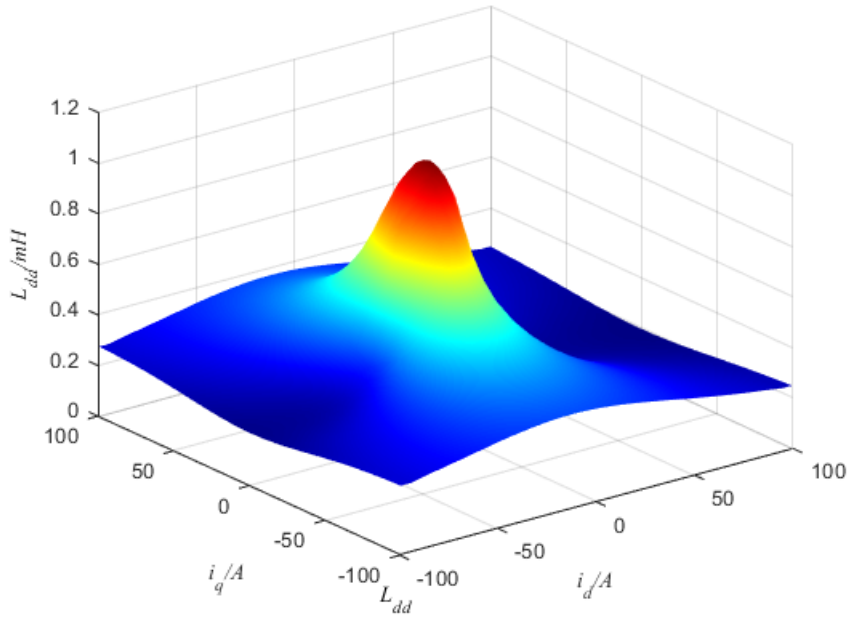


(e) Diagram of dynamic inductance $L_{dd}$ as a function of current $(i_d, i_q)$.

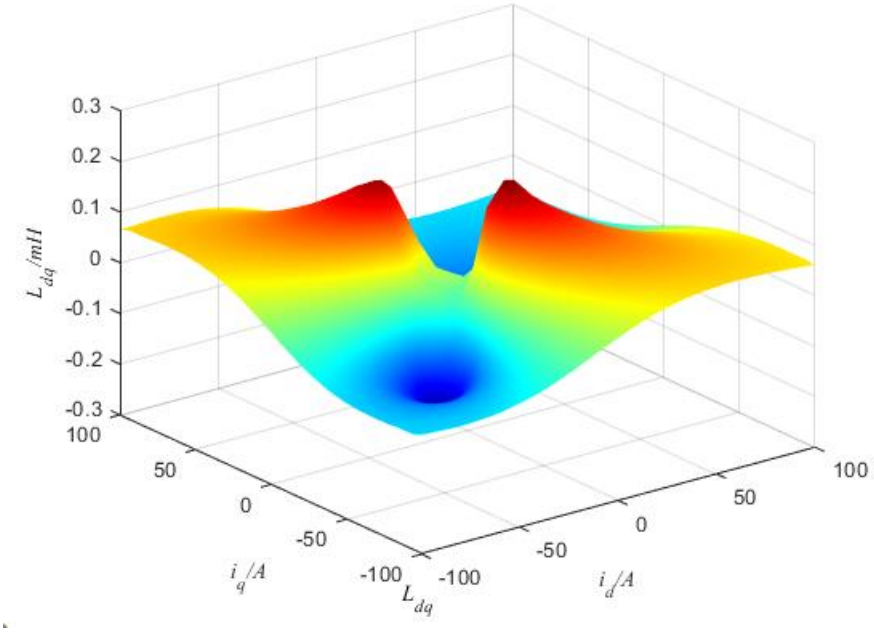


(f) Diagram of dynamic inductance $L_{dq}$ as a function of current $(i_d, i_q)$.

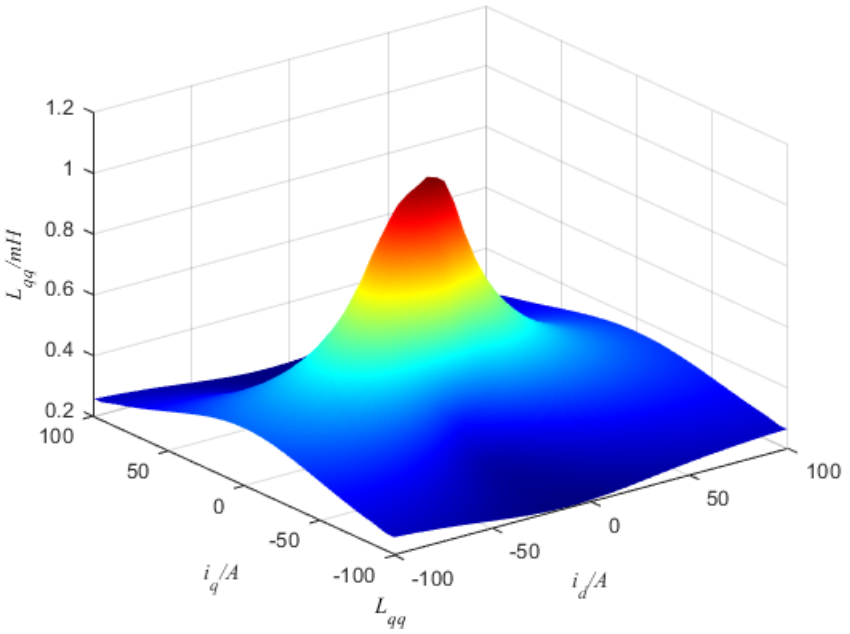


(g) Diagram of dynamic inductance $L_{qq}$ as a function of current $(i_d, i_q)$

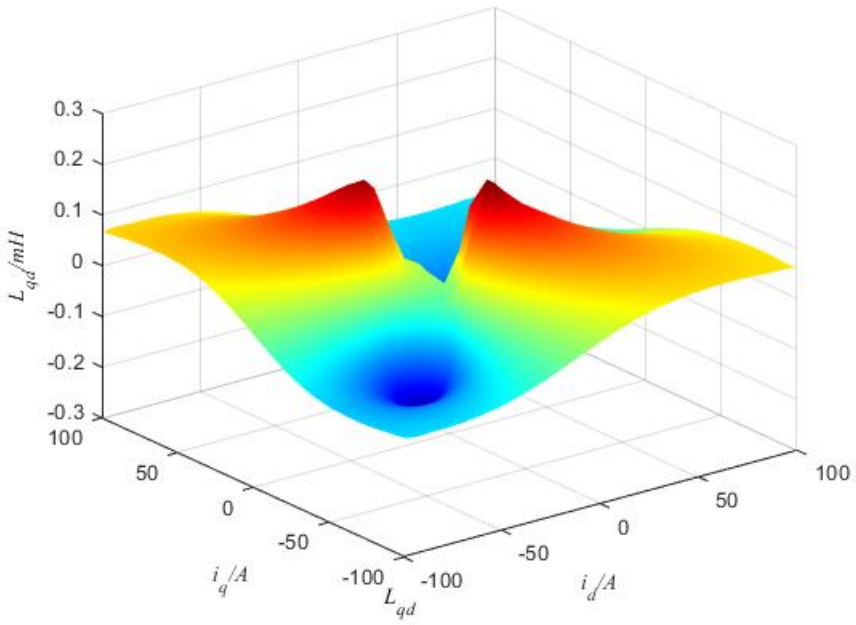


(h) Diagram of dynamic inductance $L_{qd}$ as a function of current $(i_d, i_q)$.

Figure 3.2 Flux linkage, static inductance, and dynamic inductance data for the $dq$-axis ($\psi_d(i_d, i_q)$, $\psi_q(i_d, i_q)$, $L_d(i_d, i_q)$, $L_q(i_d, i_q)$, $L_{dd}(i_d, i_q)$, $L_{dq}(i_d, i_q)$, $L_{qq}(i_d, i_q)$, $L_{qd}(i_d, i_q)$).

Based on the findings from finite element simulations, it can be observed that the influence of the current on the permanent magnet flux linkage $\lambda_{pm}(i_d, i_q)$ is small. Hence, it is neglected in this study.

### 3.1.3 Nonlinear Model of PMSM Considering Slotting Effect

In order to accommodate the winding within the stator iron core, slots are required on the stator. The high-frequency spatial harmonics generated by slotting effect cause the distribution of the armature reaction flux linkage induced by the excitation current in the air gap to deviate from a sinusoidal shape. Since the three-phase armature reaction flux linkages $\psi_a(i_a, i_b, i_c)$, $\psi_b(i_a, i_b, i_c)$, $\psi_c(i_a, i_b, i_c)$ in the air gap do not exhibit a standard sinusoidal waveform, the resulting *dq*-axis flux linkages $\psi_d(i_d, i_q)$ and $\psi_q(i_d, i_q)$ after applying Clark and Park transformations exhibit fluctuations. Specifically, when the *d*-axis is aligned with a slot, the magnetic reluctance of the *d*-axis path increases, leading to a reduction in $\psi_d(i_d, i_q)$. On the other hand, when the *d*-axis aligns with a tooth, the magnetic reluctance of the *d*-axis path decreases, resulting in an increase in $\psi_d(i_d, i_q)$. As the rotor rotates, the *d*-axis flux undergoes periodic variations, with six fluctuations occurring within each electrical cycle. The same situation applies to the *q*-axis.

Therefore, considering the slotting effect and iron core saturation, both the excitation current and rotor position have an impact on the flux linkage. As shown in Figure 3.1, denoting the electrical angular displacement where the *d*-axis leads the *a*-axis as $\theta$, the *d*-axis flux linkage is represented as $\psi_d(i_d, i_q, \theta)$, the q-axis flux linkage as $\psi_q(i_d, i_q, \theta)$, and the permanent magnet flux linkage as $\lambda_{pm}(i_d, i_q, \theta)$. By replacing $\psi_d(i_d, i_q)$ and $\psi_q(i_d, i_q)$ with $\psi_d(i_d, i_q, \theta)$ and $\psi_q(i_d, i_q, \theta)$ in (3.7), the voltage equation (3.14) considering cross-saturation and slotting effect is derived.

$$\begin{bmatrix} u_d \\ u_q \end{bmatrix} = R \begin{bmatrix} i_d \\ i_q \end{bmatrix} + \frac{d}{dt} \begin{bmatrix} \Psi_d(i_d, i_q, \theta) \\ \Psi_q(i_d, i_q, \theta) \end{bmatrix} + \omega_e \begin{bmatrix} -\psi_q(i_d, i_q, \theta) \\ \psi_d(i_d, i_q, \theta) + \lambda_{pm}(i_d, i_q, \theta) \end{bmatrix} \tag{3.14}$$

The static inductances on the *dq*-axis, considering the effect of slots, are denoted as $L_d(i_d, i_q, \theta)$ and $L_q(i_d, i_q, \theta)$ in (3.15). The dynamic inductances $L_{dd}(i_d, i_q, \theta)$, $L_{dq}(i_d, i_q, \theta)$, $L_{qd}(i_d, i_q, \theta)$, $L_{qq}(i_d, i_q, \theta)$ are defined according to (3.16) and (3.17).

$$L_d(i_d, i_q, \theta) = \frac{\psi_d(i_d, i_q, \theta)}{i_d}, L_q(i_d, i_q, \theta) = \frac{\psi_q(i_d, i_q, \theta)}{i_q} \tag{3.15}$$

$$L_{dd}(i_d, i_q, \theta) = \frac{\partial \psi_d(i_d, i_q, \theta)}{\partial i_d}, L_{dq}(i_d, i_q, \theta) = \frac{\partial \psi_d(i_d, i_q, \theta)}{\partial i_q} \tag{3.16}$$

$$L_{qd}(i_d, i_q, \theta) = \frac{\partial \psi_q(i_d, i_q, \theta)}{\partial i_d}, L_{qq}(i_d, i_q, \theta) = \frac{\partial \psi_q(i_d, i_q, \theta)}{\partial i_q} \tag{3.17}$$

The voltage and flux linkage equation is shown in (3.17) and (3.18).

$$\begin{bmatrix} \psi_d(i_d, i_q, \theta) \\ \psi_q(i_d, i_q, \theta) \end{bmatrix} = \begin{bmatrix} L_d(i_d, i_q, \theta) & 0 \\ 0 & L_q(i_d, i_q, \theta) \end{bmatrix} \begin{bmatrix} i_d \\ i_q \end{bmatrix} \tag{3.18}$$

$$\begin{bmatrix} u_d \\ u_q \end{bmatrix} = R \begin{bmatrix} i_d \\ i_q \end{bmatrix} + \begin{bmatrix} L_{dd}(i_d, i_q, \theta) & L_{dq}(i_d, i_q, \theta) \\ L_{qd}(i_d, i_q, \theta) & L_{qq}(i_d, i_q, \theta) \end{bmatrix} \frac{d}{dt} \begin{bmatrix} i_d \\ i_q \end{bmatrix} + \omega_e \begin{bmatrix} -L_q(i_d, i_q, \theta) i_q \\ L_d(i_d, i_q, \theta) i_d + \lambda_{pm}(i_d, i_q, \theta) \end{bmatrix} \tag{3.19}$$

Considering the torque fluctuation caused by the impact of spatial harmonics, the electromagnetic torque $T_e(i_d, i_q, \theta)$ can be derived from the rate of change of the co-energy [102] $W'(i_d, i_q, \theta)$ with respect to the rotor

position $\theta_m$, as expressed in (3.20). Without current excitation, $T_e(0,0,\theta)$ represents the torque generated by slotting. Under zero current excitation conditions, $T_e(0,0,\theta)$ represents the intrinsic torque component caused by the slot structure, which is one of the main sources of torque ripple.

$$T_e(i_d,i_q,\theta)=\frac{3}{2}p\left[\lambda_{pm}(i_d,i_q,\theta)i_q+\left(L_d(i_d,i_q,\theta)-L_q(i_d,i_q,\theta)\right)i_d i_q\right]$$
$$+\frac{3}{2}p\left[\frac{\partial\lambda_{pm}(i_d,i_q,\theta)i_d}{\partial\theta}+\frac{\partial L_q(i_d,i_q,\theta)i_q^2}{\partial\theta}+\frac{\partial L_d(i_d,i_q,\theta)i_d^2}{\partial\theta}\right]$$
$$-p\frac{\partial W(i_d,i_q,\theta)}{\partial\theta} \tag{3.20}$$

The flux linkage $\psi_d(i_d,i_q,\theta)$ 、 $\psi_q(i_d,i_q,\theta)$, is determined by the magnetic path and the medium's magnetoconductivity. The direction of the magnetic path is influenced by the combination of the magnetic circuit structure and the angle of the motor. Additionally, it is difficult to accurately model the magnetization curve of the stator core using analytical methods. Notably, a frameless permanent magnet synchronous motor with a 20-pole, 24-slot configuration is employed as the simulation model. However, the proposed method is equally applicable to other axial or radial flux PMSMs, reluctance motors, and dual-rotor or dual-stator machines with different pole-slot combinations. Consequently, analytical calculations for the flux linkages are challenging, and numerical calculation methods are commonly employed. By performing transient magnetic field scans using finite element simulation, the relationship between $\psi_d(i_d,i_q,\theta)$, $\psi_q(i_d,i_q,\theta)$, and $i_d,i_q,\theta$ can be obtained. The inductance data can be obtained using (3.15), (3.16), and (3.17), and the results can be stored in the form of a four-dimensional table representing the inductance values with respect to $i_d,i_q,\theta$, for the convenience of controller's access. The sliced contour plots of the four-dimensional table are shown below in Figure 3.3, consisting of 9 pages of contour plots from left to right, representing the flux linkage and inductance values at 0, 1.625, 3.25, 7.5,15 and 30 degrees.

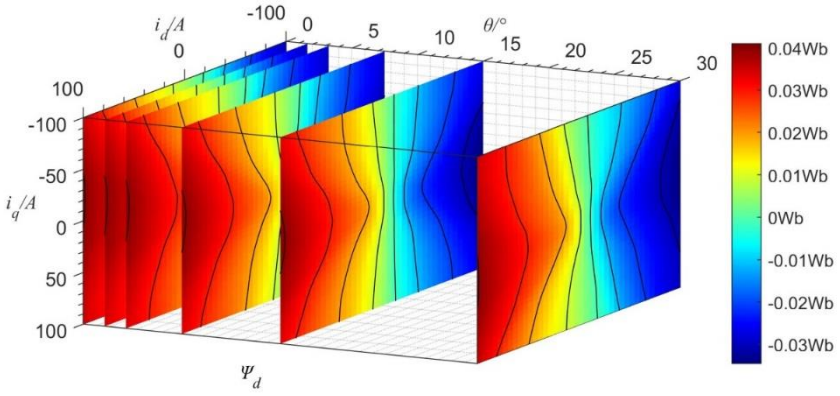


(a) Diagram of flux linkage $\psi_d$ as a function of current and position $(i_d,i_q,\theta)$.

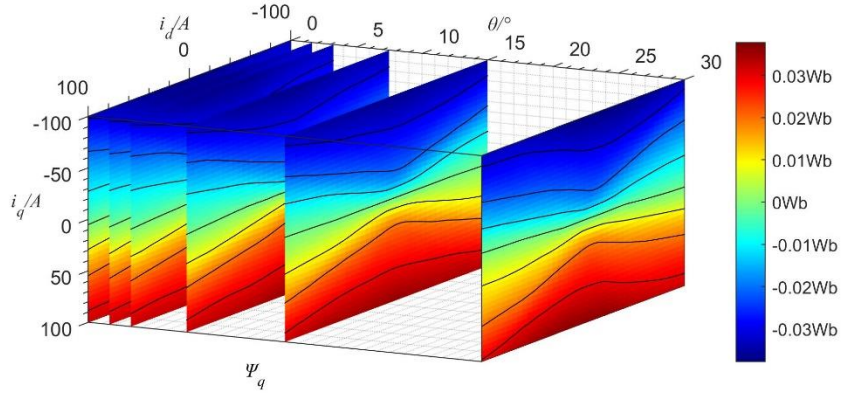


(b) Diagram of flux linkage $\psi_q$ as a function of current and position $(i_d, i_q, \theta)$.

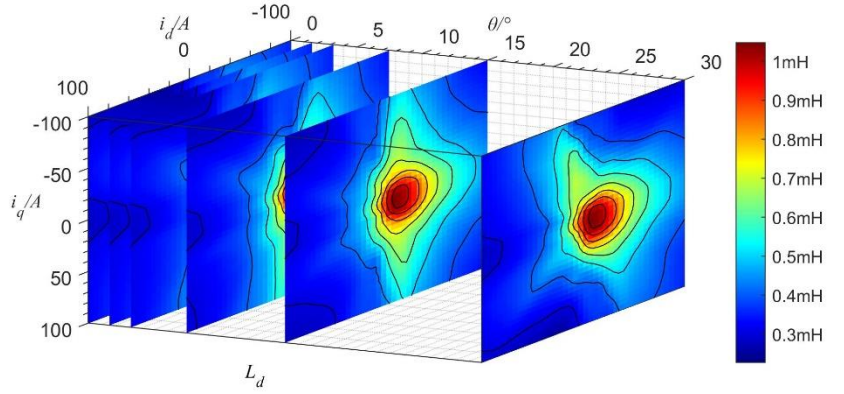


(c) Diagram of static inductance $L_d$ as a function of current and position $(i_d, i_q, \theta)$.

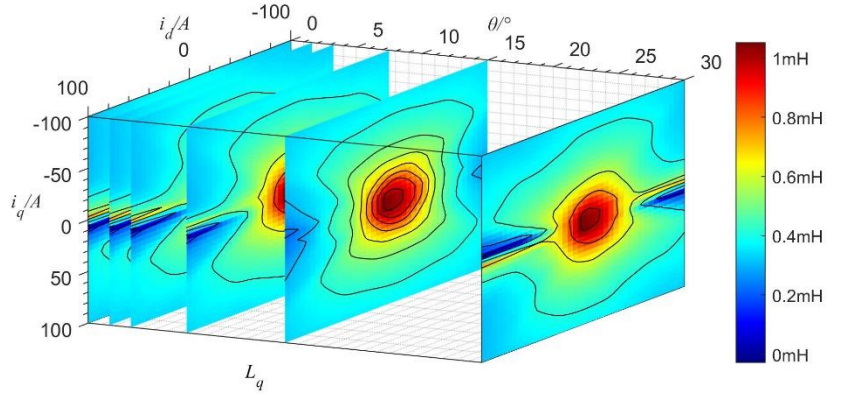


(d) Diagram of static inductance $L_q$ as a function of current and position $(i_d, i_q, \theta)$.

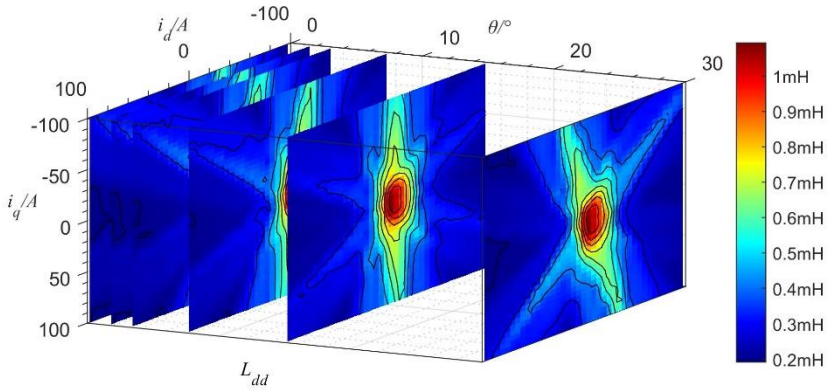


(e) Diagram of dynamic inductance $L_{dd}$ as a function of current and position $(i_d, i_q, \theta)$.

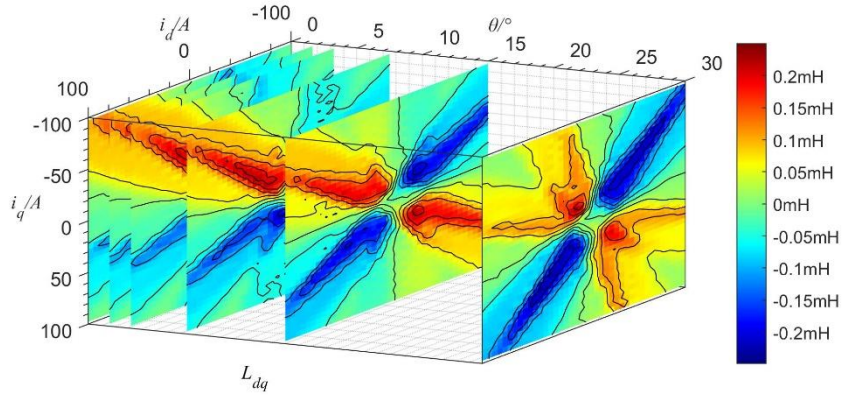


(f) Diagram of dynamic inductance $L_{dq}$ as a function of current and position $(i_d, i_q, \theta)$.

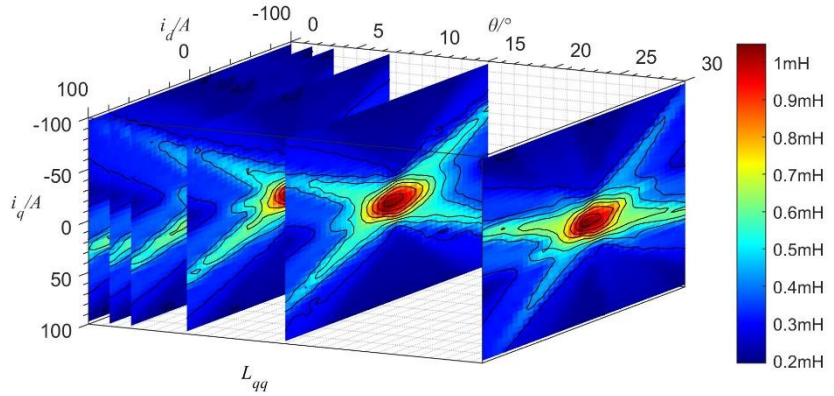


(g) Diagram of dynamic inductance $L_{qq}$ as a function of current and position $(i_d, i_q)$.

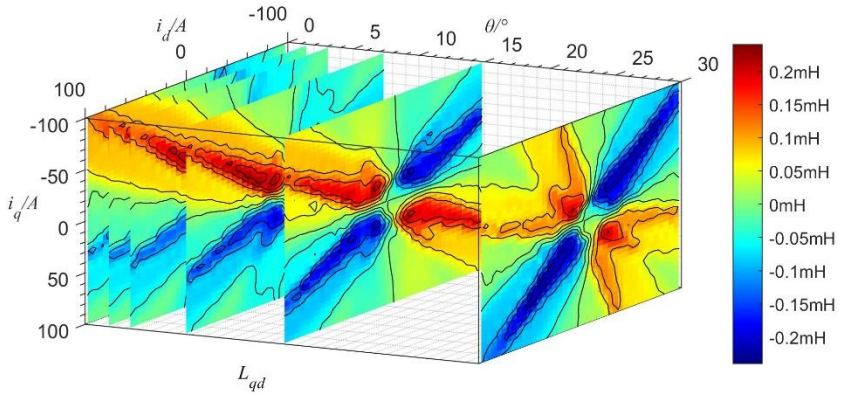


(h) Diagram of dynamic inductance $L_{qd}$ as a function of current and position $(i_d, i_q)$.

Figure 3.3 The flux linkage $\psi_d(i_d, i_q, \theta), \psi_q(i_d, i_q, \theta)$, static inductance $L_d(i_d, i_q, \theta), L_q(i_d, i_q, \theta)$, dynamic inductance $L_{dd}(i_d, i_q, \theta), L_{dq}(i_d, i_q, \theta), L_{qq}(i_d, i_q, \theta), L_{qd}(i_d, i_q, \theta)$ depicted as slices on a four-dimensional hypersurface (sliced at $\theta = 0°, 1.625°, 3.25°, 7.5°, 15°, 30°$).

Considering the substantial computational requirements of the finite element field-circuit co-simulation, to quickly validate the performance of the designed controller, the data and equations mentioned above are implemented using MATLAB/Simulink in this study, as shown in Figure 3.4. This simulation model shown below is based on table lookup and interpolation of the finite element simulation results, which offers a combination of accuracy and high speed.

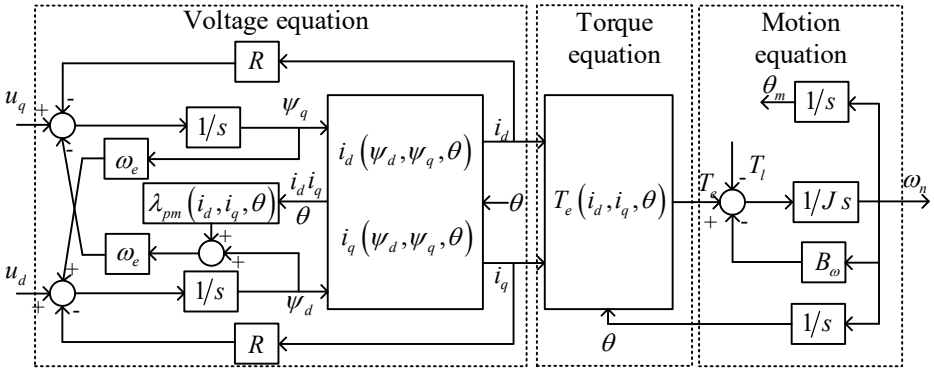


Figure 3.4 Structure diagram of nonlinear PMSM model.

## 3.2 HIGH-FREQUENCY SYSTEM MODELLING

### 3.2.1 High-Frequency model of PMSM

This section focuses on exploring the characteristics of the motor model within the frequency range of 10 kHz to 30 MHz. The high-frequency characteristics of a motor are closely related to its structure, materials, and manufacturing process. For the round wire motor manufactured in this study, using finite element or analytical methods for high-frequency modeling presents significant challenges. Therefore, this study adopts an approach based on the external characteristics of the motor to construct its high-frequency model.

First, it is necessary to accurately measure the common-mode and differential-mode external

characteristics of the motor. A three-phase PMSM has four ports: three phases A, B, and C and a ground port g. The impedance between the combined phases A // B // C, and the ground is defined as the common-mode impedance $Z_{cm}$. The impedance between any single phase and the parallel combination of the other two phases is defined as the differential-mode impedance $Z_{dm}$. The high-frequency model of the four-port network, comprising the motor windings and the motor casing, is shown in Figure 3.5.

Notably, the stator windings and the stator yoke, separated by insulating varnish and insulating paper, form the two electrodes of a parasitic capacitor. Due to the small spatial distance between the capacitor's electrodes, the influence of parasitic capacitance impedance is significant in the high-frequency range. However, the width of the air gap is much larger than the electrode spacing of the stator parasitic capacitor, so the rotor's shape and material have a minimal impact on high-frequency impedance and are typically ignored in high-frequency models [103].

Common-mode and differential-mode impedances of the motor play a crucial role in the design of electromagnetic compatibility filters. Their measurement is typically carried out using an impedance analyzer (IA) or network analyzer (NA). Studies have shown that changes in rotor speed and stator current have little impact on the high-frequency impedance characteristics of the motor. Therefore, high-frequency impedance measurements can be performed when the motor is stationary and powered off [104]. To minimize the interference of cable inductance on the measurement results, the measurement points should be as close to the motor windings as possible.

As shown in Figure 3.6, this study uses the HP 4294A impedance analyzer to measure the high-frequency impedance of the high-overload PMSM designed for this study. The resulting common-mode and differential-mode impedance data are listed in Figure C.1 in Appendix C. The measurement results indicate that the common-mode impedance $Z_{cm}$ exhibits capacitive characteristics overall, showing a 20 dB/dec attenuation trend with increasing frequency.

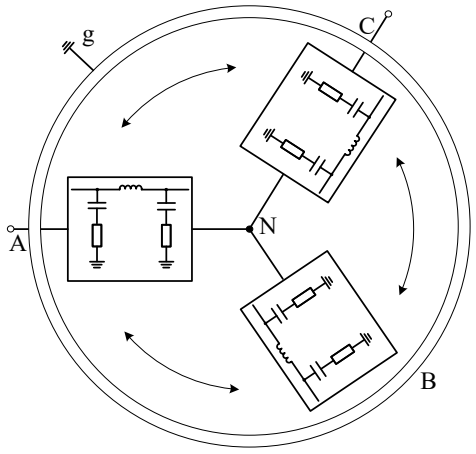


Figure 3.5 Three-phase motor HF model schematic.

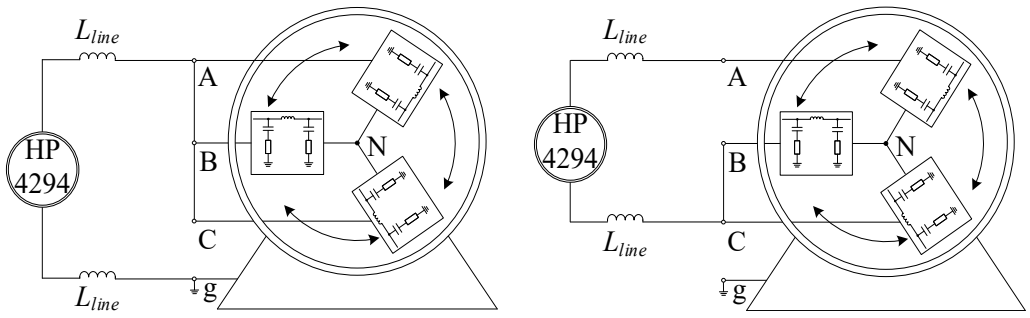


(a) CM impedance measurement wiring. (b) DM impedance measurement wiring.

Figure 3.6 High-frequency impedance measurement wiring diagram.

The simplified three-phase common-mode circuit is shown in Figure 3.7. In this circuit, $L_{d1}$, $L_{d2}$ and $L_{d3}$ represent the self-inductances of the windings, and $M$ represents the mutual inductance. The stator resistance $R_{cu}$ of the high-frequency model generally increases as the power level decreases but typically remains below 10Ω and can be neglected in the HF model. At lower frequencies, the impedance $Z_{cm}$ of the winding common-mode inductor $L_{cm}$ is negligible, causing the parasitic capacitors $C_{g1}$ and $C_{g2}$ to appear approximately in parallel. In the high-frequency range, as shown in Figure C.1, the impedance of $L_d$ is relatively high, and the impedance measurement reflects $C_{g1}$. After point D, a 20dB/dec increase is caused by the stray inductance $L_c$ of the motor winding feeder. At point D, $L_{cm}$ and $C_{g2}$ form a series resonance. From the characteristic point D on the differential-mode impedance curve, $C_{g1}$, $C_{g2}$, and common mode inductor $L_{cm}$ can be derived using (3.21), (3.22), and (3.23), where $C_E$,$C_G$ are the capacitance of point E and G and $f_D$is the frequency of point D in Figure C.1.

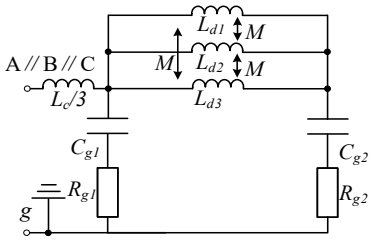


Figure 3.7 Simplified three-phase common-mode circuit.

$$C_{g1} = \frac{1}{3} C_G \tag{3.21}$$

$$C_{g2} = \frac{1}{3} C_E - \frac{1}{3} C_G \tag{3.22}$$

$$L_{cm} = \frac{1}{3(2\pi)^2 C_{g2} f_D^2} \tag{3.23}$$

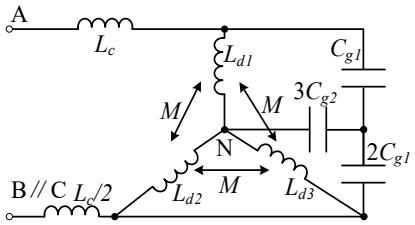


Figure 3.8 Simplified differential-mode circuit.

As the frequency increases, the differential-mode impedance curve alternates between inductive and capacitive characteristics due to the differential-mode inductance, grounding capacitance, and feeder capacitance dominating at different frequency ranges. The simplified differential-mode circuit is shown in Figure 3.8. The differential mode inductance $L_{dm}$ can be calculated at 20dB/dec impedance rise of point A using (3.24). By separating the mutual inductance using (3.25), the three-phase inductance value $L_d$ can be determined. The parasitic capacitors $C_{g1}$ and $C_{g2}$, which are in parallel with the windings, exhibit high impedance at point B, making their influence on $Z_B$ negligible. Thus, the core's ferromagnetic loss resistance $R_e$ can be obtained as shown in (3.26) [105]. Parasitic inductance and capacitance $C_{g1}$ at points D and F cause high-frequency series resonance. The impedance at these resonance points allows the calculation of $R_{g1}$ and $R_{g2}$ using (3.27) and (3.28).

$$L_{dm} = \frac{Z_A}{2\pi f_A} \tag{3.24}$$

$$L_d = L_{cm} + \frac{4}{9}L_{dm} \tag{3.25}$$

$$R_e = \frac{2}{3}Z_B \tag{3.26}$$

$$R_{g1} = \frac{2}{3}Z_D \tag{3.27}$$

$$R_{g2} = 3Z_F \tag{3.28}$$

To describe the second resonance point $C(f_C, Z_C)$ in detail, an extended model proposed in [106] is shown in Figure 3.9. The study indicates that the second resonance point is caused by the core's skin effect. This extended model calculates the parasitic inductance $L_{str}$ and mutual inductance $L_M$ using (3.29) and (3.30). The auxiliary resistance $R_{ad}$ and auxiliary capacitor $C_{ad}$ are determined through trial and error, and the modified core loss resistance $R_e'$ is estimated in the vicinity of $R_e$ to reflect the impedance characteristics of the second resonance point. Although this extended model is complex in parameterization and difficult to apply to time-domain simulation, it provides a foundation for accurately describing the second resonance point.

$$L_M = \left| L_{cm} - \frac{2}{9}L_{dm} \right| \tag{3.29}$$

$$L_{str} = L_d - L_M \tag{3.30}$$

In this study, $R_{e2} = R_e - R_{e1}$ is introduced to represent the change in iron loss due to the skin effect, where $R_{e2}$ is taken as the impedance value $Z_C$ at point C. A common-mode resonant branch with a series resonant

frequency of $f_C$ is added, as shown in Figure 3.10(a). According to (3.31), the auxiliary capacitor $C_{ad}$ is typically taken as one-tenth of the total capacitance of the single-phase winding to ground [107-108]. The auxiliary inductance $L_{ad}$ can be calculated using (3.32).

$$C_{ad} = \left(C_{g1} + C_{g2}\right) / 10 \tag{3.31}$$

$$L_{ad} = \frac{1}{4\pi^2 C_{ad} f_C^2} \tag{3.32}$$

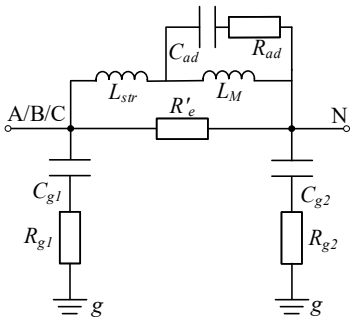


Figure 3.9 Expanded single-phase motor model.

At frequencies above 10MHz, the motor feeder acts as a single-turn inductor, whose value can be determined from the 20dB/dec rise in the high-frequency impedance curve, $L_c = Z_D \,/\, 2\pi f_D$. Through the equivalent circuit transformation, the proposed high-frequency common-mode and differential-mode motor models are shown in Figures 3.10(b) and 3.10(c).

By parameterizing the high-frequency model of the motor, the corresponding high-frequency model parameters shown in Figure 3.10 can be obtained, with the detailed parameters listed in Table C.1 in Appendix C.

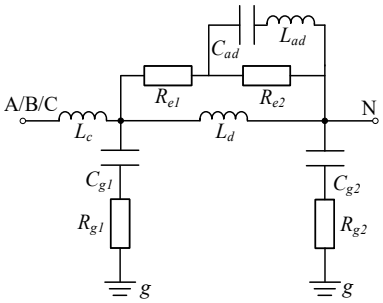


(a) Single-phase circuit model.

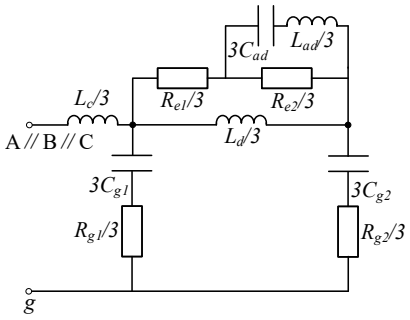


(b) Common-mode circuit model.

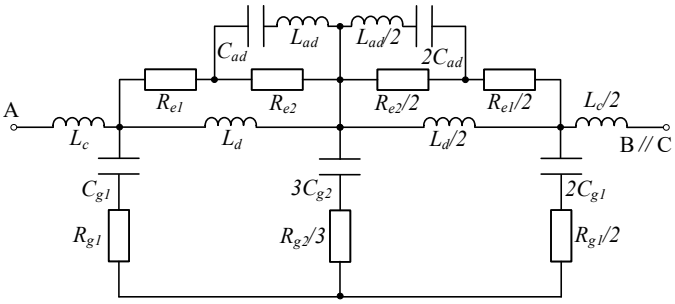


(c) Differential-mode circuit model.

Figure 3.10 The proposed high-frequency motor model.

Figure 3.11 illustrates the external characteristics of the motor impedance obtained from measurements and the impedance values calculated using the high-frequency model. The red dashed line represents the model impedance without considering the second resonant point, while the black solid line represents the model impedance with the second resonant point considered.

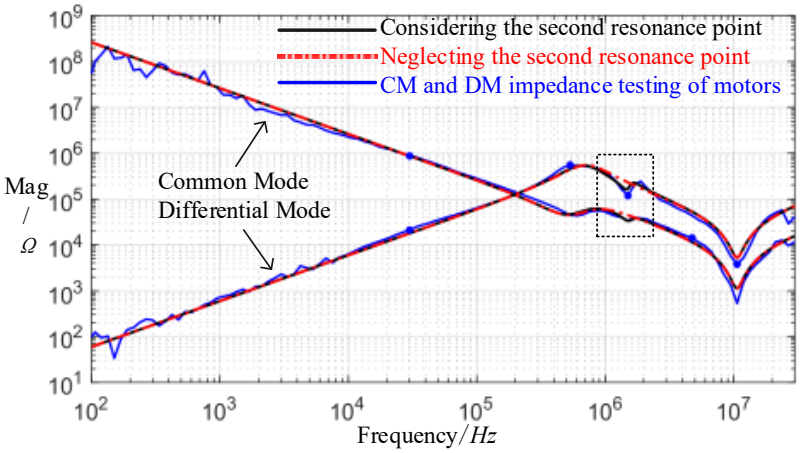


Figure 3.11 Measuring and modeling results of the motor's CM and DM impedance.

It is evident from Figure 3.11 that the high-frequency model of the motor, which includes the second resonant point, demonstrates higher accuracy in the frequency range of 10 kHz to 30 MHz. Notably, the accuracy is significantly improved at the second resonant point, as indicated by the dashed box.

### 3.2.2 High-Frequency model of Controller

To establish a high-frequency model of the system, it is necessary to model the controller. Compared to the motor, the controller is more prone to failure, often requiring rectification to address electromagnetic compatibility issues. Unlike modeling methods based on external characteristics, finite element modeling (FEM) allows for simulation and verification before the production of circuit boards, reducing rectification costs and cycle time. This study employs the FEM to model the controller, using the Q3D quasi-static FEM electromagnetic field simulation tool to extract the parasitic RLCG (Resistance, Inductance, Capacitance, and Conductance) parameters of the circuit board and generate the equivalent circuit.

The flowchart for extracting PCB parasitic parameters is shown in Figure 3.12. The parasitic parameters of the controller mainly include line inductance, capacitance, bus parasitic inductance, capacitance, and component package inductance.

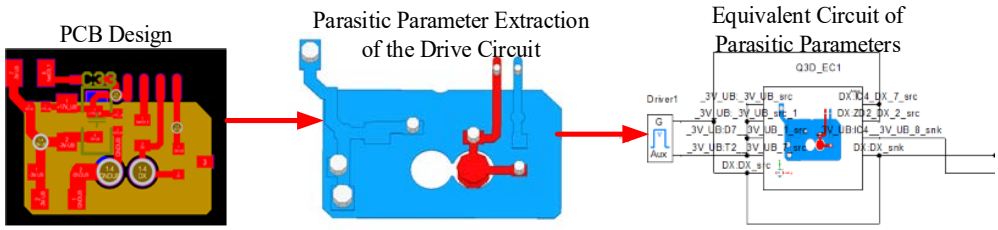


(a) Parasitic parameter extraction for the drive board.

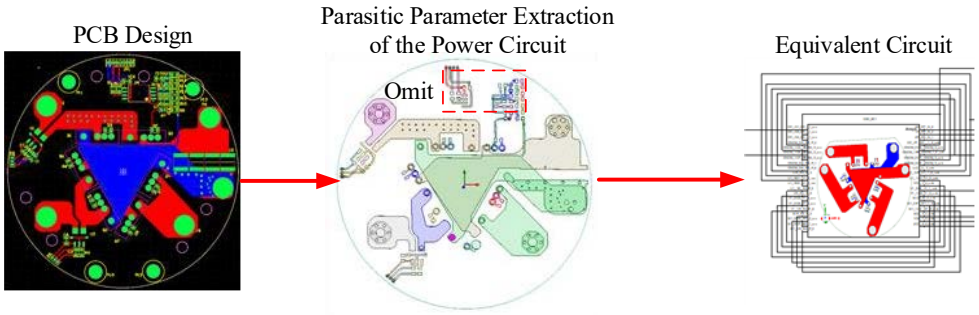


(b) Parasitic parameter extraction for the power board.

Figure 3.12 PCB parasitic parameter extraction.

Due to the compact component layout and complex routing in the PCB designed for this study, the mesh resolution cannot be too low. The numerous chip pins result in large RLCG parameter tables for each network, but many irrelevant parameters do not improve calculation accuracy. Therefore, to ensure computational efficiency, this study simplifies the circuit to some extent. Additionally, a finite element model of the cables used in the experiment is generated based on parameters such as wire diameter, conductor, and insulation materials. The dynamic model of the Silicon Carbide (SiC) Metal Oxide Semiconductor Field Effect Transistor (MOSFET) is established according to the device manual.

### 3.2.3 EMI Prediction Model of Electric Drive System

3.2.3.1 Common-mode Conducted EMI Coupling Path

In motor drive systems, there are numerous common-mode loops. However, in many cases, the common-mode current caused by distributed capacitance is very weak and is usually ignored during analysis. The common-mode interference current primarily originates from the following three parts:

(1) Distributed capacitance between the DC bus cable and the reference ground;

(2)Distributed capacitance between the motor windings and the stator housing, and between the motor bearing inner ring and the housing;

(3)Distributed capacitance between the power transistor devices and the heat sink.

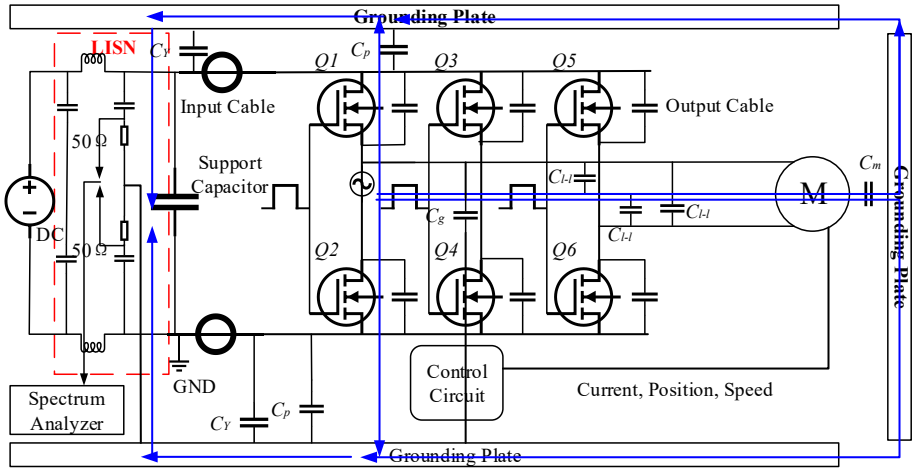


Figure 3.13 Coupling path of the common-mode current on the DC side.

The coupling path of the common-mode current on the DC side is shown in Figure 3.13. In the figure, $C_p$ represents the parasitic capacitance between the switching transistor and the ground, $C_{bg}$ represents the distributed capacitance between the midpoint of the bridge arm and the ground, $C_m$ represents the parasitic capacitance between the motor housing and the ground, and $C_y$ represents the parasitic capacitance between the DC bus and the ground. This chapter only considers the primary sources of common-mode electromagnetic interference (EMI) and components. The coupling path of the common-mode interference current in the EMI test circuit is as follows: power transistor - distributed capacitance between the power transistor and the heat sink - line impedance stabilization network - support capacitor - DC bus cable - bridge arm midpoint. The common-mode voltage generated by the switching transistor is grounded through the following paths: 1) grounded through the bridge arm inter-electrode capacitance and the parasitic capacitance of the positive and negative DC buses; 2) grounded through the parasitic capacitance of the motor windings to the stator housing; and 3) grounded through the parasitic capacitance between the stator windings and the rotor, forming a common-mode induced voltage on the rotor core and ultimately grounding through the parasitic capacitance of the bearing oil film.

3.2.3.2 Differential-Mode Conducted Electromagnetic Interference Coupling Path

In circuit analysis, once an interference source is generated, the resulting differential-mode interference current flows through low-impedance loops in the system, as shown in Figure 3.14. The conduction and cutoff of power switches alter the paths of differential-mode currents. The following example illustrates the scenario when switches Q1, Q4, and Q6 are conducting.

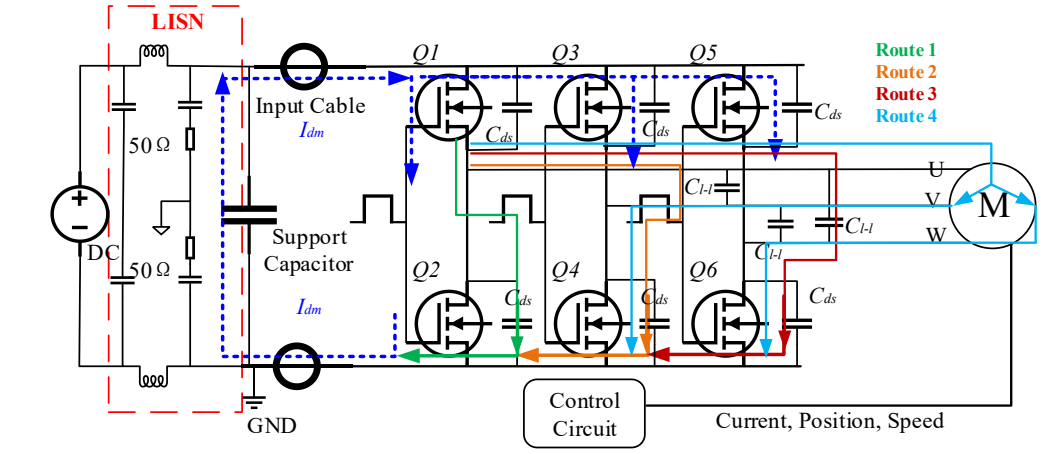


Figure 3.14 Conduction path of differential-mode current in the motor drive system.

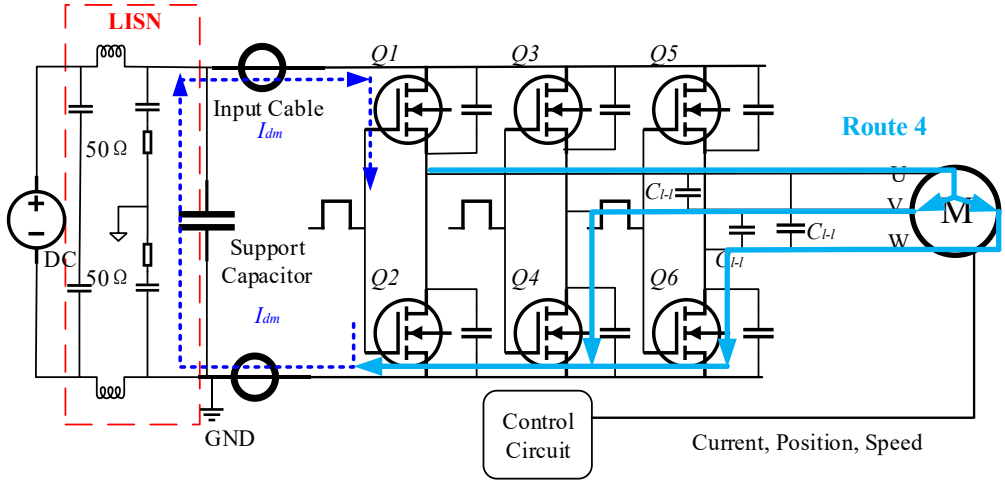


Figure 3.15 Differential-mode interference current path on the DC side.

When Q1 is conducting, the differential-mode interference current generated on the DC side can flow through paths 1, 2, 3, and 4 in the system. The flow path is mainly influenced by the parasitic parameters in the system. Typically, in the conducted EMI test frequency range, the system's parasitic parameters satisfy $Z_M \ll Z_{ds}$ and $Z_M \ll Z_{C_{l-l}} / 2$, where $Z_M$ represents the motor phase winding impedance, expressed as $(|3/2\,R_m + j3\pi f L_m| \ll 1 / 2\pi f C_{ds})$ and $(|\frac{3}{2R_m} + j3\pi f L_m| \ll 1 / 4\pi f C_{l-l})$, with $C_{l-l}$ indicating the parasitic capacitance between different phase lines and $C_{ds}$ indicating the MOSFET inter-electrode capacitance. In this case, the differential-mode interference current on the DC side mainly flows through path 4, as shown in Figure 3.15. Specifically, the interference current flows from the positive terminal of the DC power supply, through the MOSFET bridge midpoint, then through the output cable, motor winding, and cable, finally returning to the negative terminal of the DC power supply via power transistors Q4 and Q6.

In the conducted EMI test frequency range, when the system's parasitic parameters meet the conditions $Z_{ds} \ll Z_{C_{l-l}}$ and $Z_M \gg Z_{C_{l-l}} / 2$, where $Z_M$ represents the motor phase winding impedance, expressed as $(|3/2\,R_m + \mathrm{j}3\pi f L_m| \ll 1 / 2\pi f C_{ds})$ and $(|\frac{3}{2R_m} + \mathrm{j}3\pi f L_m| \ll 1 / 4\pi f C_{l-l})$. In this case, the differential-

mode interference path on the AC output side is shown in Figure 3.16: from the bridge midpoint, through the output cable and the parasitic capacitance $C_{l-l}$ between lines, flowing through power transistors Q6 and Q4, and finally returning to the bridge midpoint via the inter-electrode capacitance of Q2. As shown, the interference current flows between the output cables.

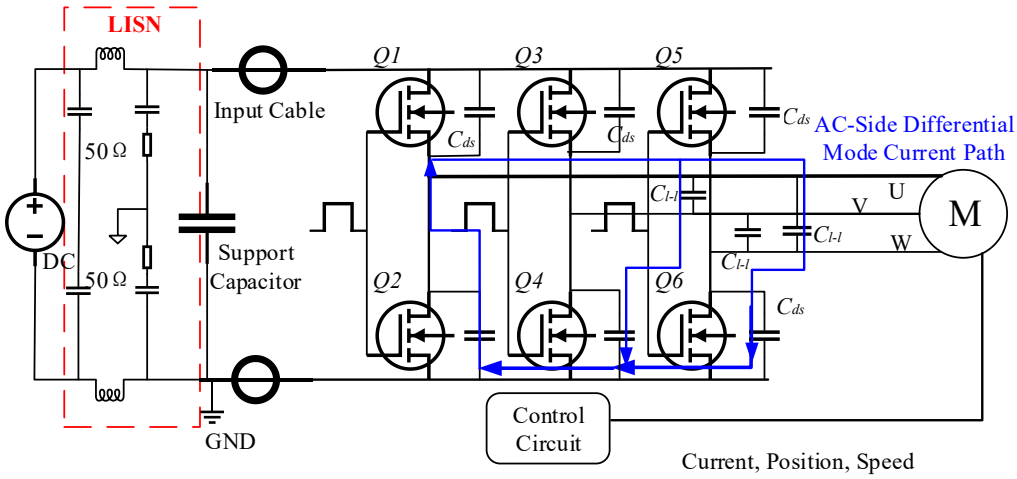


Figure 3.16 Differential-mode interference current path on the AC side.

3.2.3.3Prediction Model of Common-mode EMI Current

The above analysis reveals that the differential-mode interference current and common-mode loops are independent of each other. Therefore, predictions of common- and differential-mode interference current noise can be conducted separately. Common-mode current forms a large loop between the power supply and ground, and due to its large loop area, it can easily lead to radiated electromagnetic interference emissions exceeding standards.

The common-mode EMI prediction model simulation is shown in Figure 3.17, using Simulink/SIwave/Simplorer joint simulation. The fitted SiC MOSFET model is imported into Simplorer, and the RLCG models of the drive circuit, main circuit, and cables are extracted using SIwave. A 2D finite element motor model is built in Maxwell, with motor output current and rotor position input into Simulink. The motor control algorithm is calculated in Simulink, and ultimately, six PWM signals are output from Simulink to control the three-phase full bridge.

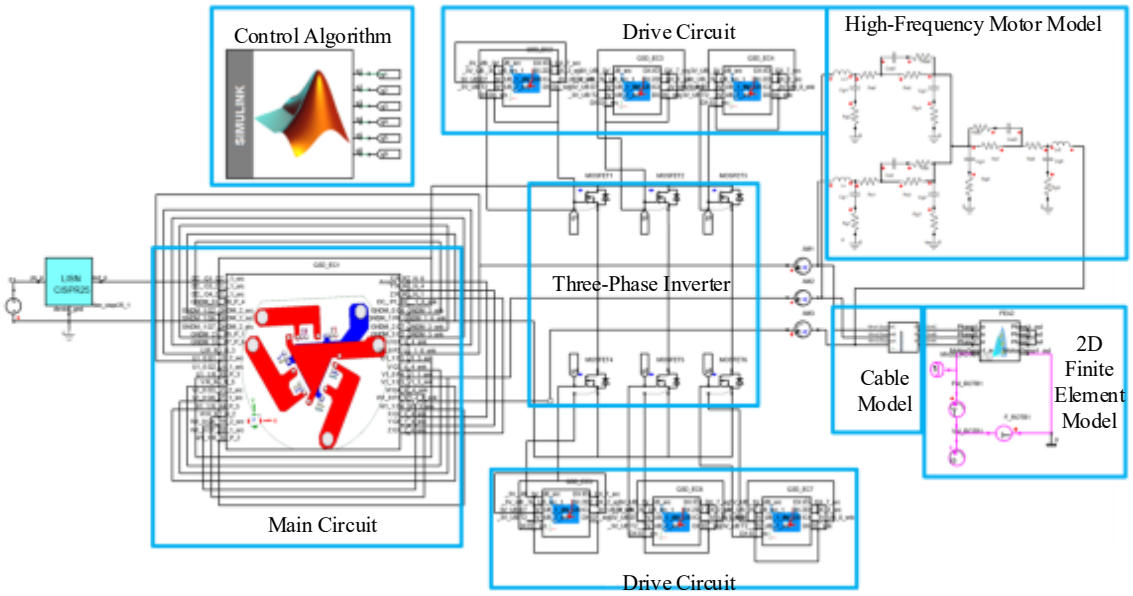


Figure 3.17 Block diagram of the conducted EMI current prediction model.

Control signals are generated in the Matlab environment, while the inverter circuit and high/low-frequency motor models are computed in Simplorer and Maxwell, respectively. To ensure accurate co-simulation, consistent simulation time settings and step sizes must be applied across both platforms. For a target frequency of 30 MHz, the simulation step size is set to 15 nanoseconds or less, satisfying the Nyquist sampling theorem and enabling accurate capture of noise distribution within this frequency range. To speed up simulation stabilization, initial currents are set close to steady-state values, and simulating around ten switching cycles can provide common-mode EMI current data.

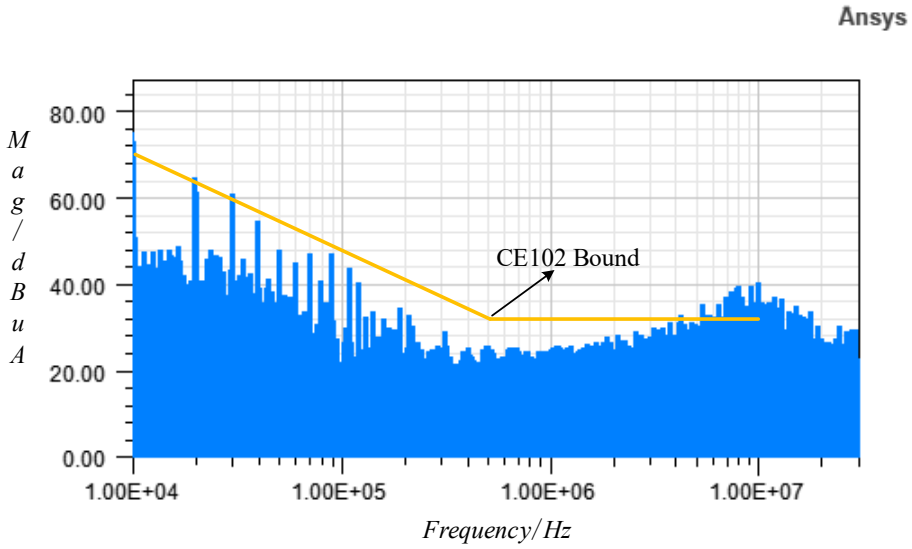


Figure 3.18 Predicted results of common-mode conducted EMI currents.

As shown in Figure 3.18, with constant switching frequency SVPWM modulation, the predicted common-mode EMI current exceeds the CE102 standard limit. This simulation result highlights the challenges in common-mode EMI management using traditional modulation strategies, underscoring the necessity of

optimizing modulation strategies to meet stringent EMI standards. Chapter 4 will use the above current prediction simulation model to predict and analyze common-mode EMI currents under different modulation methods.

## 3.3 SUMMARY

An accurate mathematical model is crucial for in-depth research on the current loop control algorithm of high-speed, high-overload PMSMs and the spread spectrum modulation strategy of high-speed, high-overload electric drive systems. The content of this chapter is summarized as follows:

The impact of stator core magnetic saturation on inductance under high overload conditions was analyzed. A nonlinear motor model considering cross-saturation was established, providing a basis for the discrete complex vector current control strategy based on flux linkage data presented in Chapter 3.

A nonlinear motor model considering slotting effects was introduced, laying the theoretical foundation for the programmed spread spectrum modulation strategy considering cross-saturation and slotting effects proposed in Chapter 4.

A high-frequency motor model considering the skin effect and its efficient parameterization method was proposed. This model is highly accurate in the range of 10kHz to 30MHz, with fewer parameters and easy parameterization, suitable for both time-domain and frequency-domain simulations. Additionally, based on this high-frequency model, a common-mode EMI current prediction model was constructed to verify the effectiveness of the hybrid spread spectrum modulation algorithm in suppressing EMI conducted current in Chapter 4.

# Chapter 4: Current Loop Control Considering Saturation

To improve the performance and range of the battery-powered automated devices, motor control systems should be able to work at high-speed and peak-torque operating modes for short durations, which presents a challenge in the design of the current loop.

On the one hand, for the high-speed operating mode, the current loop performance deteriorates with the speed increase due to the computation and modulation delay. In order to improve the stability of the current loop controller at high speeds, the time-lag issue can be addressed by increasing the switching frequency and sampling frequency. However, switching frequency and sampling frequency are limited by switching loss and computing resources. Therefore, in order to reduce the sampling update delay, it is possible to model and compensate for the delay.

On the other hand, in the peak-torque mode, the current is several times the rated value, resulting in significant parameter changes. When the operating current exceeds the knee point current, the saturation of the iron core will lead to a significant decrease in inductance. These parameter mismatches will influence the stability and fast response of the current loop.

In this chapter, a discrete-time current controller utilizing flux-linkage data-based complex vector is proposed to address the instability issue in the current control of synchronous motors during high-power output. Firstly, an offline flux-linkage measurement method for the model considering the cross saturation in Chapter II is introduced, and the flux-linkage data are used to deduce the symmetrical complex vector controller. Then, the influence of the latch and delay of inverters on the line voltage of machines at high speed is analyzed and compensated in the designed complex vector controller. The proposed controller can deal with the inductance mismatch issues caused by iron core saturation. It offers the advantage of a simple structure, requiring the tuning of only a single parameter. The controller can be adopted in the current loop of high-speed saturated salient or nonsalient PMSMs and reluctance motors. Lastly, simulations and experiments verify the effectiveness of the proposed method.

## 4.1 PI CONTROLLER BASED ON INTERNAL MODEL PRINCIPLE

A decoupled PI controller based on the internal model principle is the most widely used solution for its simple structure and good performance. In this section, a brief introduction to the controller is given. For diagonal IMC (DIMC), decoupling should be implemented first to remove the cross-coupling of direct and quadrature axis terms in (4.1). Equation (4.1) represents two separate SISO systems, where $u_d'$ and $u_q'$ are direct and quadrature axes voltages after decoupling. To achieve a good dynamic performance, the voltage drop caused by crossover inductance and permanent flux linkage $\omega_e[-L_q i_q \quad L_d i_d + \lambda_{pm}]^T$ should be added back to

$[u'_d(s) \quad u'_q(s)]^T$ during realization.

$$\begin{bmatrix} u'_d \\ u'_q \end{bmatrix} = \begin{bmatrix} u_d \\ u_q \end{bmatrix} - \omega_e \begin{bmatrix} -L_q i_q \\ L_d i_d + \lambda_{pm} \end{bmatrix} = R \begin{bmatrix} i_d \\ i_q \end{bmatrix} + \begin{bmatrix} L_d & 0 \\ 0 & L_q \end{bmatrix} \frac{d}{dt} \begin{bmatrix} i_d \\ i_q \end{bmatrix} \tag{4.1}$$

Equation (4.2) can be obtained from (4.1) in the frequency domain, where s denotes the Laplace factor.

$$\begin{bmatrix} i_d \\ i_q \end{bmatrix} = G_{Plant}(s) * \begin{bmatrix} u'_d(s) \\ u'_q(s) \end{bmatrix} = \begin{bmatrix} \frac{1}{R + sL_d} & 0 \\ 0 & \frac{1}{R + sL_q} \end{bmatrix} \begin{bmatrix} u'_d(s) \\ u'_q(s) \end{bmatrix} \tag{4.2}$$

According to the DIMC principle, the current controller can be designed as (4.3), where $K_d = \alpha L_d$, $K_q = \alpha L_q$, $T_{id} = \frac{L_d}{R}$ ,$T_{iq} = \frac{L_q}{R}$, and $\alpha$ is the pending parameter [109].

$$C(s) = \begin{bmatrix} K_d \left(1 + \frac{1}{sT_{id}}\right) & 0 \\ 0 & K_q \left(1 + \frac{1}{sT_{iq}}\right) \end{bmatrix} \tag{4.3}$$

The closed-loop transfer function $G_{clPI}(s)$ is a first-order lag, as shown in (4.4). The expected bandwidth is determined by the only unknown parameter $\alpha$. When $\alpha = s$, Equation (4.4) becomes a 0.5-scaled diagonal matrix, corresponding to –3 dB, which indicates the system bandwidth.

$$G_{clPI}(s) = \frac{C(s)G_{Plant}(s)}{1 + C(s)G_{Plant}(s)} = \begin{bmatrix} \frac{\alpha}{s + \alpha} & 0 \\ 0 & \frac{\alpha}{s + \alpha} \end{bmatrix} \tag{4.4}$$

Because Laplace transformation is only applicable to the linear time-invariant system, theoretically speaking, the parameters in (4.3) should be fixed in the control period. When saturation occurs, the inductance and thus the stability margin will decrease, leading to the overshoot and even oscillation of the current. The delay of the control system is also neglected, and therefore, the expected bandwidth $\alpha$ cannot be achieved. The controller proposed below, which is based on the flux-linkage state and data, can handle these issues.

## 4.2 THE EFFECT OF LATCH AND DELAY IN INVERTERS

With the development of digital control, DSP and insulated gate bipolar transistor (IGBT) have been widely used in the machine control area. The current is sampled, transformed, and input into the current loop to calculate the voltage command value. Then, the converter outputs the voltage after a short delay, which is relative to the sampling period. If the machine is working in high-speed mode, the delay in the sampling–updating–outputting procedure cannot be neglected. Compared to synchronous SSSU, synchronous DSDU can double the sampling frequency and halve the delay time without increasing the switching loss.

As shown in Figure 4.1, sampling is synchronous with carrier waves. In DSDU, sampling occurs at the peak and valley value of carrier waves, and updating occurs after sampling. For example, the DSP samples at $t_1$ and updates at $t_2$. The ordinary seven-segment voltage vector is divided into two four-segment voltage vectors, namely $\overrightarrow{u_{dq}}(k-2)$ of $t_1 - t_2$ and $\overrightarrow{u_{dq}}(k-1)$ of $t_2 - t_4$. It can be approximately regarded that the average value of $\overrightarrow{u_{dq}}(k-1)$ occurs at the midpoint of $t_2$ and $t_4$, namely $t_3$. The voltage vector command value corresponding to the sample time $t_1$ is not applied to the winding until the $t_3$ moment. The delay between

sampling and outputting is equal to $\frac{3T_s}{2}$.

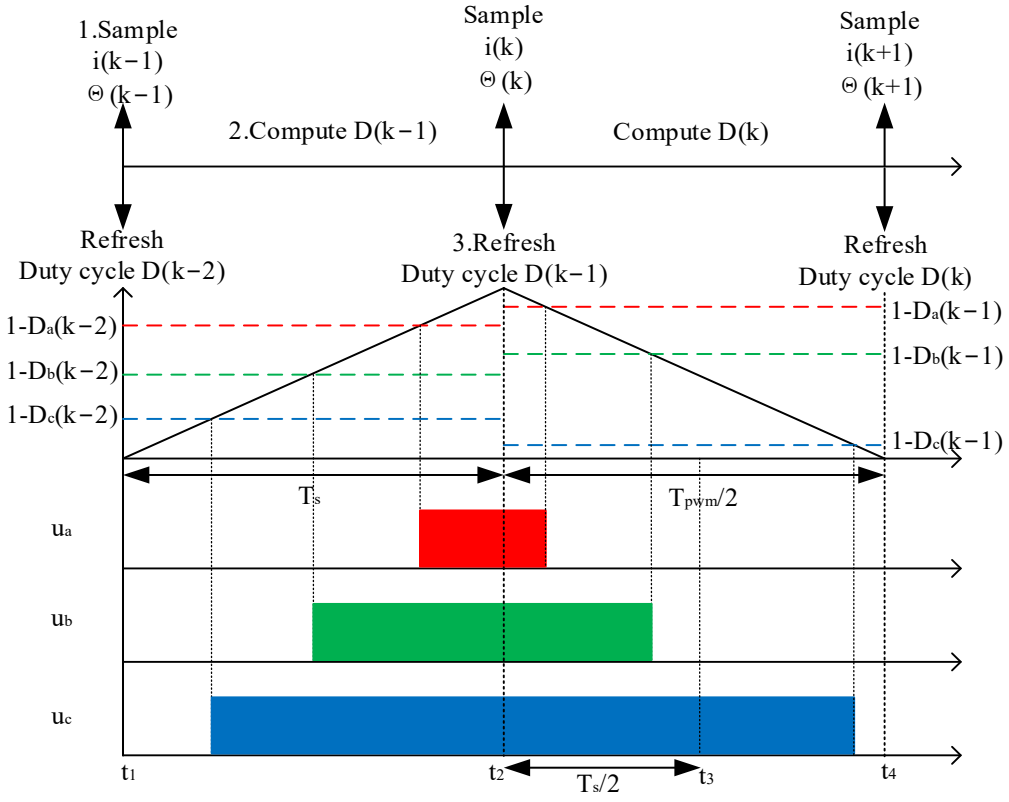


Figure 4.1 Chronological chart of sampling and outputting of DSDU.

To illustrate the deviation between the given value and the output value, Figure 4.2 presents a two-pole machine model with the rotor rotating (aligned with the direct-axis). Supposing the rotor speed $\omega_e$ is steady, the rotor position of the north pole at the three sampling instants $t_1$, $t_2$ and $t_4$ are $d(t_1)$, $d(t_2)$, $d(t_4)$. After sampling at $t_1$ and computing during $t_1 - t_2$, the duty cycle information is updated to the register at $t_2$. During the outputting time $t_2 - t_4$, the rotor still rotates at the speed of $\omega_e$. The actual output voltage vector during $t_2 - t_4$ can be calculated by (4.5),

$$\overrightarrow{u_{dq}}(t) = \overrightarrow{u_{dq}^*}(k)e^{j\theta(k)}e^{-j\theta(k)-j\omega_e t}, t \in [t_2, t_4] \tag{4.5}$$

where $e^{-j\theta(k)-j\omega_e t}$ and $e^{j\theta(k)}$ denote Park's transformation factor and inverse Park's transformation factor. $\overrightarrow{u_{dq}^*}(k)$ denotes the voltage command value. The average output voltage is given in (4.6).

$$\overrightarrow{u_{dq}}(k+1) = \frac{1}{T_s}\int_{T_s}^{2T_s}\overrightarrow{u_{dq}}(t)\,d\tau = \frac{\frac{1}{2}\omega_e T_s}{Sin\left(\frac{\omega_e T_s}{2}\right)}\overrightarrow{u_{dq}^*}(k)e^{-j\frac{3}{2}\omega_e T_s} \tag{4.6}$$

Equation (4.6) shows that the magnitude error is $\omega_e T_s/2Sin(\omega_e T_s/2)$, and the direction error is $e^{-j3\omega_e T_s/2}$. With the increasing $\omega_e$, the errors become non-ignorable. The errors should be compensated in the control system.

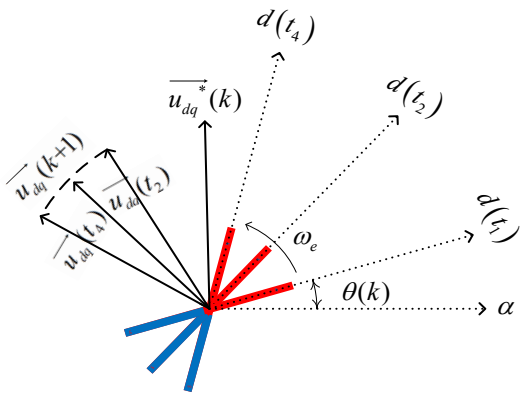


Figure 4.2 Voltage complex vector plot of a rotating PMSM.

## 4.3 CONTROLLER BASED ON FLUX-LINKAGE DATA

Define intermediate voltage $v_d$ and $v_q$, as shown in (4.7). Deduced from (4.7), Equation (4.8) describes the relationship between voltage and flux linkage.

$$\begin{bmatrix} v_d \\ v_q \end{bmatrix} = \begin{bmatrix} u_d \\ u_q \end{bmatrix} - R\begin{bmatrix} i_d \\ i_q \end{bmatrix} - \omega_e \begin{bmatrix} 0 \\ \lambda_{pm}(i_d, i_q) \end{bmatrix} \tag{4.7}$$

$$\frac{d}{dt}\begin{bmatrix} \psi_d(i_d, i_q) \\ \psi_q(i_d, i_q) \end{bmatrix} = \begin{bmatrix} 0 & \omega_e \\ -\omega_e & 0 \end{bmatrix}\begin{bmatrix} \psi_d(i_d, i_q) \\ \psi_q(i_d, i_q) \end{bmatrix} + \begin{bmatrix} v_d \\ v_q \end{bmatrix} \tag{4.8}$$

The complex vector form of (4.8) is shown in (4.9), where $\vec{\psi}(i_d, i_q) = [\psi_d(i_d, i_q) \quad \psi_q(i_d, i_q)]^T$, and $\vec{v} = [v_d \quad v_q]^T$. The mechanical time constant is much bigger than the electrical time constant, and the variation of $\omega_e$ can be neglected. Equation (4.9) is a state-space representation that describes a SISO linear time-invariant system.

$$\frac{d\vec{\psi}(i_d,i_q)}{dt} = -j\omega_e\vec{\psi}(i_d, i_q) + \vec{v} \tag{4.9}$$

The discrete-time solution of (4.9) is shown in (4.10). With the delay in (4.6) considered, the transfer function of the plant $G_{Plant}(z)$ can be written as (4.11).

$$\vec{\psi}(k+1)|_{i_d,i_q} = e^{-j\omega_e T_s}\vec{\psi}(k)|_{i_d,i_q} + \frac{1}{j\omega_e}(1 - e^{-j\omega_e T_s})\vec{v}(k) \tag{4.10}$$

$$G_{Plant}(z) = \frac{\vec{\psi}(z)|_{i_d,i_q}}{\overrightarrow{v^*}(z)} = \frac{1}{j\omega_e z}\frac{1 - e^{-j\omega_e T_s}}{ze^{j\frac{3}{2}\omega_e T_s} - e^{j\frac{1}{2}\omega_e T_s}}\frac{\frac{1}{2}\omega_e T_s}{Sin\left(\frac{\omega_e T_s}{2}\right)} \tag{4.11}$$

Based on the accurate discrete model, the controller $G_c(z)$ in (4.12) can be obtained without discretization procedure. As shown in (4.13), the closed-loop transfer function $G_{clCV}(z)$ is of simple structure

$$G_c(z) = \frac{k(e^{j\omega_e T_s} - 1)}{T_s(e^{-j\omega_e T_s} - 1)}\frac{ze^{j\omega_e T_s} - 1}{1 - z} \tag{4.12}$$

$$G_{clCV}(z) = \frac{G_c(z)G_{Plant}(z)}{1 + G_c(z)G_{Plant}(z)} = \frac{k}{z^2 - z + k} \tag{4.13}$$

Figure 4.3 presents the structure of the proposed controller. First, the feedback current $(i_d, i_q)$ is given to the look-up table $\psi_d(i_d, i_q)$ and $\psi_q(i_d, i_q)$ to acquire $\vec{\psi}$. The intermediate voltage $\overrightarrow{v^*}$ can be acquired from $\vec{\psi}$. Then, the voltage drop across the resistor and back EMF are added, and the voltage reference value $\overrightarrow{u^*}$ is

given to the inverter. The complex form has to be transformed into the scalar form using the Euler equation to be implemented in DSP. To enhance code execution efficiency, the flux linkage lookup table as well as sine and cosine values can be precomputed and stored in RAM during the initialization phase of the digital signal processor, TI DSP28335, thereby enabling real-time execution of the control algorithm on this platform. The flux-linkage table should be large enough to cover the whole dynamic process of the current.

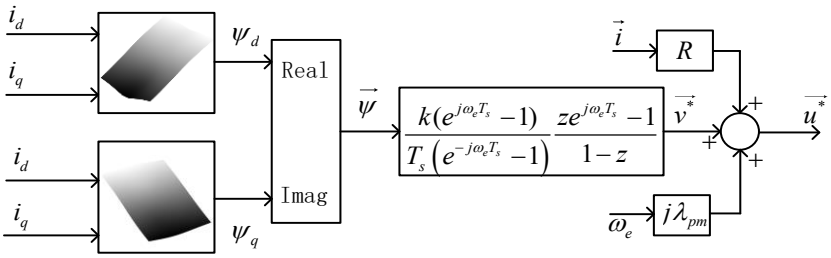


Figure 4.3 Structure of complex vector current controller based on the flux-linkage data.

## 4.4 SIMULATION RESULTS

The simulation of the PI control and complex vector control is carried out in Matlab/Simulink. The discrete-time step is set as 1μs, and the switching frequency is set as 10kHz. The motor module is based on (4.7) and the inductance table [110]. Voltage-controlled voltage source (VCVS) with 1 μs delay is adopted to represent the three-phase full-bridge voltage source inverter (VSI). The complex vector controller $G_c(z)$ multiplied with $\frac{1}{2}\omega_e T_s / Sin(0.5\omega_e T_s)\, e^{-j\frac{1}{2}\omega_e T_s}$ is used to compensate for the time delay between VCVS and VSI.

The step response of the closed-loop transfer function of the complex vector controller $G_{clCV}(z)$ with $k = 0.15,0.3,0.45$ is simulated, and the results are presented in Figure 4.4. According to the simulation result, $k$ is set to 0.3 in the following. The $-3$dB bandwidth of the closed-loop transfer function $G_{clCV}(z)$ is $12{,}947 rad/s$ when the sampling frequency is 20kHz. The $-3$dB bandwidth of $G_{clCV}(z)$ is $6473 rad/s$ when the sampling frequency is 10kHz.

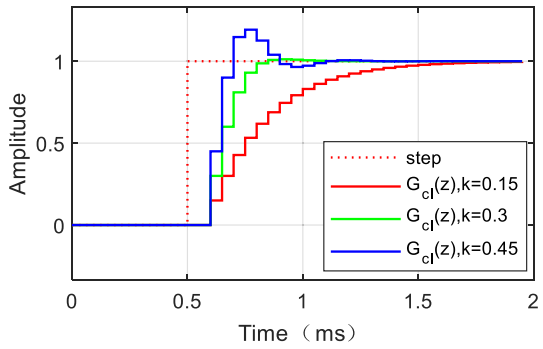


Figure 4.4 Step response of ideal closed-loop transfer function with different parameters.

As shown in Figure 4.5, the Bode diagram of the PI control and complex vector control system has the same $-3$dB bandwidth at $\alpha = 12{,}947 rad/s$ and $k = 0.3$. However, considering the time-lag effect, the bandwidth of the PI controller is limited. In engineering practice, bandwidth is usually set as $\alpha = 1/2T_{delay}$.

Since $T_{delay} = 75\mu s$ in DSDU, the parameter $\alpha$ should be $6667 rad/s$. Large currents are assigned to the winding to generate short-time peak torques; thus, the motor in this research can be highly saturated, which means that a smaller $\alpha$ is more suitable. The simulation of the two controllers in different working conditions is shown in the following sections.

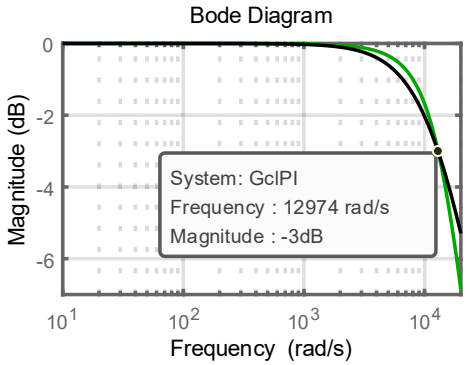


Figure 4.5 Bode diagram of closed-loop transfer functions (Green line, complex vector controller; Black line, PI controller).

### 4.4.1 Simulation of the Locked Saturated Machine

To verify the effectiveness of high-current control, the speed is set close to 0 rpm, and the sampling frequency is 20kHz. According to the simulation and experiment, the control parameters are set as follows, $\alpha = 4000 rad/s$, $k = 0.3$. In practice, for a saturated salient machine, the dq axes current command trajectories are given through a look-up table to achieve maximum torque per ampere (MTPA) control performance. In this research, the MTPA look-up table is not experimentally calibrated, and the direct axis command current is set as −0.2 times the quadrature one. The quadrature axis current is given an incremental increase of 15 A each 5 ms from 0 to 60 A. The direct axis current is given a step decrease of 3 A each 5 ms from 0 to −12 A.

As shown in Figures 4.6 and 4.7, the current oscillation appears when using the PI controller to deal with the saturated machine. “SR” is the abbreviation of step response in this research. With the increasing severity of the saturation, the deviation between the current trajectory and step response of the closed-loop transfer function $G_{clPI}(s)$ increases. As for the complex vector controller, the current always follows the step response of the closed-loop transfer function $G_{clCV}(z)$, no matter how saturated the motor is.

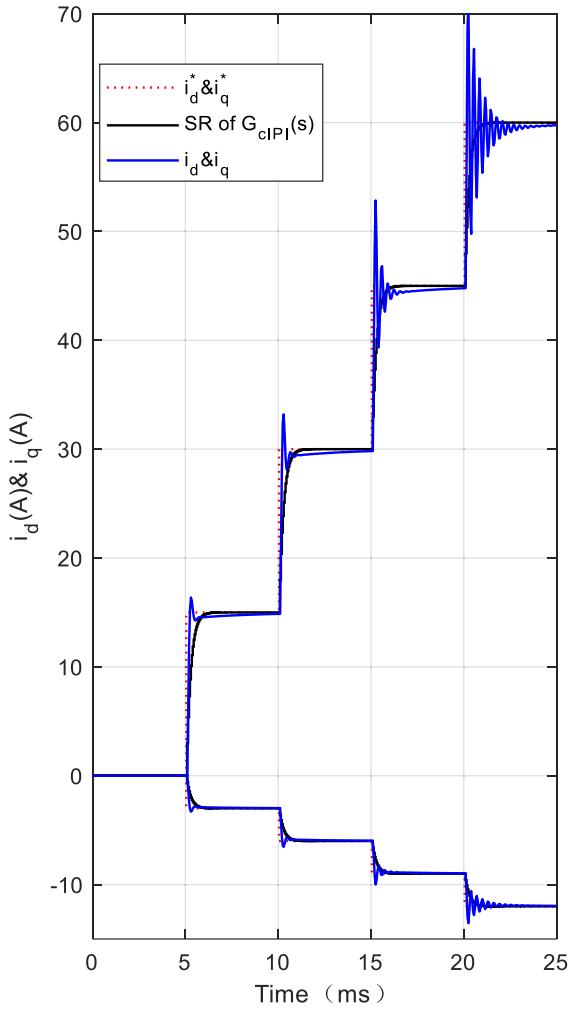


Figure 4.6 Simulation result of PI controller based on DIMC ($\alpha = 4000 rad/s$) of the locked saturated machine.

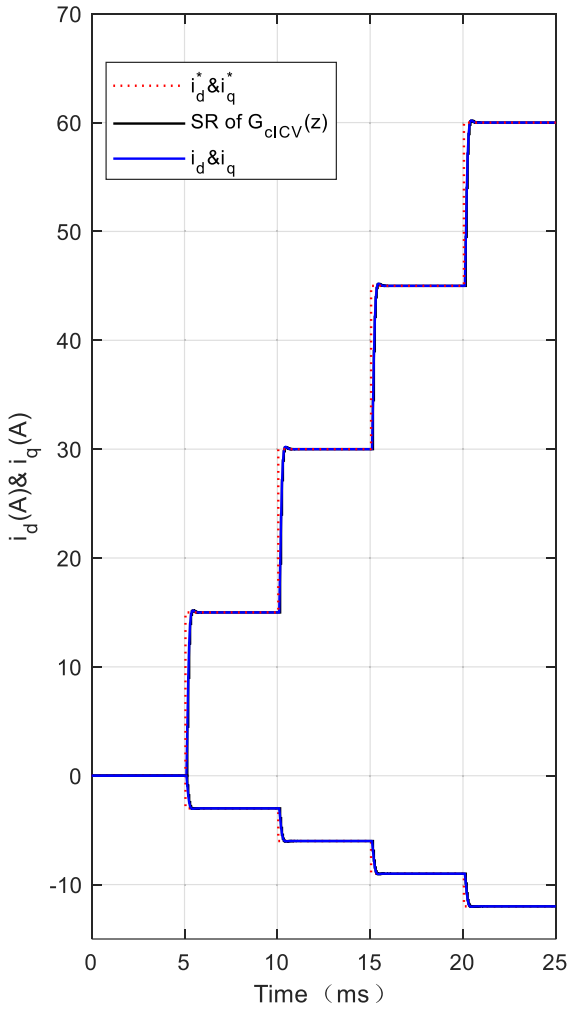


Figure 4.7 Simulation result of complex vector controller based on flux-linkage data ($k = 0.3$) of the locked saturated machine.

### 4.4.2 Simulation of the High-Speed Machine

In the high-speed mode, the speed is set as 5000 rpm, which means that the fundamental frequency of the output current $f_{out}$ is 833Hz. The current reference value is less than the rated value. In order to improve the ratio of current frequency to sampling frequency, SSSU is adopted. The sampling frequency $f_s$ is 10 kHz. The −3 dB bandwidth is set to $6473 rad/s$ through making $\alpha = 6473 rad/s, k = 0.3$.

Figures 4.8 and 4.9 present simulation results. The decoupled performance of the classical PI control system is unsatisfactory at high speed with rated current working conditions. This is because of the mismatch of inductance parameters and time delay. Furthermore, complex vector control, which is deducted from the accurate model, achieves perfect decoupling. The current trajectory follows the step response of the closed-loop transfer function $G_{clCV}(z)$ satisfactorily.

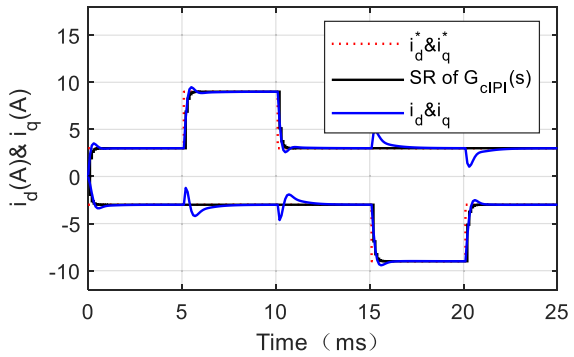


Figure 4.8 Simulation result of PI controller based on DIMC ($\alpha = 6473rad/s$, $f_s = 10kHz$) of the high-speed machine ($f_{out} = 833Hz$).

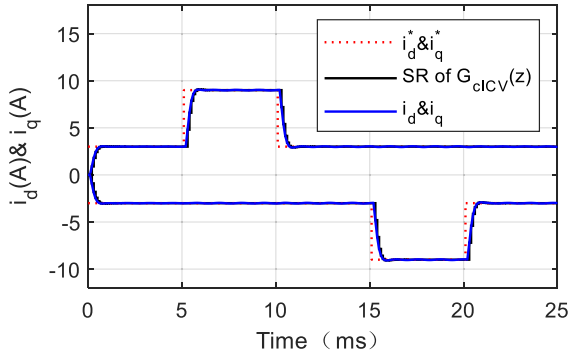


Figure 4.9 Simulation result of complex vector controller based on flux-linkage data ($k = 0.3$,$f_s = 10kHz$) of the high-speed machine ($f_{out} = 833Hz$).

### 4.4.3 Simulation of the High-Speed Saturated Machine

Now, set the speed to 5000 rpm and the sampling frequency to 10 kHz in the simulation. The parameters of both controllers are still the same, namely $\alpha = 6473rad/s$, $k = 0.3$. The quadrature axis current is given an incremental increase of 15 A each 5 ms from 0 to 60 A, while the direct axis current is given a step decrease of 3 A each 5 ms from 0 to −12 A.

The simulation results can be seen in Figures 4.10 and 4.11. For complex vector control, the current still agrees with the expected response and achieves good performance in the dynamic and steady state. In contrast, the classic PI control based on the DIMC principle fails to follow the instructions, especially in highly saturated situations. This is because the PI controller's parameters are fixed and cannot adapt to the changes in motor parameters caused by saturation.

The simulation results illustrate that the complex vector controller based on flux-linkage data is suitable for saturated and high-speed machines.

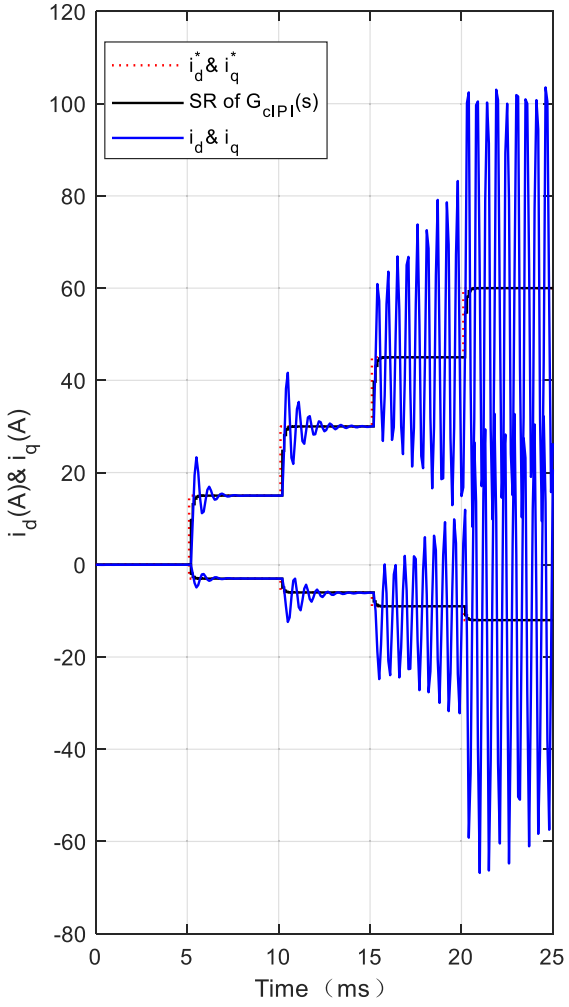


Figure 4.10 Simulation result of PI controller based on DIMC ($\alpha = 6473rad/s$, $f_s = 10kHz$) of the high-speed saturated machine ($f_{out} = 833Hz$).

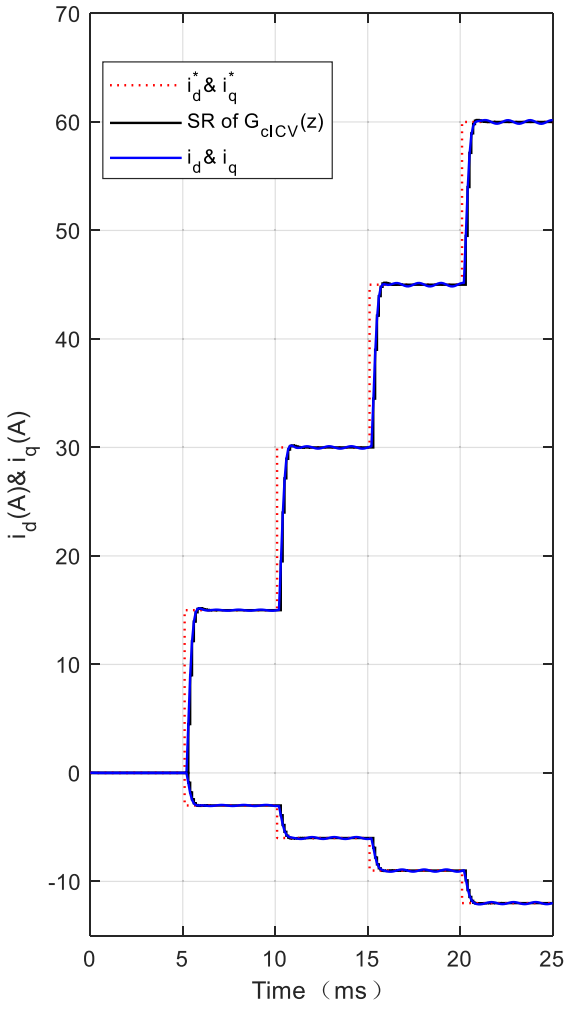


Figure 4.11 Simulation result of complex vector controller based on flux-linkage data ($k = 0.3, f_s = 10kHz$) of the high-speed machine ($f_{out} = 833Hz$).

## 4.5 EXPERIMENT RESULT

In this section, the experimental platform is introduced first. Then, the experiment results are presented.

### 4.5.1 Experiment Platform

Figure 4.12 presents the experiment platform. The motor under test (MUT) and load motor are installed on the bench. These two motors are powered by two VSIs. The data are sent to computers through USB-CAN interfaces. The data in DSP reflect the actual values of the current loop controller; thus, the digital values transported to the computer are used in the analysis of this study rather than the analog value measured by the current clamp [111]. The user interfaces on the computers can display data and send instructions. The magnetic particle brake is installed on the bench to lock the MUT when the parameters are measured, the inverter nonlinearity is measured, and the 0-speed current control performance experiment is carried out. Parameters of

the motor under test and load motor are shown in Table 4.1.

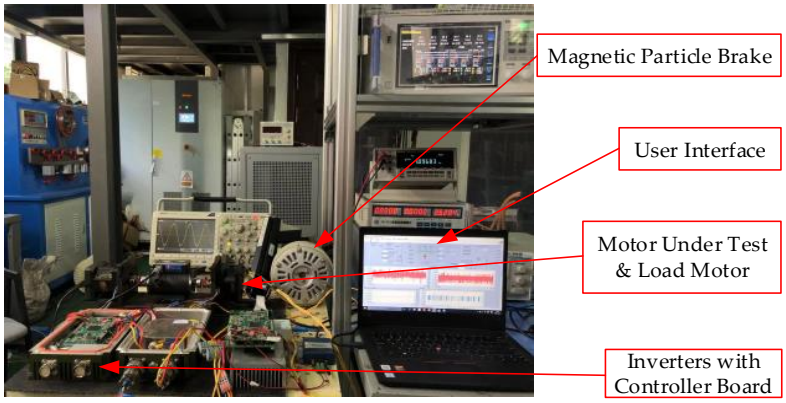


Figure 4.12 Experiment platform.

Table 4.1 Parameters of the motor under test and load motor.

| Parameters | Motor Under Test | Load Motor |
|---|---|---|
| Number of pole pairs | 10 | 10 |
| Stator winding resistance | 0.8 Ω | 1.5 Ω |
| d-axis inductance | 0.69 mH [1] | 0.63 mH [1] |
| q-axis inductance | 0.74 mH [1] | 0.67 mH [1] |
| PM flux-linkage | 0.02 Wb | 0.018 Wb |
| Rated speed | 2000 rpm | 2000 rpm |
| Maximum speed | 5000 rpm | 5000 rpm |

[1] The data are measured at $i_d = -1.8\text{A}$, $i_q = 9\text{A}$.

The TMS320F28335 of Texas Instruments is adopted in the full-bridge inverter, which is made of IGBTs. The switching frequency of the inverter is 10 kHz. By using SSSU/DSDU, the sampling frequency is 10 kHz/20 kHz. Direct memory access (DMA) technology is used to increase the current sample accuracy. The look-up tables for $\psi_d(i_d, i_q)$ and $\psi_q(i_d, i_q)$ are saved in a flash. At the beginning of the program, the table is moved to RAM. The sine and cosine values are also computed after reset to increase code execution speed. The deadtime compensation algorithm is adopted to improve the accuracy of output voltage [112]. Although the complex vector controller involves more computation due to delay compensation using trigonometric functions, the lookup operation itself is efficient. It runs in real-time on DSP28335 with CPU utilization below 85%.

The parameters used in the PI controller are static inductance at $i_d = -1.8\text{A}$, $i_q = 9\text{A}$. As for the complex vector controller, calculating $i_d$ and $i_q$, looking up to the table, and interpolation are implemented to get the value of $\psi_d(i_d, i_q)$ and $\psi_q(i_d, i_q)$. Instead of using current, flux linkage feedback can avoid the influence of the cross-saturation terms $l_{dq}(i_d, i_q) \cdot di_q/dt$ and $l_{qd}(i_d, i_q) \cdot di_d/dt$, which improves the performance of the current control.

The control software cannot show every sampling value in real time due to the capacity of the serial controller area network (CAN) bus communications. The sampled values are recorded in RAM every sampling period at running conditions. When the system stops, the recorded values are transmitted to the computer.

### 4.5.2 Experiment Result of the Locked Saturated Machine

Lock the rotor through a magnetic particle brake and set the control parameter/sampling frequency the

same as the simulation. The quadrature axis current is given with an incremental increase of 15 A from 0 to 60 A, 5 ms each. The direct axis current is given with a step decrease of 3 A from 0 to −12 A, 5 ms each.

The experiment results are consistent with the simulation results. For the classical PI controller, the current ringing effect becomes more and more distinct with the increasing current, as shown in Figure 4.13. At around 21ms, the software protection is triggered. The result represents that the dynamic and steady-state performance of the PI controller based on IMC is not guaranteed when the iron core is saturated. Although the current $i_d$ demagnetizes the magnetic circuit in this experiment, the cross saturation reduces the direct-axis inductance. Figure 4.14 will be discussed in Section 3.5.4 for coherence.

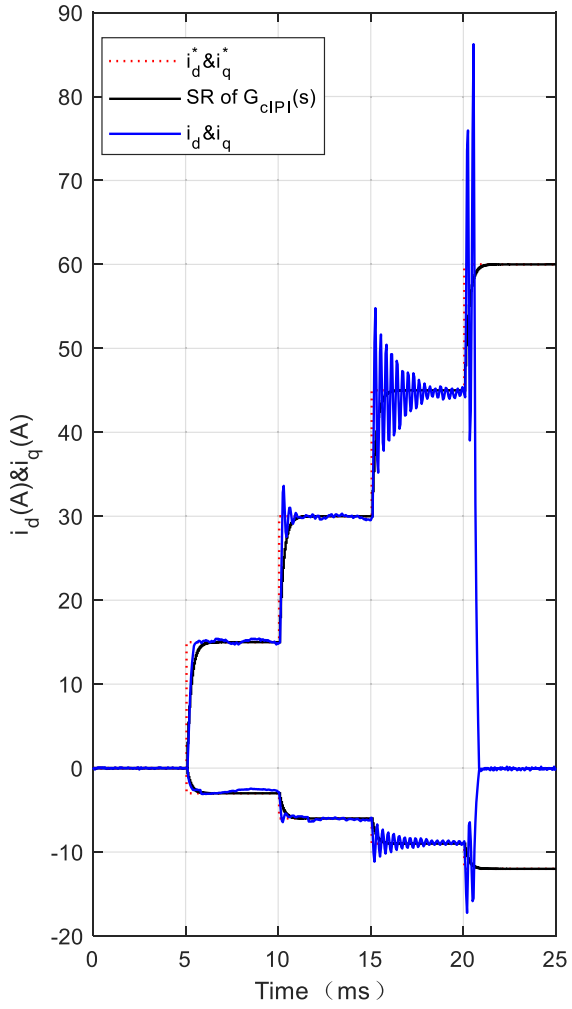


Figure 4.13 Experiment result of PI controller based on DIMC ($\alpha = 4000 rad/s$) of the locked saturated machine.

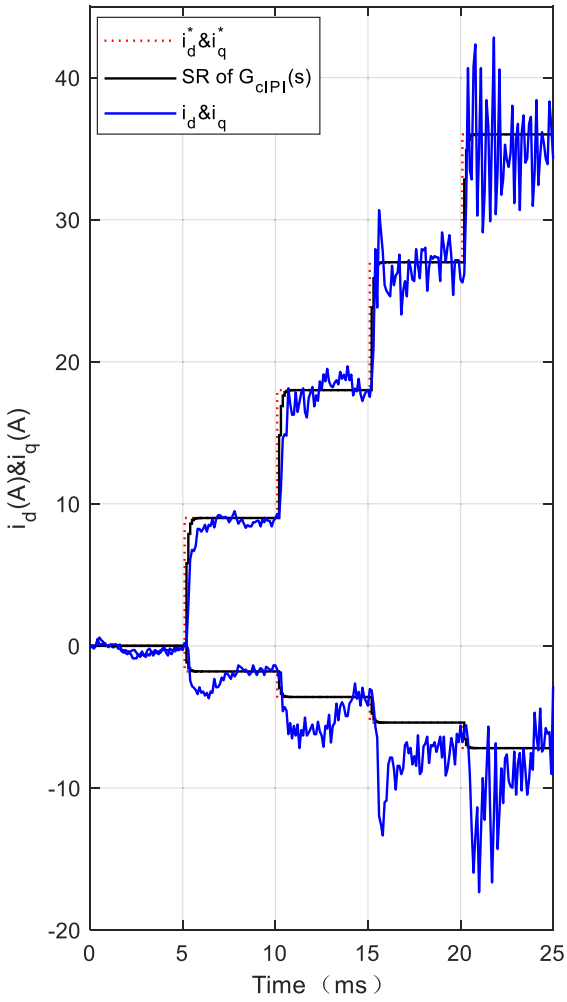


Figure 4.14 Experiment result of PI controller based on DIMC ($\alpha = 6473\text{rad/s}, f_s = 10kHz$) of the high-speed saturated machine ($f_{out} = 833Hz$).

Figure 4.15 presents the experiment result of complex vector control. The response of each step is presented separately to show the detailed results. The current response follows the step response of the closed-loop transfer function satisfactorily. The usage of flux-linkage data can compensate for the parameter mismatch of inductance.

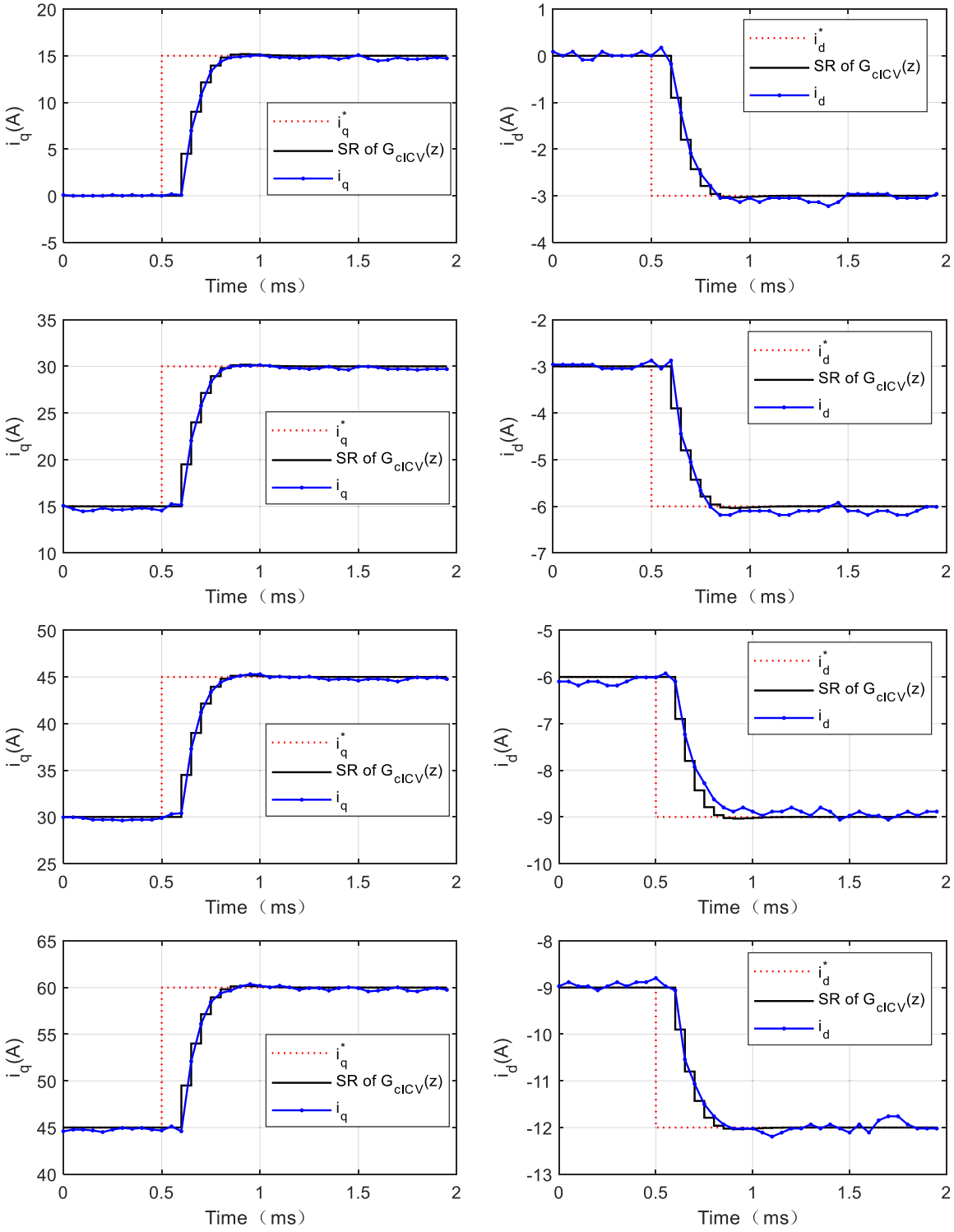


Figure 4.15 Experiment result of complex vector controller based on flux-linkage data ($k = 0.3$) of the locked saturated machine

### 4.5.3 Experiment Result of the High-Speed Machine

The load motor is used to control the speed at 5000 rpm. The dq axis of the motor is given with pulse reference currents in turn which are not greater than the rated current, and the step response and decoupling performance are observed. Controller parameters and sampling time are the same as the simulation values.

Figures 4.16-4.18 present the experiment results, consistent with the simulation results. The steady and dynamic performance of the complex vector controller is better than that of the classical PI controller at $f_{out} = 833Hz$. With the proposed controller, the current oscillation caused by the coupling effect decreases from 1.8 to 0.6 A. The almost perfect decoupling performance in high-speed working conditions is achieved by using the complex vector controller. By putting the d-q current into the X–Y plot, the fluctuation of complex vector controller steady current at (−3 A, 9 A), (−9 A, 3 A), (−3 A, 3 A) is gentler than that of the PI controller. At the time of 5.5, 10.5, 15.8, and 20.5 ms, it can be seen that the deviation between the current under PI control and the reference current is more significant than that under the complex vector controller.

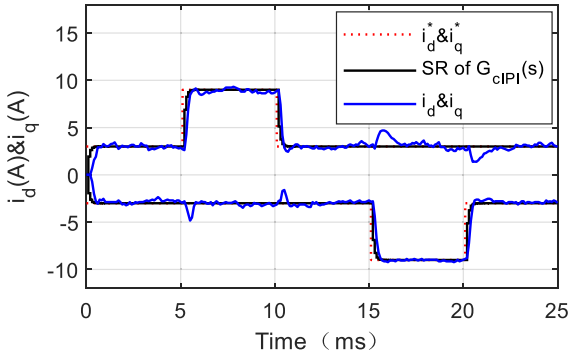


Figure 4.16 Experiment result of PI controller based on DIMC ($\alpha = 6473rad/s$, $f_s = 10kHz$) of the high-speed machine ($f_{out} = 833Hz$).

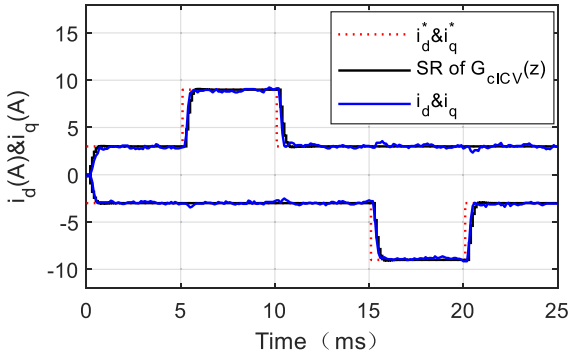


Figure 4.17 Experiment result of complex vector controller based on flux-linkage data ($k = 0.3$,$f_s = 10kHz$) of the high-speed machine ($f_{out} = 833Hz$).

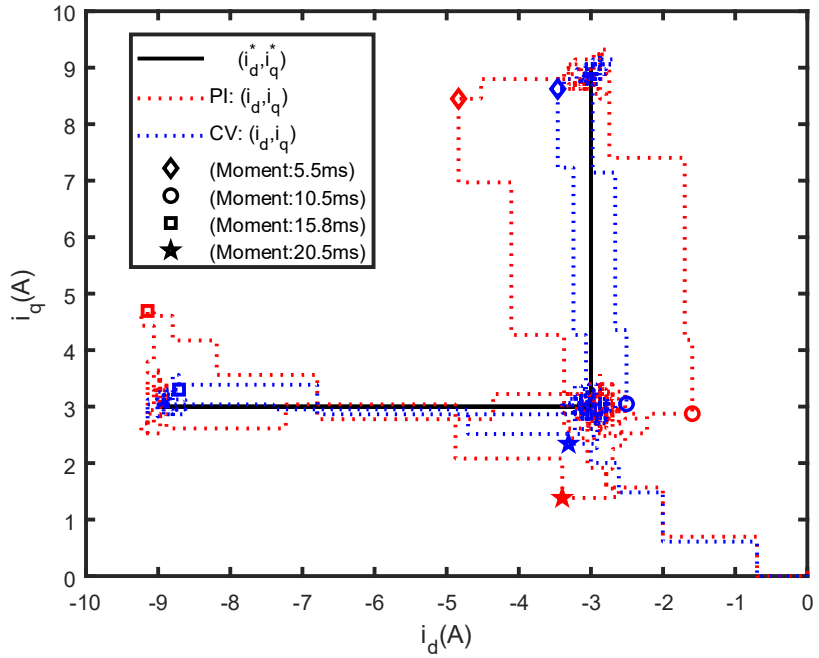


Figure 4.18 X-Y graph of the d-q current under PI controller based on DIMC ($\alpha = 6473 rad/s$, $f_s = 10kHz$) and complex vector controller based on flux-linkage data ($k = 0.3$,$f_s = 10kHz$) of the high-speed machine ($f_{out} = 833Hz$).

### 4.5.4 Experiment Result of the High-Speed Saturated Machine

The load motor is used to control the speed at 5000 rpm. Controller parameters and sampling time are the same as the simulation values. During the verification of the PI controller, the quadrature axis current is given with an incremental increase of 9 A from 0 to 36 A, 5 ms each, to prevent the current loop from collapsing. The quadrature axis current is given with an incremental increase of 15 A from 0 to 60 A, 5 ms each, which is the same as the simulation. Both reference values of the direct axis current are set as $i_d^* = -0.2 \cdot i_q^*$.

The experiment results of both controllers under saturated high-speed working conditions are presented in Figures 4.14 and 4.19. At high speeds, the control performance of the classical PI controller deteriorates with increasing saturation. The response of each step is shown separately to describe the detailed results. With the proposed controller, the peak quadrature axis current is improved from 36 to 60 A, and the peak direct axis current is improved from -7.2 to -12 A, which improves the output power by 39%. At the fundamental frequency of output current, which is 833 Hz, the current response follows the step response of the closed-loop transfer function satisfactorily. The increase in the current ripple is inevitable because of the decrease in the inductance.

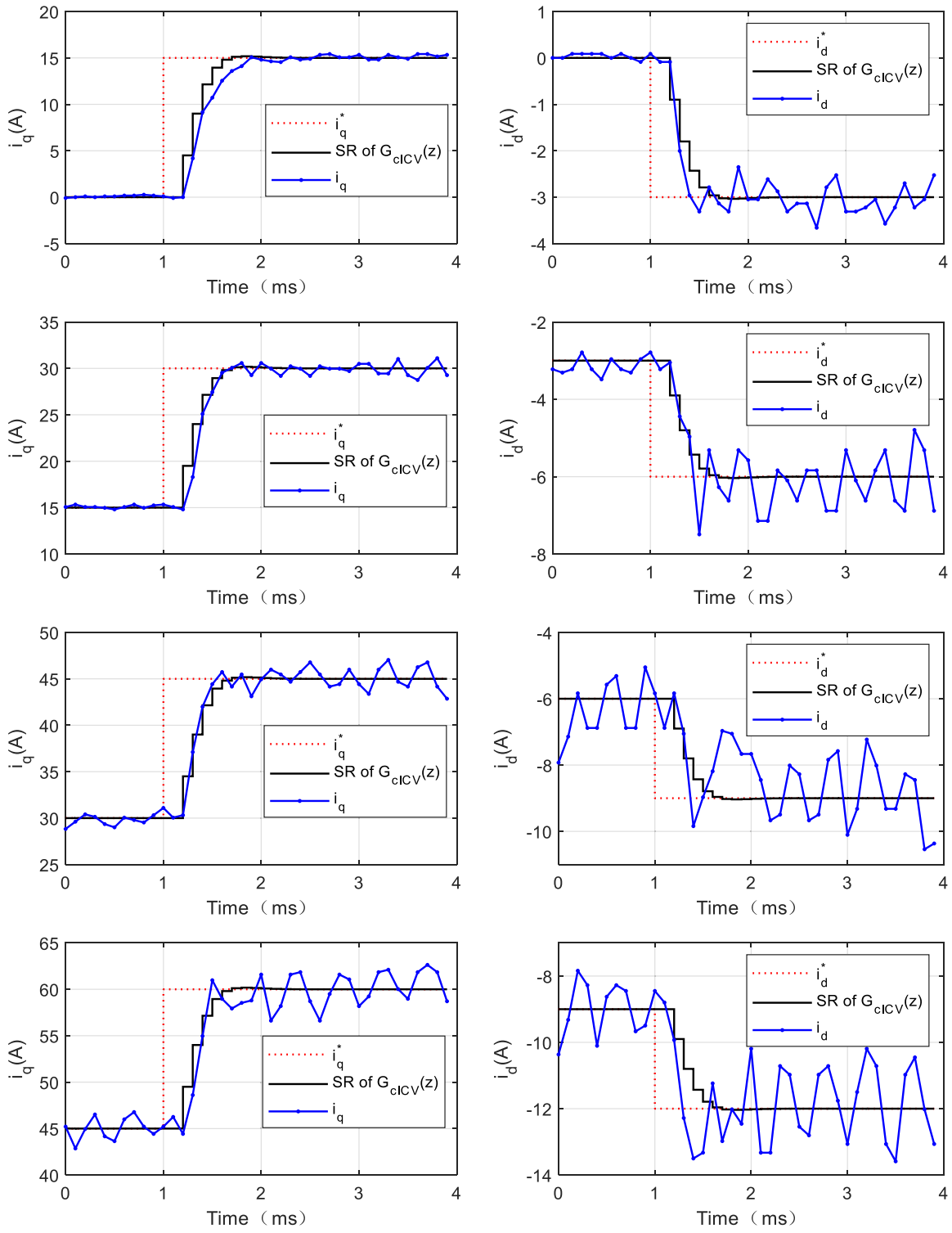


Figure 4.19 Experiment result of complex vector controller based on flux-linkage data ($k = 0.3, f_s = 10kHz$) of the high-speed saturated machine ($f_{out} = 833Hz$).

## 4.6 SUMMARY

In this chapter, the influence of time delay in the digital control system is analyzed. The flux-linkage values at different current conditions are measured. Then, a controller based on the flux data is proposed to mitigate the delay and parameter mismatch problems. To verify the performance, simulation and experiment of PI control based on the DIMC principle and complex vector control based on the flux-linkage data are carried out. As a comparative case, the performance of the PI controller based on DIMC matches the desired bandwidth target in unsaturated circumstances. The proposed controller achieves better bandwidth and decoupled performance than the DIMC PI controller. It can improve the peak current output region at high speed, which can improve the maximum output power by 39%. However, the parameters are prone to be affected by temperature, which is not included in this research. The nonlinearity caused by temperature will be investigated in future work.

# Chapter 5: Hybrid Spread Spectrum PWM Considering Saturation

In order to meet the requirements of performance, comfort, and safety, intelligent power electronic devices typically incorporate a significant number of integrated circuits, resulting in higher electrical integration. These devices often adopt a distributed drive system to achieve greater control freedom. Furthermore, factors such as stacked design, dense layout and routing, reduced volume of electromagnetic interference filters and shielding further increase the sensitivity of the system. These factors pose challenges to the existing electromagnetic compatibility design of power electronic devices.

This chapter introduces a hybrid modulation method for variable switching frequency control to harness the emission from the source. An offline table based on the average RMS value of flux linkage harmonics is utilized. This method avoids increasing the number of switching operations and switching losses, while maintaining the harmonic RMS value unchanged, which will prevent the increase of motor iron losses. Additionally, it reduces the peak value of the common-mode current by spreading the spectrum.

## 5.1 HYBRID SPREAD SPECTRUM PWM

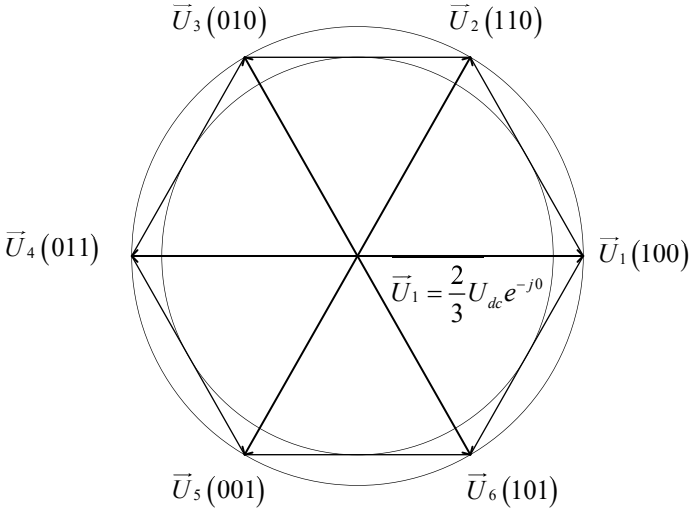


Figure 5.1 Fundamental vectors in the linear hexagon region.

Several basic voltage vector pulses are utilized in PWM technique to generate the target voltage vector. A three-phase two-level VSI outputs six active vectors, $\vec{U}_N$ $(N = 1,2,3,4,5,6)$, and two zero vectors, namely $\vec{U}_0$ and $\vec{U}_7$, as shown in Figure 5.1. The active vector $\vec{U}_N$ has a magnitude of $2U_{\mathrm{dc}}/3$, and by combining eight voltage vectors, any voltage vector within the hexagon can be synthesized. A binary logic switching functions $S_k$ $(k = a, b, c)$ is defined to represent the working conditions of the three legs of the VSI as

$$S_k = \begin{cases} 1 & \text{The upper leg is turned on while the lower leg is turned off} \\ 0 & \text{The upper leg is turned off while the lower leg is turned on} \end{cases} \quad (5.1)$$

The three bridge legs can be arranged in $2^3$ working states, corresponding to eight space vectors. The midpoints of the three bridge legs are connected to the $abc$ winding terminal of the motor. If the three-phase windings are assumed to be symmetrical, the maximum phase voltage on each winding is $2U_{dc}/3$. The pulse width modulation voltage applied to the three-phase winding, $\vec{U}_{PWM}$, is determined by the switching state, $S_k$, and can be written in the form of space vectors as follows:

$$\vec{U}_{PWM} = \frac{2}{3}S_a U_{dc} + \frac{2}{3}S_b U_{dc} e^{j\frac{2\pi}{3}} + \frac{2}{3}S_c U_{dc} e^{-j\frac{2\pi}{3}} \quad (5.2)$$

### 5.1.1 Analysis of flux linkage ripple in a subcycle of SVPWM and DPWM

A few voltage vector pulses are utilized in PWM techniques to generate the desired voltage vector. Among the PWM methods, SVPWM and DPWM are two commonly used ones due to the advantages of low harmonics, low switch losses, and high utilization of the DC bus. DPWM can be divided into DPWM012 and DPWM127 according to the allocation of the zero vector. Within one switching period, these three methods use two active vectors and one or two zero vectors to synthesize the reference vector. However, the error between these instantaneously applied output vectors and the reference vector will lead to ripples in the stator flux linkage and current. The error vectors are represented by $\vec{u}_{err,1}$, $\vec{u}_{err,2}$, $\vec{u}_{err,z}$ as shown in (5.3)

$$\begin{aligned} \vec{u}_{err,1} &= \frac{2}{3}U_{dc}e^{j0} - \overrightarrow{u^*} \\ \vec{u}_{err,2} &= \frac{2}{3}U_{dc}e^{j\frac{\pi}{3}} - \overrightarrow{u^*} \\ \vec{u}_{err,z} &= 0 - \overrightarrow{u^*} \end{aligned} \quad (5.3)$$

Voltage harmonics are space vectors that can be decomposed and calculated in the three-phase stationary $abc$ coordinate system, the two-phase stationary $\alpha\beta$ coordinate system, and the voltage-oriented synchronous rotating $DQ$ coordinate system [113]. To simplify the calculation, this research uses the $DQ$ coordinate system. As shown in Figure 5.2, the $DQ$ coordinate system is rotating synchronously with a reference voltage vector, of which the $Q$-axis aligned with the direction of the given voltage, and the $D$-axis lags 90 degrees behind the $Q$-axis in electrical angle. In steady states, the angular velocity of the given voltage is the same as the motor's electrical angular speed, and the $DQ$ coordinate system can be viewed as a synchronous rotating coordinate system.

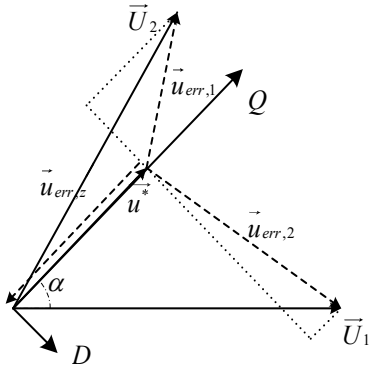


Figure 5.2 Decomposition of error vectors $\vec{u}_{err,1}$, $\vec{u}_{err,2}$, $\vec{u}_{err,z}$ in the $DQ$ coordinate system.

The modulation method studied in this research uses symmetrical vectors on both sides of the switch midpoint. In order to simplify the analysis, only the ripple within one sub-fundamental cycle $T_{ss} = T_s/2$ is calculated. The flux linkage ripple $\overrightarrow{\Delta\psi^{DQ}}(t)$ is a vector that can be decomposed into $D$-axis and $Q$-axis flux linkage ripples $\Delta\psi^D(t)$ and $\Delta\psi^Q(t)$ in the $DQ$ coordinate system, as shown in (5.4):

$$\overrightarrow{\Delta\psi^{DQ}}(t) = \Delta\psi^D(t) + j\Delta\psi^Q(t) \tag{5.4}$$

The flux linkage ripple varies with the sector periodically. Taking the reference voltage $u^*$ in the first sector as an example, when SVPWM modulation is used for output, the flux linkage ripple on the $DQ$ axis is denoted by $\Delta\psi^D_{0127}(t)$ and $\Delta\psi^Q_{0127}(t)$, both of which are functions of time. Depending on the selected fundamental vectors, they can be expressed by piecewise functions, as shown in (5.5) and (5.6):

$$\Delta\psi^Q_{0127}(t) = \begin{cases} -u^*t, & 0 \le t < 0.5T_z \\ \left(\frac{2}{3}U_{dc}cos(\alpha) - u^*\right)(t - 0.5T_z) + \Delta\psi^Q_{0127}(0.5T_z), & 0.5T_z \le t < 0.5T_z + T_1 \\ \left(\frac{2}{3}U_{dc}cos\left(\frac{\pi}{3} - \alpha\right) - u^*\right)(t - 0.5T_z - T_1) + \Delta\psi^Q_{0127}(0.5T_z + T_1), & 0.5T_z + T_1 \le t < 0.5T_z + T_1 + T_2 \\ -u^*(t - 0.5T_z - T_1) + \Delta\psi^Q_{0127}(0.5T_z + T_1 + T_2), & 0.5T_z + T_1 + T_2 \le t < T_{ss} \end{cases} \tag{5.5}$$

$$\Delta\psi^D_{0127}(t) = \begin{cases} 0, & 0 \le t < 0.5T_z \\ \frac{2}{3}U_{dc}sin(\alpha)(t - 0.5T_z), & 0.5T_z \le t < 0.5T_z + T_1 \\ \frac{2}{3}U_{dc}sin\left(\frac{\pi}{3} - \alpha\right)(t - 0.5T_z - T_1) + \Delta\psi^D_{0127}(0.5T_z + T_1), & 0.5T_z + T_1 \le t < 0.5T_z + T_1 + T_2 \\ 0, & 0.5T_z + T_1 + T_2 \le t < T_{ss} \end{cases} \tag{5.6}$$

The flux linkage ripple decomposition of SVPWM, DPWM012 and DPWM721 in the $DQ$ coordinate system is shown in the figure below. The figure shows the fluctuation of flux linkage caused by each sub-fundamental voltage vector.

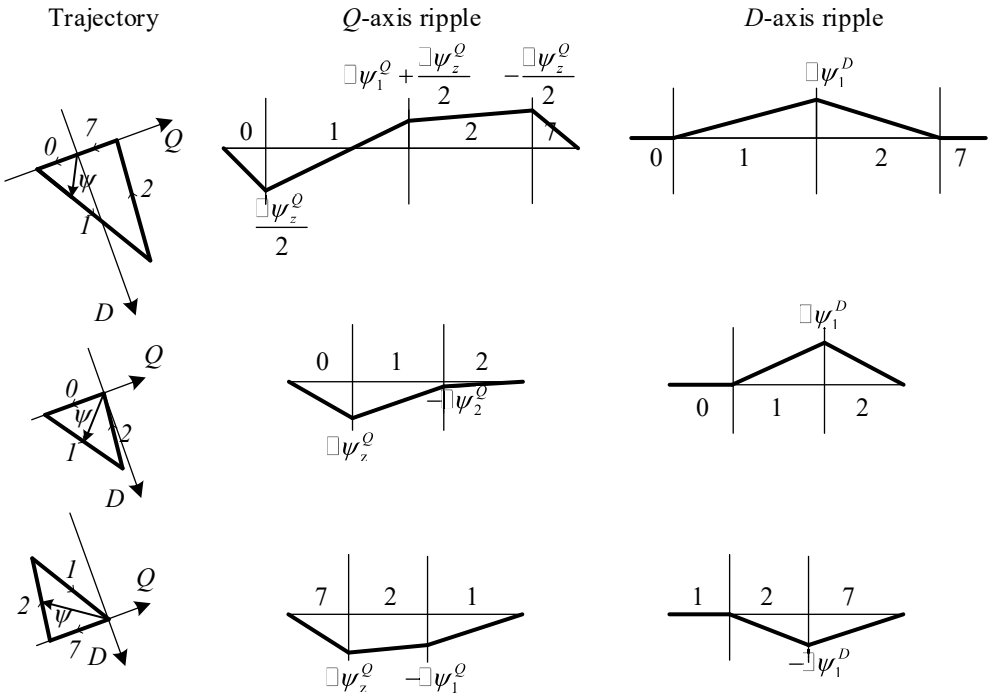


Figure 5.3 The flux linkage ripple decomposition of SVPWM, DPWM012 and DPWM721 in the given voltage-oriented coordinate system.

The PWM voltage vectors cause fluctuations in flux linkage. Let $\Delta\psi_1^Q$， $\Delta\psi_2^Q$ and $\Delta\psi_z^Q$ represent the components of flux linkage ripple in the $Q$-axis caused by the 1, 2, and zero vectors, respectively, where z represents the 0 vector or the 7 vector. $\Delta\psi_1^D$ and $\Delta\psi_2^D$ represent the $D$-axis components of the flux linkage ripple caused by the 1 and 2 vectors, respectively. $T_1$， $T_2$ and $T_z$ are the times of the 1, 2, and zero vectors during a sub-fundamental cycle $T_{ss}$, respectively, and $sqrt\{\cdot\}$ represents the square root function.

$$\begin{cases} \Delta\psi_1^Q = \left[\dfrac{2}{3}U_{dc}cos(\alpha) - u^*\right]T_1 \\ \Delta\psi_2^Q = \left[\dfrac{2}{3}U_{dc}cos\left(\dfrac{\pi}{3}-\alpha\right) - u^*\right]T_2 \\ \Delta\psi_z^Q = -u^*T_z \\ \Delta\psi_1^D = \dfrac{2}{3}U_{dc}sin(\alpha)T_1 \\ \Delta\psi_2^D = \dfrac{2}{3}U_{dc}sin\left(\dfrac{\pi}{3}-\alpha\right)T_2 \\ \Delta\psi_z^D = 0 \end{cases} \tag{5.7}$$

For SVPWM, the root-mean-square (RMS) value of the flux linkage ripple $\Delta\psi_{0127}^{rms}$ within a sub-fundamental cycle $T_{ss}$ can be obtained by integrating the $D$ and $Q$-axis flux linkage ripple over one sub-fundamental cycle and is given by the following equation:

$$\Delta\psi_{0127}^{rms}=\sqrt{\frac{1}{T_{ss}}\int_0^{T_{ss}}[\Delta\psi_{0127}^{D}(t)]^2+[\Delta\psi_{0127}^{Q}(t)]^2dt}$$

$$\begin{aligned}&=sqrt\Big\{\frac{1}{3}\left(0.5\Delta\psi_z^Q\right)^2\frac{T_z}{2T_{ss}}\\&+\frac{1}{3}\Big[\left(0.5\Delta\psi_z^Q\right)^2+0.5\Delta\psi_z^Q\left(0.5\Delta\psi_z^Q+\Delta\psi_1^Q\right)+\left(0.5\Delta\psi_z^Q+\Delta\psi_1^Q\right)^2\Big]\frac{T_1}{T_{ss}}\\&+\frac{1}{3}\Big[\left(0.5\Delta\psi_z^Q+\Delta\psi_1^Q\right)^2-0.5\Delta\psi_z^Q\left(0.5\Delta\psi_z^Q+\Delta\psi_1^Q\right)+\left(-0.5\Delta\psi_z^Q\right)^2\Big]\frac{T_2}{T_{ss}}\\&+\frac{1}{3}\left(-0.5\Delta\psi_z^Q\right)^2\frac{T_z}{2T_{ss}}+\frac{1}{3}\left(\Delta\psi_1^D\right)^2\frac{T_1+T_2}{T_{ss}}\Big\}\end{aligned}\tag{5.8}$$

For SVPWM, DPWM012, and DPWM721, the sub-switching period $T_{ss}$ is given by:

$$T_1+T_2+T_z=T_{ss}\tag{5.9}$$

Similarly, the RMS value of the flux linkage ripple of DPWM012 and DPWM721 can be obtained as:

$$\Delta\psi_{012}^{rms}=\sqrt{\frac{1}{T_{ss}}\int_0^{T_{ss}}[\Delta\psi_{012}^{D}(t)]^2+[\Delta\psi_{012}^{Q}(t)]^2dt}$$

$$\begin{aligned}&=sqrt\Big\{\frac{1}{3}\left(\Delta\psi_z^Q\right)^2\frac{T_z}{T_{ss}}+\frac{1}{3}\Big[\left(\Delta\psi_z^Q\right)^2+\Delta\psi_z^Q\left(\Delta\psi_z^Q+\Delta\psi_1^Q\right)+\left(\Delta\psi_z^Q+\Delta\psi_1^Q\right)^2\Big]\frac{T_1}{T_{ss}}\\&+\frac{1}{3}\left(\Delta\psi_z^Q+\Delta\psi_1^Q\right)^2\frac{T_2}{T_{ss}}+\frac{1}{3}\left(\Delta\psi_1^D\right)^2\frac{T_1+T_2}{T_{ss}}\Big\}\end{aligned}\tag{5.10}$$

$$\Delta\psi_{721}^{rms}=\sqrt{\frac{1}{T_{ss}}\int_0^{T_{ss}}[\Delta\psi_{721}^{D}(t)]^2+[\Delta\psi_{721}^{Q}(t)]^2dt}$$

$$\begin{aligned}&=sqrt\Big\{\frac{1}{3}\left(\Delta\psi_z^Q\right)^2\frac{T_z}{T_{ss}}+\frac{1}{3}\Big[\left(\Delta\psi_z^Q\right)^2+\Delta\psi_z^Q\left(\Delta\psi_z^Q+\Delta\psi_1^Q\right)+\left(\Delta\psi_z^Q+\Delta\psi_1^Q\right)^2\Big]\frac{T_2}{T_{ss}}\\&+\frac{1}{3}\left(\Delta\psi_z^Q+\Delta\psi_1^Q\right)^2\frac{T_1}{T_{ss}}+\frac{1}{3}\left(\Delta\psi_1^D\right)^2\frac{T_1+T_2}{T_{ss}}\Big\}\end{aligned}\tag{5.11}$$

Based on (5.9)-(5.11), it can be seen that the RMS flux linkage ripple value is proportional to the DC bus voltage. Meanwhile, according to (5.7), the RMS value of the flux linkage ripple varies continuously with the amplitude of the command voltage vector $u^*$, the angle of the command voltage vector $\alpha$ and the sub-fundamental cycle $T_{ss}$. By changing the switching frequency, the harmonic fluctuations caused by $u^*$ and $\alpha$ can be mitigated, which will be further discussed in Section 5.1.3.

The RMS value of the flux linkage ripple $\Delta\psi^{rms}(u^*,\ \alpha,\ U_{dc},\ T_{ss})$ is proportional to the amplitude of the DC bus voltage $U_{dc}$. For the convenience of comparison, the modulation factor $M_i$ is defined in (5.12). When

$M_i \in [0, \sqrt{3}/2]$, the inverter works in the sine linear modulation region. When $M_i = \sqrt{3}/2$, the amplitude of the given voltage vector $\overrightarrow{u^*}$ is equal to the radius of the inscribed circle of the regular hexagon in Figure 5.1.

$$M_i = \frac{3}{2U_{dc}} u^* \tag{5.12}$$

The RMS value of flux linkage ripple $\Delta\psi^{rms}$ is also related to the voltage vector amplitude $u^*$, angle $\alpha$, and the sub-fundamental cycle $T_{ss}$. To make the calculation applicable to arbitrary basic switching frequency and DC bus voltage, the flux linkage ripple is normalized. The specific normalization method can be found in Appendix A. After normalization, the normalized RMS value of the flux linkage ripple $\Delta\psi_{pu}^{rms}(M_i,\ \alpha)$ is only related to the modulation coefficient $M_i$ and the angle $\alpha$ of the given voltage vector.

In order to compare the three modulation methods, the normalized flux linkage ripple values $\Delta\psi_{0127pu}^{rms}(M_i,\ \alpha)$, $\Delta\psi_{127pu}^{rms}(M_i,\ \alpha)$, $\Delta\psi_{012pu}^{rms}(M_i,\ \alpha)$ are plotted against $(M_i,\ \alpha)$ in Figure 5.4. When the modulation index $M_i$ is high, both DPWM methods exhibit lower flux linkage ripple compared to SVPWM. Therefore, a combination of the three modulation methods can be used to reduce the flux linkage ripple while maintaining equivalent switching losses.

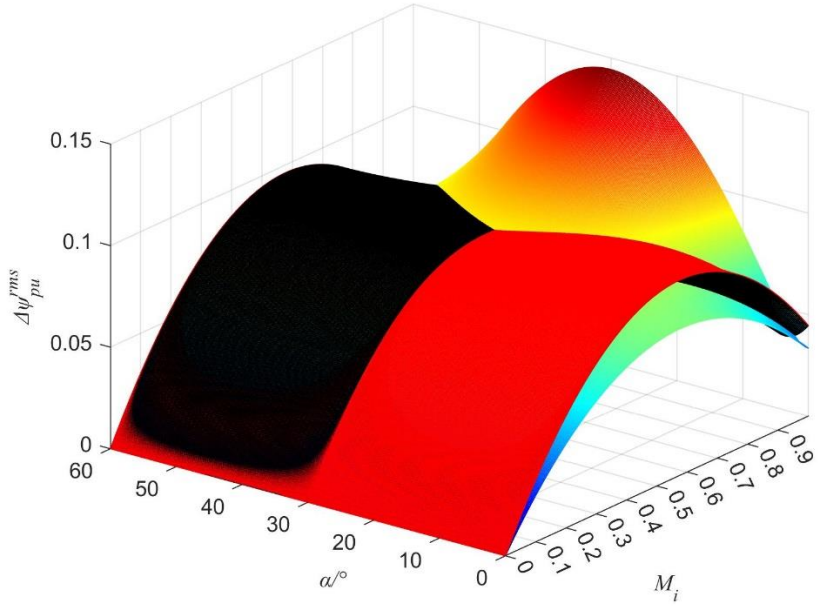


Figure 5.4 Normalized flux linkage ripple values of SVPWM (colored), DPWM012 (black), DPWM721 (red).

### 5.1.2 Analysis of Flux Linkage Ripple of AZSPWM and NSPWM in a Subcycle

The use of zero vectors may cause a common mode voltage fluctuation with an amplitude of $\pm U_{dc}/2$. Active zero vector pulse width modulation and near state pulse width modulation are two methods that can reduce the common mode voltage fluctuation caused by the use of zero vectors. This fluctuation can be reduced

to $\pm U_{dc}/6$ through the use of AZSPWM or NSPWM. Moreover, by avoiding the use of zero vectors, the energy emitted by EMI from the source can also be reduced. Specifically, AZSPWM replaces the zero vector with two opposite active vectors, while NSPWM outputs the reference vector equivalently using three adjacent active vectors, as shown in the figure below.

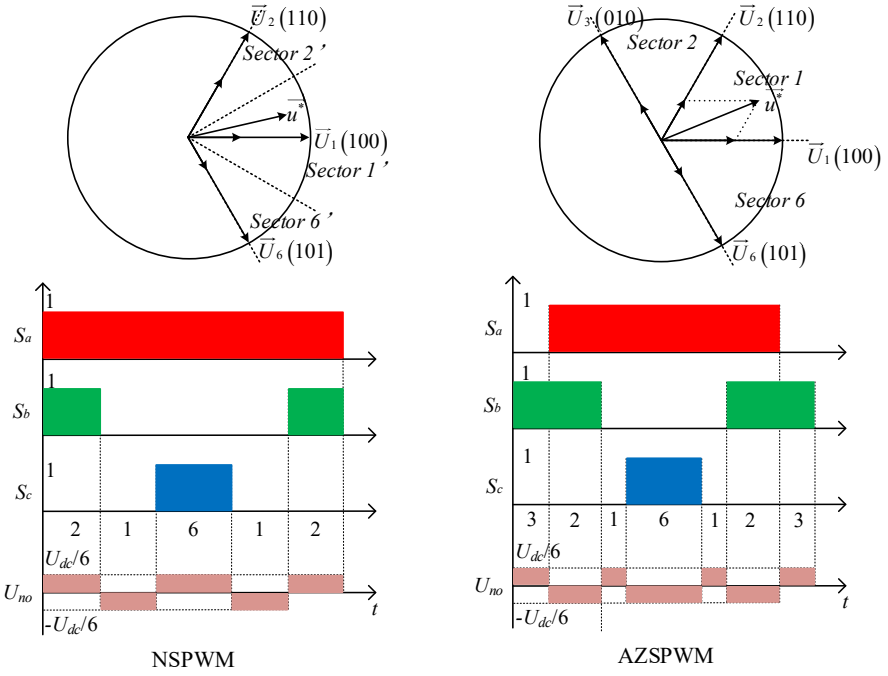


Figure 5.5 Schematic diagram of switch sequence and CM voltage for output of the first sector vector using AZSPWM and NSPWM.

Taking voltage vectors in sector 1 of AZSPWM and vectors in sector $1'$ of NSPWM as examples, the trajectory of the flux linkage error vectors in the $DQ$ coordinate system is shown in Figure 5.6.

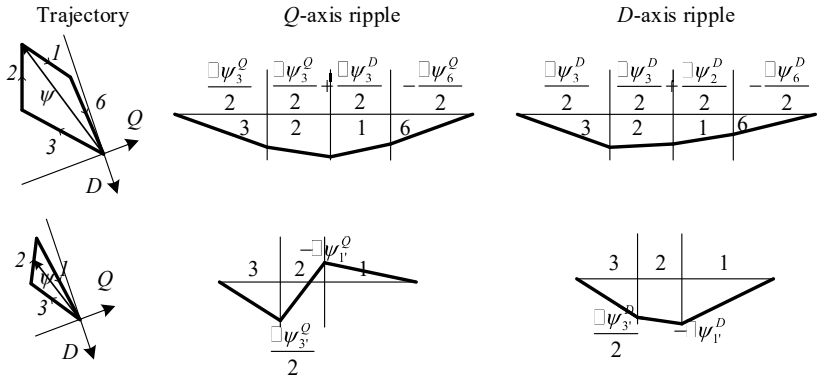


Figure 5.6 The flux linkage ripple decomposition of AZSPWM and NSPWM in the $DQ$ coordinate system.

When using AZSPWM, the given vector $\overrightarrow{u^*}$ in the sector 1 needs two active vectors, 3 and 6, to achieve the function of the zero vector, so we have:

$$T_1 + T_2 + T_3 + T_6 = T_{ss} \tag{5.13}$$

When using AZSPWM, the RMS value of the flux linkage ripple $\Delta\psi_{3216}^{rms}$ within $T_{ss}$ can be expressed as follows:

$$\begin{aligned}\Delta\psi_{3216}^{rms} &= \sqrt{\frac{1}{T_{ss}}\int_0^{T_{ss}}[\Delta\psi_{3216}^{D}(t)]^2+[\Delta\psi_{3216}^{Q}(t)]^2dt}\\ &= sqrt\left\{\frac{1}{3}\left(\Delta\psi_3^Q\right)^2\frac{T_3}{T_{ss}}+\frac{1}{3}\left[\left(\Delta\psi_3^Q\right)^2+\Delta\psi_3^Q\left(\Delta\psi_3^Q+\Delta\psi_2^Q\right)+\left(\Delta\psi_3^Q+\Delta\psi_2^Q\right)^2\right]\frac{T_2}{T_{ss}}\right.\\ &+\frac{1}{3}\left[\left(\Delta\psi_3^Q+\Delta\psi_2^Q\right)^2-\Delta\psi_6^Q\left(\Delta\psi_3^Q+\Delta\psi_2^Q\right)+\left(\Delta\psi_6^Q\right)^2\right]\frac{T_1}{T_{ss}}+\frac{1}{3}\left(\Delta\psi_6^Q\right)^2\frac{T_6}{T_{ss}}+\frac{1}{3}\left(\Delta\psi_3^D\right)^2\frac{T_3}{T_{ss}}\\ &+\frac{1}{3}\left[\left(\Delta\psi_3^D\right)^2+\Delta\psi_3^D\left(\Delta\psi_3^D+\Delta\psi_2^D\right)+\left(\Delta\psi_3^D+\Delta\psi_2^D\right)^2\right]\frac{T_2}{T_{ss}}\\ &\left.+\frac{1}{3}\left[\left(\Delta\psi_3^D+\Delta\psi_2^D\right)^2-\Delta\psi_6^D\left(\Delta\psi_3^D+\Delta\psi_2^D\right)+\left(\Delta\psi_6^D\right)^2\right]\frac{T_1}{T_{ss}}+\frac{1}{3}\left(\Delta\psi_6^D\right)^2\frac{T_6}{T_{ss}}\right\}\end{aligned} \tag{5.14}$$

The intermediate variables $\Delta\psi_1^Q$, $\Delta\psi_2^Q$ and $\Delta\psi_1^D$, $\Delta\psi_2^D$ in (5.7) still apply. The $D$-axis and $Q$-axis components of the flux linkage ripples caused by the vectors 3 and 6 are recorded as $\Delta\psi_3^D$, $\Delta\psi_6^D$ and $\Delta\psi_3^Q$, $\Delta\psi_6^Q$, respectively, as shown below:

$$\begin{cases}\Delta\psi_3^D=\dfrac{2}{3}U_{dc}sin\left(\dfrac{2\pi}{3}-\alpha\right)T_3\\ \Delta\psi_6^D=\dfrac{2}{3}U_{dc}sin\left(\dfrac{5\pi}{3}-\alpha\right)T_6\\ \Delta\psi_3^Q=\left[\dfrac{2}{3}U_{dc}cos\left(\dfrac{2\pi}{3}-\alpha\right)-u^*\right]T_3\\ \Delta\psi_6^Q=\left[\dfrac{2}{3}U_{dc}cos\left(\dfrac{5\pi}{3}-\alpha\right)-u^*\right]T_6\end{cases} \tag{5.15}$$

NSPWM uses three adjacent active vectors to construct the command vector. The sector boundaries of NSPWM are different from other modulation methods mentioned previously. The sectors can be categorized by the angle $\alpha$ between the given vector $\overrightarrow{u^*}$ and the $\alpha$-axis. The sector boundaries of NSPWM occur at $\alpha=-\frac{\pi}{6}+N\frac{\pi}{3}, N=(1,2,3,4,5,6)$. The sectors of SVPWM, DPWM, and AZSPWM are labeled as $N$, while the sectors of NSWPM are labeled as $N'$. The distinction is shown in the table below.

Table 5.1 Sector division of SVPWM, DPWM, AZSPWM, and NSPWM.

| Sector for SVPWM,DPWM,AZSPWM | $\alpha$ for SVPWM,DPWM,AZSPWM | Sector for NSPWM | $\alpha$ for NSPWM |
|---|---|---|---|
| 1 | $0-\frac{\pi}{3}$ | $1'$ | $\left(-\frac{\pi}{6}\right)-\frac{\pi}{6}$ |
| 2 | $\frac{\pi}{3}-\frac{2\pi}{3}$ | $2'$ | $\frac{\pi}{6}-\frac{\pi}{2}$ |
| 3 | $\frac{2\pi}{3}-\pi$ | $3'$ | $\frac{\pi}{2}-\frac{5\pi}{6}$ |
| 4 | $\pi-\frac{4\pi}{3}$ | $4'$ | $\frac{5\pi}{6}-\frac{7\pi}{6}$ |
| 5 | $\frac{4\pi}{3}-\frac{5\pi}{3}$ | $5'$ | $\frac{7\pi}{6}-\frac{3\pi}{2}$ |

| | | | |
|---|---|---|---|
| 6 | $\frac{5\pi}{3}-2\pi$ | $6'$ | $\frac{3\pi}{2}-\left(-\frac{\pi}{6}\right)$ |

For the NSPWM method, to synthesize the target vector $\overrightarrow{u^*}$ in sector $1'$, three active vectors 1, 2, and 3 are needed, and we have:

$$T_1 + T_2 + T_3 = T_{ss} \tag{5.16}$$

The RMS value of the flux linkage ripple $\Delta\psi_{321}^{rms}$ for the NSPWM within a sub-fundamental $T_{ss}$ is given by the following equation:

$$\begin{aligned}\Delta\psi_{321}^{rms} &= \sqrt{\frac{1}{T_{ss}}\int_0^{T_{ss}}\left[\Delta\psi_{321}^{D}(t)\right]^2+\left[\Delta\psi_{321}^{Q}(t)\right]^2 dt} \\ &= sqrt\left\{\frac{1}{3}\left(\Delta\psi_{3'}^{Q}\right)^2\frac{T_3}{T_{ss}}+\frac{1}{3}\left[\left(\Delta\psi_{3'}^{Q}\right)^2+\Delta\psi_{3'}^{Q}\left(\Delta\psi_{3'}^{Q}+\Delta\psi_{2'}^{Q}\right)+\left(\Delta\psi_{3'}^{Q}+\Delta\psi_{2'}^{Q}\right)^2\right]\frac{T_2}{T_{ss}}\right. \\ &+\frac{1}{3}\left(\Delta\psi_{3'}^{Q}+\Delta\psi_{2'}^{Q}\right)^2\frac{T_1}{T_{ss}}+\frac{1}{3}\left(\Delta\psi_{3'}^{D}\right)^2\frac{T_3}{T_{ss}} \\ &+\frac{1}{3}\left[\left(\Delta\psi_{3'}^{D}\right)^2+\Delta\psi_{3'}^{D}\left(\Delta\psi_{3'}^{D}+\Delta\psi_{2'}^{D}\right)+\left(\Delta\psi_{3'}^{D}+\Delta\psi_{2'}^{D}\right)^2\right]\frac{T_2}{T_{ss}} \\ &\left.+\frac{1}{3}\left(\Delta\psi_{3'}^{D}+\Delta\psi_{2'}^{D}\right)^2\frac{T_1}{T_{ss}}\right\}\end{aligned} \tag{5.17}$$

The different definition of sectors does not result in the difference of the voltage vectors and angle $\alpha$ definitions. Therefore, the method for calculating the flux linkage ripple is the same as other modulation methods, namely:

$$\begin{cases}\Delta\psi_{N'}^{D}=\Delta\psi_{N}^{D}\\ \Delta\psi_{N'}^{Q}=\Delta\psi_{N}^{Q}\end{cases}\quad,\ N\in\{1,\ 2,\ 3,\ 4,\ 5,\ 6,\ z\} \tag{5.18}$$

AZSPWM and NSWPM do not adopt zero vectors. Figure 5.7 shows the relationship of $\Delta\psi_{3216pu}^{rms}(M_i,\ \alpha)$ and $\Delta\psi_{321pu}^{rms}(M_i,\ \alpha)$ with $(M_i,\ \alpha)$ at $\alpha\ \in\left[0,\frac{\pi}{3}\right]$. As shown in Figure 5.7, the flux linkage ripple of NSWPM is lower than that of AZSPWM. However, NSWPM has limitations that it cannot output the command vector with a modulation index $M_i$ lower than 0.61. Hybrid modulation could extend the output region and reduce the flux linkage ripple. In addition to hybrid modulation, varying the switching frequency can also smooth the fluctuation of harmonics caused by $u^*$ and $\alpha$.

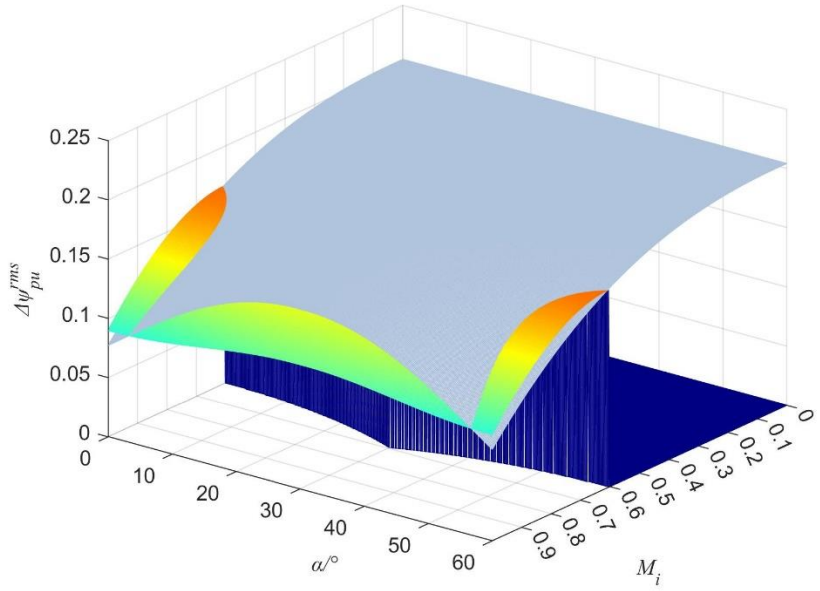


Figure 5.7 Normalized flux linkage ripple values of AZSPWM (colored), NSPWM (gray).

### 5.1.3 Modulation Method Selection and Switching Frequency Table Generation

While avoiding the use of zero vectors can reduce electromagnetic emissions at the source, it can also increase the harmonic content of flux linkage and current. Furthermore, even with this technique, current harmonics concentrated at integer multiples of the switching frequency may still cause local interference peaks and exceed regulatory limits. The application of variable frequency methods can disperse EMI energy over a wider frequency range, enabling products to pass certification standards such as FCC and CE, which has garnered widespread attention [114,115]. At the same time, the current ripple is an important indicator for evaluating inverter performance. The increase in the RMS value of current ripple may cause motor torque fluctuations, eddy current and hysteresis losses to increase, and even cause permanent demagnetization of permanent magnets due to temperature rise. Therefore, while meeting mandatory certification regulations, efforts should also be made to minimize the current ripple of the inverter.

Zero vectors can be used for modulation if the EMI radiation energy is not the core concern. However, to achieve minimal current ripple under the same number of switching cycles, a hybrid modulation method of three modulation methods can be employed within one electrical fundamental period $T_e = 2\pi\omega_e$[116]. The flux linkage harmonics $\Delta\psi^{rms}$ of the first sector's SVPWM, DPWM012, and DPWM721 modulation methods can be plotted in a cylindrical coordinate system, as illustrated in Figure 5.8. In the colored region of the low modulation degree (i.e., $(M_i,\ \alpha) \in Z_{0127}$), SVPWM is used, whereas in the red region of the high modulation degree (i.e., $(M_i,\ \alpha) \in Z_{721}$), DPWM721 is utilized. DPWM012 is utilized in the black region (i.e.,$(M_i,\ \alpha) \in Z_{012}$). The flux linkage ripple can be reduced by utilizing a hybrid modulation of these three methods.

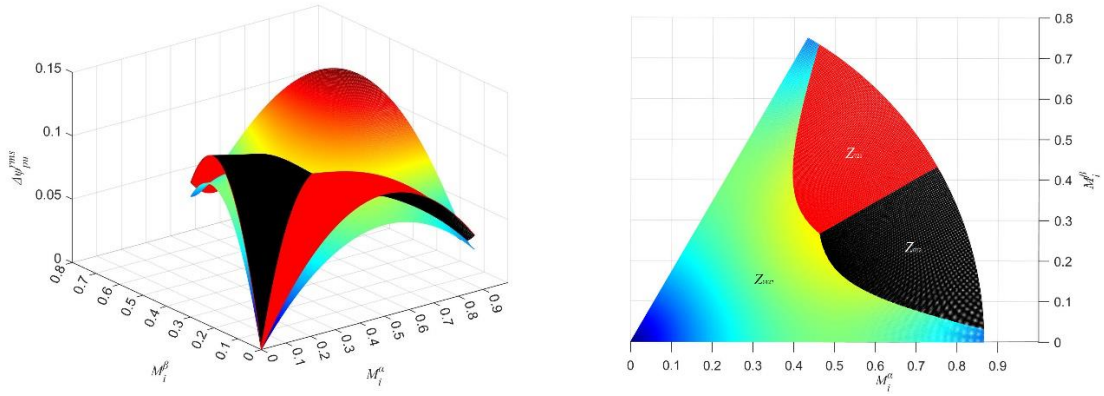

Figure 5.8 The flux linkage linkage harmonics $\Delta\psi^{rms}$ of voltage in the first sector using SVPWM (colored), DPWM012 (black), and DPWM721 (red) in a cylindrical coordinate system and the block diagram for selecting the modulation method in the first sector.

When it is necessary to reduce EMI emission, a hybrid modulation method that switches between AZSPWM and NSPWM can be used for common-mode voltage suppression. The normalized RMS flux linkage ripple of NSPWM over a complete electrical fundamental period $T_e$ and AZSPWM in the first sector are plotted in cylindrical coordinates, as shown in Figure 5.9. NSPWM is used in the colored region of high modulation degree where $(M_i,\ \alpha) \in Z_{321}$, while AZSPWM is used in the black region of low modulation degree where $(M_i,\ \alpha) \in Z_{3216}$. By combining these two methods, common-mode voltage can be reduced while flux linkage ripple is also reduced.

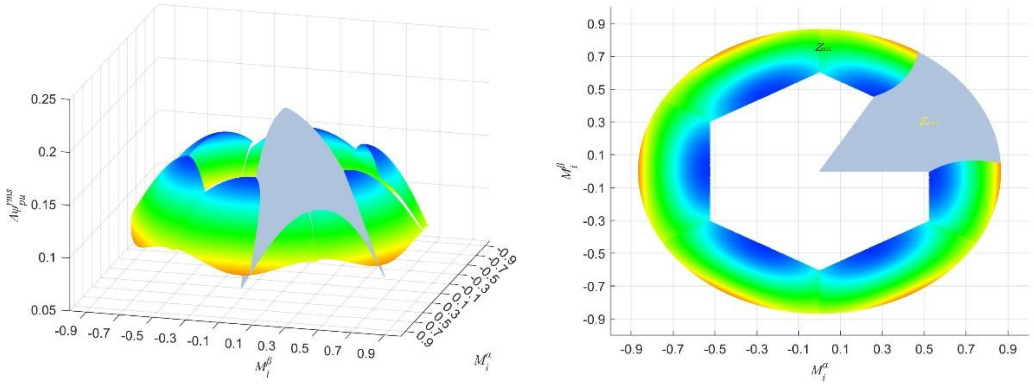

Figure 5.9 The flux linkage harmonics $\Delta\psi^{rms}$ of voltage in the first sector using AZSPWM (grey), and NSPWM (grey) in a cylindrical coordinate system and the block diagram for selecting the modulation method in the first sector.

A unique set of PWM voltages can be determined by the modulation method and a given voltage vector $\vec{u}^*(M_i,\ \alpha)$. In steady-state conditions, where the electrical fundamental period is much greater than the switching period and the voltage drop across resistance and back-EMF is ignored, the current ripple in one switching period $T_s$ is proportional to the switching period and inversely proportional to the inductance for a surface-mounted synchronous motor, as represented by (5.19).

$$\Delta I\ \ (M_i,\ \alpha) = \frac{1}{L}\int_0^{\frac{T_s}{2}} \left(U_{pwm}(t) - u^*(M_i,\ \alpha)\right) dt \tag{5.19}$$

Assuming constant inductance, a fixed peak-to-peak current ripple can be achieved by adjusting the switching frequency $T_s$ as a new degree of freedom. Specifically, the switching frequency $T_s$ is proportional to the normalized value of the flux linkage harmonic $\Delta\psi_{pu}^{rms}$, and inversely proportional to $\Delta\psi_{pu}^{rms}(M_i,\ \alpha)$ averaged over the given voltage angle $\alpha$. The hybrid modulation switching frequencies $T_{s1}(M_i,\ \alpha)$ (with zero vector) and $T_{s2}(M_i,\ \alpha)$ (without zero vector) can be calculated by (5.20) and (5.21). For five-segment PWM, the switching frequency is multiplied by $2/3$ to maintain an equal number of switch actions. The constant switching frequency modulation period is denoted by $T_{base}$, and in this chapter, $T_{base}$ is set to $1/5000\,s$.

$$T_{s1}(M_i,\ \alpha) = \begin{cases} T_{base}\dfrac{\int_0^{\frac{\pi}{3}} \Delta\psi_{0127pu}^{rms}(M_i,\ \alpha)d\alpha}{\frac{\pi}{3}\Delta\psi_{0127pu}^{rms}(M_i,\ \alpha)} & ,\quad (M_i,\ \alpha) \in Z_{0127} \\ \dfrac{2T_{base}}{3}\dfrac{\int_0^{\frac{\pi}{3}} \Delta\psi_{012pu}^{rms}(M_i,\ \alpha)d\alpha}{\frac{\pi}{3}\Delta\psi_{012pu}^{rms}(M_i,\ \alpha)} & ,\quad (M_i,\ \alpha) \in Z_{012} \\ \dfrac{2T_{base}}{3}\dfrac{\int_0^{\frac{\pi}{3}} \Delta\psi_{721pu}^{rms}(M_i,\ \alpha)d\alpha}{\frac{\pi}{3}\Delta\psi_{721pu}^{rms}(M_i,\ \alpha)} & ,\quad (M_i,\ \alpha) \in Z_{721} \end{cases} \tag{5.20}$$

$$T_{s2}(M_i,\ \alpha) = \begin{cases} T_{base}\dfrac{\int_0^{\frac{\pi}{3}} \Delta\psi_{3216pu}^{rms}(M_i,\ \alpha)d\alpha}{\frac{\pi}{3}\Delta\psi_{3216pu}^{rms}(M_i,\ \alpha)} & ,\quad (M_i,\ \alpha) \in Z_{3216} \\ \dfrac{2T_{base}}{3}\dfrac{\int_0^{\frac{\pi}{3}} \Delta\psi_{321pu}^{rms}(M_i,\ \alpha)d\alpha}{\frac{\pi}{3}\Delta\psi_{321pu}^{rms}(M_i,\ \alpha)} & ,\quad (M_i,\ \alpha) \in Z_{321} \end{cases} \tag{5.21}$$

When $T_{base}$ is constant, the switching frequency $T_s(M_i,\ \alpha)$ varies based on the magnitude and direction of the given voltage vector. To reduce the computational burden, $T_s(M_i,\ \alpha)$ can be pre-stored in an offline lookup table in the microcontroller.

The software flowchart for calculating the switching frequency using offline lookup tables is shown in Figure 5.10.

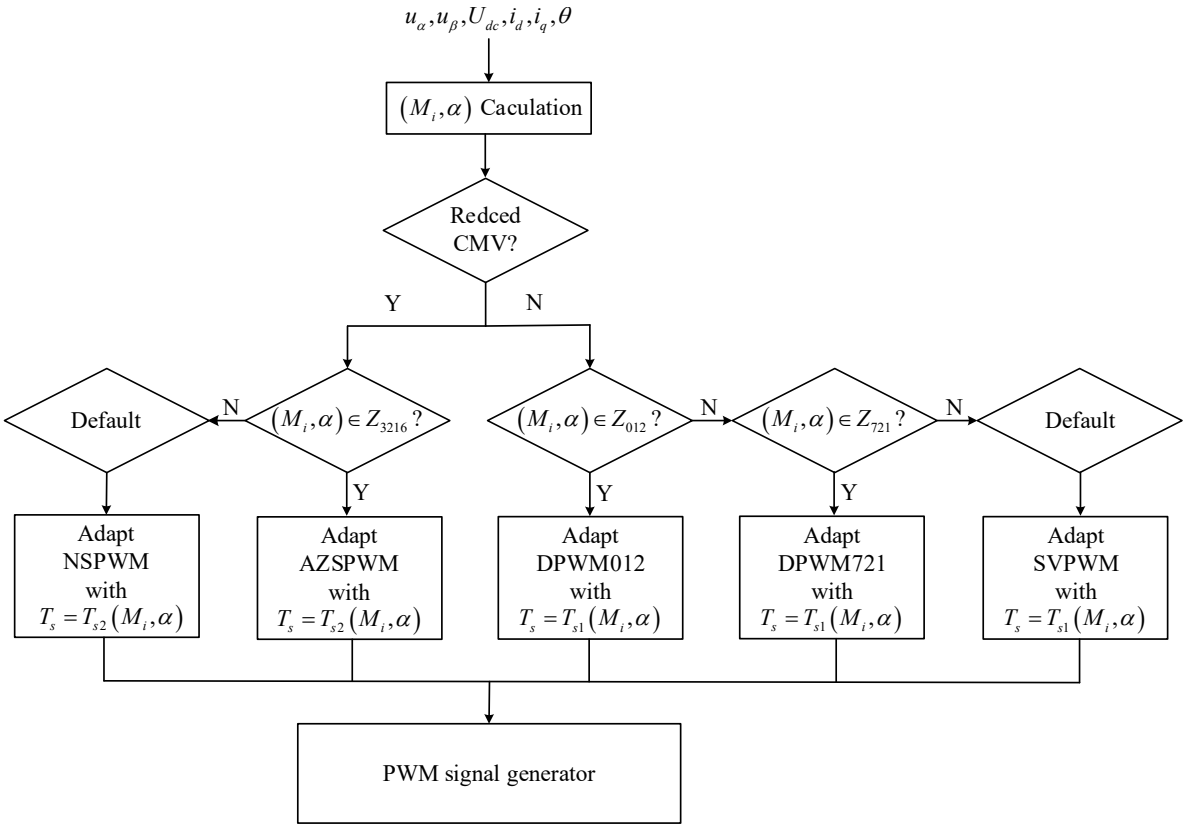


Figure 5.10 Software flow chart of hybrid spread spectrum PWM.

## 5.2 HYBRID SPREAD SPECTRUM PWM CONSIDERING SATURATION OF MOTOR

Motors with high torque density typically keep a high magnetic field density inside them. When the motor is excited with a current several times greater than its rated value, the iron core of the motor undergoes saturation, leading to a decrease in inductance and an increase in current ripple. Under these conditions, the method described above cannot precisely control the current ripple by varying the switching frequency. The mathematical model of the surface-mounted PMSM given by (5.1) and (5.2) is based on small signal theory assuming that the inductance is a constant that does not change with current, which will lead to control errors.

Slots have to be machined on the stator to accommodate the windings. This results in a non-sinusoidal distribution of armature reaction flux in the air gap. Due to the rotation of the rotor, the d-axis inductance varies periodically, with 6 fluctuations in each electrical cycle. The electric machine model considering slots is shown in (5.18).

For a certain modulation method, the given voltage $u^*(M_i,\ \alpha)$ is generated by a determined set of PWM voltages within a sub-switching period. For the surface-mounted PMSM working in steady-state, considering cross-saturation and slotting effects and neglecting the influence of voltage drop across the resistance and current ripple $\Delta I$ on the inductance $L_s$, the result is shown in (5.22).

$$\Delta I\ \ (M_i,\ \alpha) = \frac{1}{L_s(i_d, i_q, \theta)} \int_0^{\frac{T_s}{2}} \left( U_{pwm}(t) - u^*(M_i,\ \alpha) \right) dt \tag{5.22}$$

Taking into account the effects of slotting and cross-saturation, the switching frequency is also influenced by the dynamic inductance. As shown in (5.23) and (5.24), $T_{s1'}(M_i, \alpha, i_d, i_q, \theta)$ and $T_{s2'}(M_i, \alpha, i_d, i_q, \theta)$ are the target switching frequency of the hybrid modulation method with and without zero vectors, respectively.

$$T_{s1'}(M_i, \alpha, i_d, i_q, \theta) = \begin{cases} \dfrac{min\left[L_{dd}(i_d, i_q, \theta), L_{qq}(i_d, i_q, \theta)\right]}{\int_0^{\frac{\pi}{3}} L_{dd}(i_{d0}, i_{q0}, \theta) d\theta} \dfrac{\int_0^{\frac{\pi}{3}} \Delta\psi_{0127pu}^{rms}(M_i, \alpha) d\alpha}{\Delta\psi_{0127pu}^{rms}(M_i, \alpha)} T_{base}, (M_i, \alpha) \in Z_{0127} \\ \dfrac{3 * min\left[L_{dd}(i_d, i_q, \theta), L_{qq}(i_d, i_q, \theta)\right]}{2\int_0^{\frac{\pi}{3}} L_{dd}(i_{d0}, i_{q0}, \theta) d\theta} \dfrac{\int_0^{\frac{\pi}{3}} \Delta\psi_{012pu}^{rms}(M_i, \alpha) d\alpha}{\Delta\psi_{012pu}^{rms}(M_i, \alpha)} T_{base}, (M_i, \alpha) \in Z_{012} \\ \dfrac{3 * min\left[L_{dd}(i_d, i_q, \theta), L_{qq}(i_d, i_q, \theta)\right]}{2\int_0^{\frac{\pi}{3}} L_{dd}(i_{d0}, i_{q0}, \theta) d\theta} \dfrac{\int_0^{\frac{\pi}{3}} \Delta\psi_{721pu}^{rms}(M_i, \alpha) d\alpha}{\Delta\psi_{721pu}^{rms}(M_i, \alpha)} T_{base}, (M_i, \alpha) \in Z_{721} \end{cases} \tag{5.23}$$

$$T_{s2'}(M_i, \alpha, i_d, i_q, \theta) = \begin{cases} \dfrac{min\left[L_{dd}(i_d, i_q, \theta), L_{qq}(i_d, i_q, \theta)\right]}{\int_0^{\frac{\pi}{3}} L_{dd}(i_{d0}, i_{q0}, \theta) d\theta} \dfrac{\int_0^{\frac{\pi}{3}} \Delta\psi_{3216pu}^{rms}(M_i, \alpha) d\alpha}{\Delta\psi_{3216pu}^{rms}(M_i, \alpha)} T_{base}, (M_i, \alpha) \in Z_{3216} \\ \dfrac{3 * min\left[L_{dd}(i_d, i_q, \theta), L_{qq}(i_d, i_q, \theta)\right]}{2\int_0^{\frac{\pi}{3}} L_{dd}(i_{d0}, i_{q0}, \theta) d\theta} \dfrac{\int_0^{\frac{\pi}{3}} \Delta\psi_{321pu}^{rms}(M_i, \alpha) d\alpha}{\Delta\psi_{321pu}^{rms}(M_i, \alpha)} T_{base}, (M_i, \alpha) \in Z_{321} \end{cases} \tag{5.24}$$

Equations (5.23) and (5.24) are functions of five variables, with inductance values and current dependent on the rotor angle. The dynamic inductance parameters can be obtained through finite element simulation or static/dynamic offline parameter identification. The part related to inductance variation, $min\left[L_{dd}(i_d, i_q, \theta), L_{qq}(i_d, i_q, \theta)\right] / \int_0^{\frac{\pi}{3}} L_{dd}(i_{d0}, i_{q0}, \theta) d\theta$, can be stored as a separate table to represent the inductance ratio of the operating current and rated current.

If the cross-saturation caused by $i_d$ and $i_q$ is considered, and the inductance fluctuation caused by slotting is ignored, the influence of rotor position angle $\theta$ on inductance can be ignored. According to (5.25), $T_{s1''}(M_i, \alpha, i_d, i_q)$ (using zero vectors) and $T_{s2''}(M_i, \alpha, i_d, i_q)$ (not using zero vectors) should be used to determine the switching frequency. The part of inductance change, $min\left[L_{dd}(i_d, i_q), L_{qq}(i_d, i_q)\right] / L_{dd}(i_{d0}, i_{q0})$, can be stored separately in a look-up table to represent the inductance ratio of operating current and rated current. Using the look-up table can improve the computational speed. The software flow chart is shown in Figure 5.11.

$$T_{s1''}(M_i, \alpha, i_d, i_q) = \begin{cases} \dfrac{min\left[L_{dd}(i_d, i_q), L_{qq}(i_d, i_q)\right]}{L_{dd}(i_{d0}, i_{q0})} \dfrac{\int_0^{\frac{\pi}{3}} \Delta\psi_{0127pu}^{rms}(M_i, \alpha) d\alpha}{\Delta\psi_{0127pu}^{rms}(M_i, \alpha)} T_{base}, (M_i, \alpha) \in Z_{0127} \\ \dfrac{3 * min\left[L_{dd}(i_d, i_q), L_{qq}(i_d, i_q)\right]}{2L_{dd}(i_{d0}, i_{q0})} \dfrac{\int_0^{\frac{\pi}{3}} \Delta\psi_{012pu}^{rms}(M_i, \alpha) d\alpha}{\Delta\psi_{012pu}^{rms}(M_i, \alpha)} T_{base}, (M_i, \alpha) \in Z_{012} \\ \dfrac{3 * min\left[L_{dd}(i_d, i_q), L_{qq}(i_d, i_q)\right]}{2L_{dd}(i_{d0}, i_{q0})} \dfrac{\int_0^{\frac{\pi}{3}} \Delta\psi_{721pu}^{rms}(M_i, \alpha) d\alpha}{\Delta\psi_{721pu}^{rms}(M_i, \alpha)} T_{base}, (M_i, \alpha) \in Z_{721} \end{cases} \tag{5.25}$$

$$T_{s2''}(M_i,\alpha,i_d,i_q)=\begin{cases}\dfrac{min\left[L_{dd}(i_d,i_q),L_{qq}(i_d,i_q)\right]}{L_{dd}(i_{d0},i_{q0})}\dfrac{\int_0^{\frac{\pi}{3}}\Delta\psi_{3216pu}^{rms}(M_i,\alpha)d\alpha}{\Delta\psi_{3216pu}^{rms}(M_i,\alpha)}T_{base}\ ,(M_i,\alpha)\in Z_{3216}\\ \dfrac{3*min\left[L_{dd}(i_d,i_q),L_{qq}(i_d,i_q)\right]}{2L_{dd}(i_{d0},i_{q0})}\dfrac{\int_0^{\frac{\pi}{3}}\Delta\psi_{321pu}^{rms}(M_i,\alpha)d\alpha}{\Delta\psi_{321pu}^{rms}(M_i,\alpha)}T_{base}\ ,(M_i,\alpha)\in Z_{321}\end{cases} \tag{5.26}$$

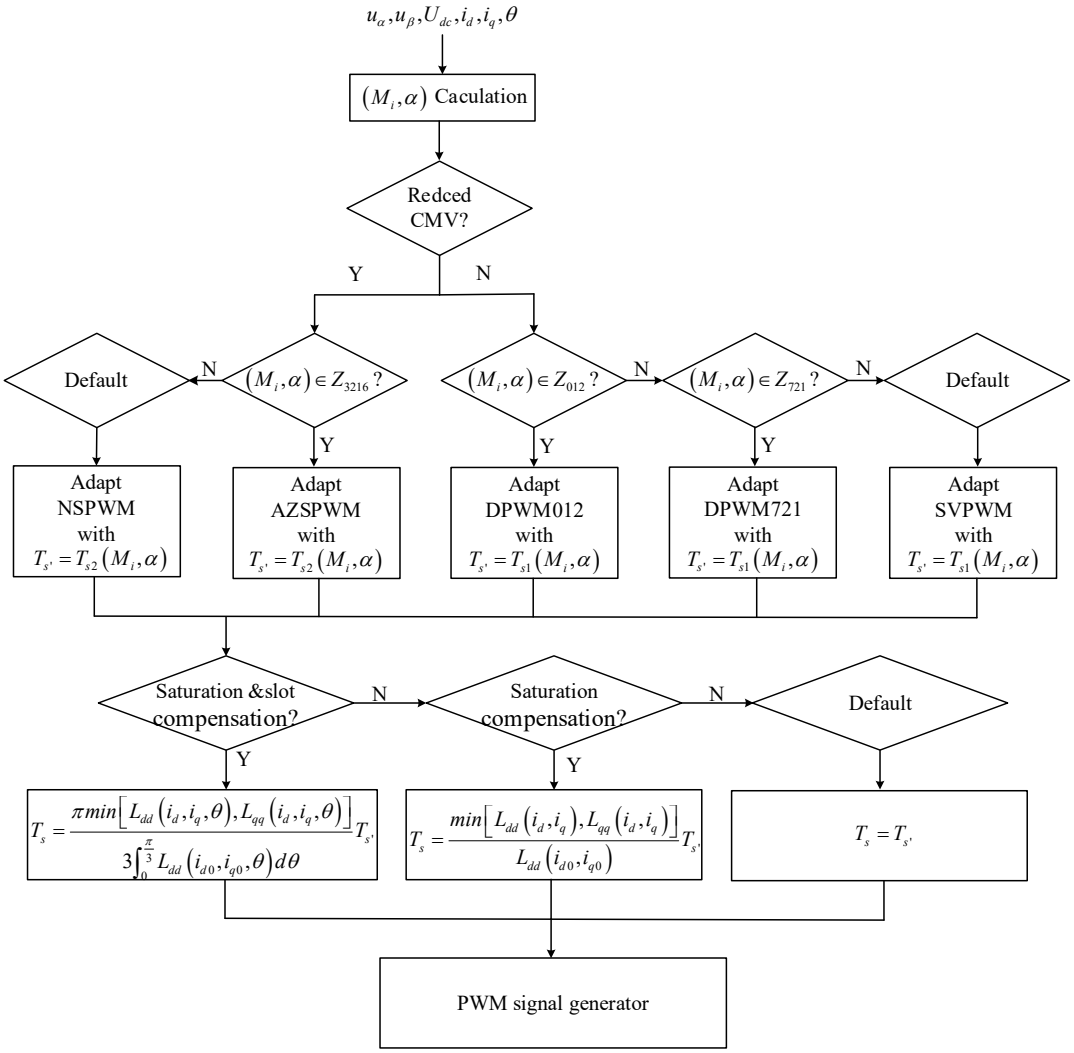


Figure 5.11 Software flow chart of hybrid spread spectrum PWM considering saturation and slot compensation.

## 5.3 SIMULATION RESULT

In this section, various modulation methods are verified through simulations. Two mathematical models are used during the simulation process: one neglects saturation in the small signal motor model, and the other considers cross-saturation and slotting effects. In this study, Simulink simulations are utilized to validate the current ripple across various modulation methods, taking advantage of the high-speed capabilities of MATLAB/Simulink models.

### 5.3.1 Simulation result based on the small-signal motor model

The motor parameters are presented in Table 5.2, with the rated working current of 5A corresponding to the rated inductance. In the simulation, the motor runs at 1000rpm with a base frequency of 166.66Hz and $M_i$ value of 0.55. The simulation results are obtained by performing the fast Fourier transform on the current. Three-phase current, A-phase fundamental current, switching period, A-phase current ripple, and A-phase current spectrum for different modulation methods within 25ms are shown in the result. The SVPWM is utilized to validate the efficacy of the spread spectrum modulation technique in the following part.

Table 5.2 Parameters of small-signal motor model.

| Parameters | Small-Signal Motor Model |
|---|---|
| Number of pole pairs | 10 |
| Stator winding resistance | 3.45 Ω |
| d-axis inductance | 0.81 mH [1] |
| q-axis inductance | 0.95 mH [1] |
| PM flux-linkage | 0.012Wb |

1 The data are measured at $i_d = 0A$, $i_q = 5A$.

5.3.1.1 Space Vector Pulse Width Modulation

*A. Constant switching frequency*

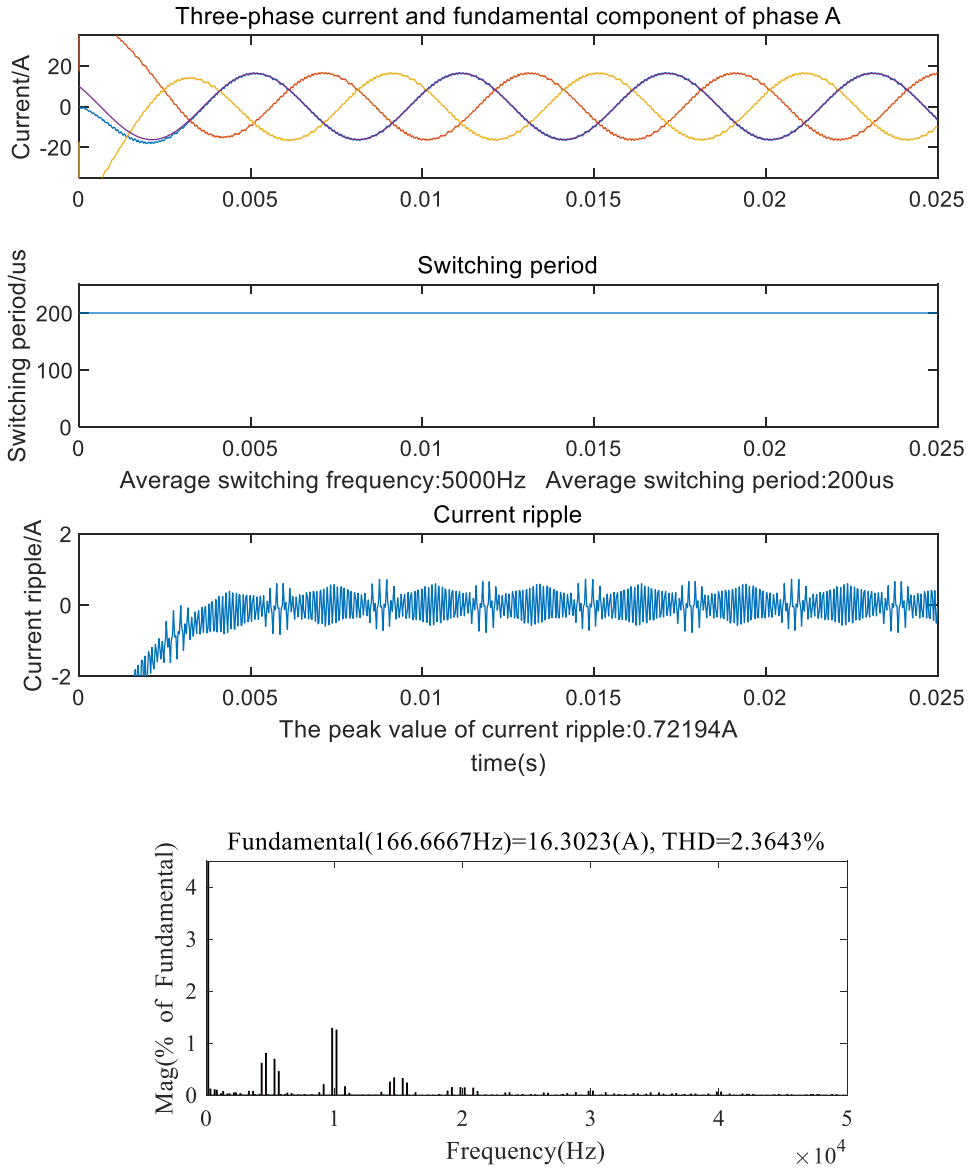


Figure 5.12 Three-phase current, A-phase fundamental current, switching period, A-phase current ripple, and A-phase current spectrum for SVPWM with constant switching frequency for small-signal motor model.

Figure 5.12 demonstrates that employing SVPWM with a switching frequency of 5000Hz leads to periodic variations in the current ripple. The harmonic spectrum exhibits a concentration around integer multiples of the switching frequency, along with its sidebands.

*B. Variable switching frequency according to RMS value of flux linkage*

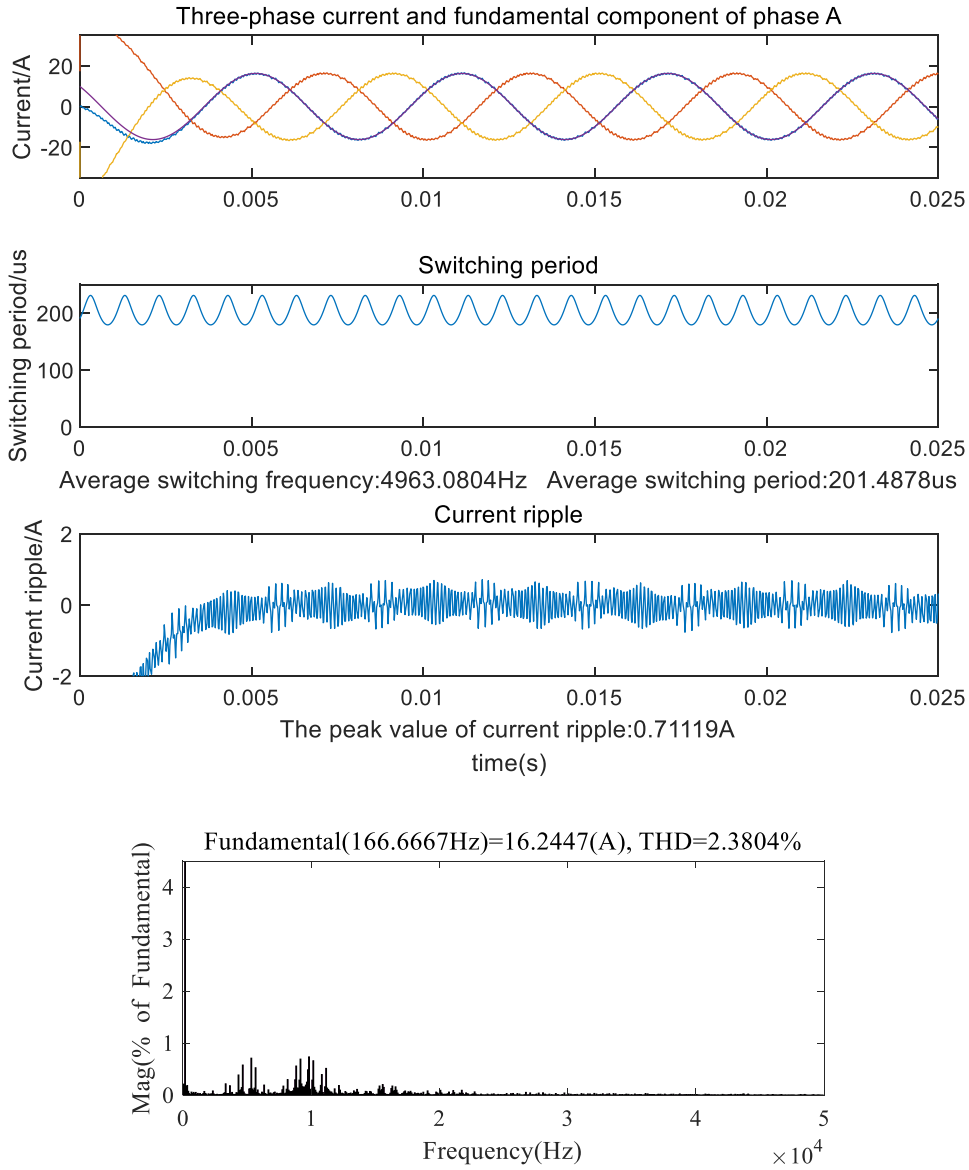


Figure 5.13 Three-phase current, A-phase fundamental current, switching period, A-phase current ripple, and A-phase current spectrum for SVPWM with varied switching frequency according to RMS value of flux linkage for small-signal motor model.

The switching frequency varies six times per fundamental period, and the average switching frequency is about 5000Hz as the given voltage angle periodically changes, as shown in Figure 5.13. Additionally, the current ripple exhibits periodic variations with a similar peak-to-peak value and total harmonic distortion to those in Figure 5.12, but with a more dispersed harmonic spectrum. To verify the effectiveness of the hybrid spread spectrum modulation method, AZSPWM and NSWPM are simulated in the next part.

5.3.1.2 AZSPWM and NSPWM

*A. AZSPWM with constant switching frequency*

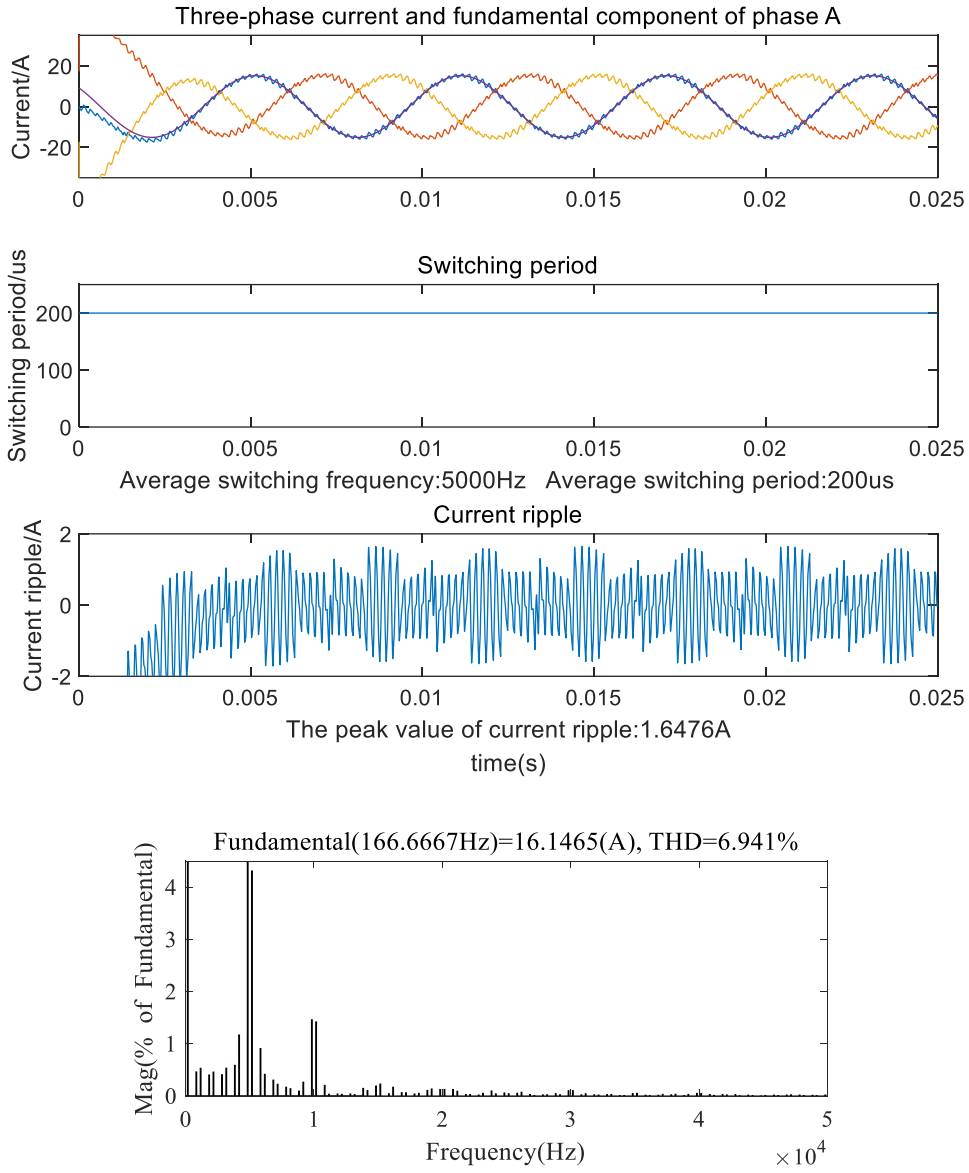


Figure 5.14 Three-phase current, A-phase fundamental current, switching period, A-phase current ripple, and A-phase current spectrum for AZSPWM with constant switching frequency for the small-signal motor model.

The current ripple exhibits periodic variation with concentrated harmonics after being modulated by AZSPWM at a constant switching frequency of $f_s$=5000Hz. However, the total harmonic distortion rate is higher compared to the SVPWM modulation with a constant switching frequency in Figure 5.12.

*B. NSPWM with constant switching frequency*

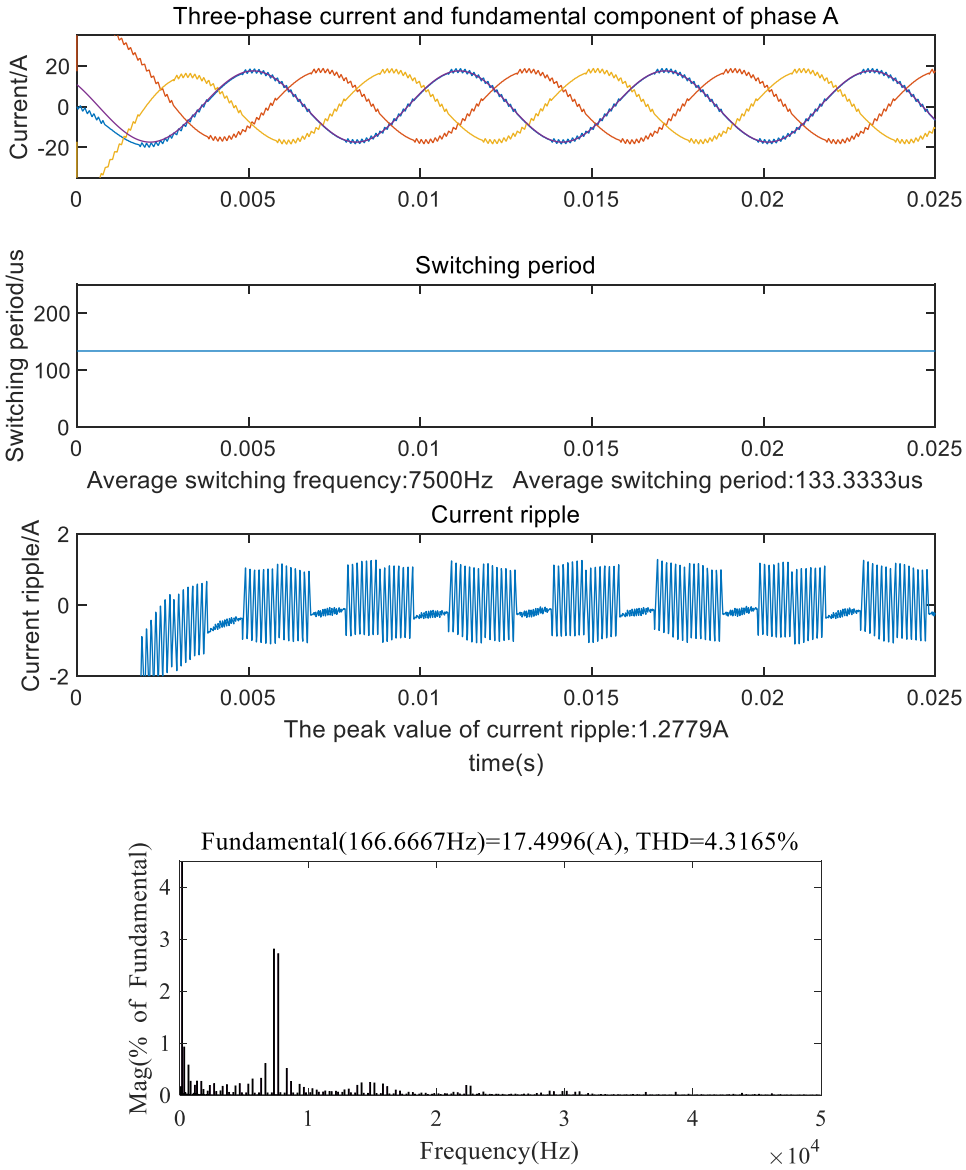


Figure 5.15 Three-phase current, A-phase fundamental current, switching period, A-phase current ripple, and A-phase current spectrum for NSPWM with constant switching frequency for small-signal motor model.

Since using NSPWM cannot linearly output the voltage of $M_i < 0.5$, $M_i$ was increased by 1.15 times to 0.6325 to verify the NSPWM. The switching frequency is set to 7500Hz to ensure the same number of switching actions per switching period as AZSPWM. As the result shows, the current ripple changes periodically, the fundamental current increases with the increase of the given voltage, and the harmonic distortion and total harmonic distortion of the current are reduced compared to the AZSPWM method.

*C. AZSPWM/NSPWM hybrid modulation according to RMS value of flux linkage*

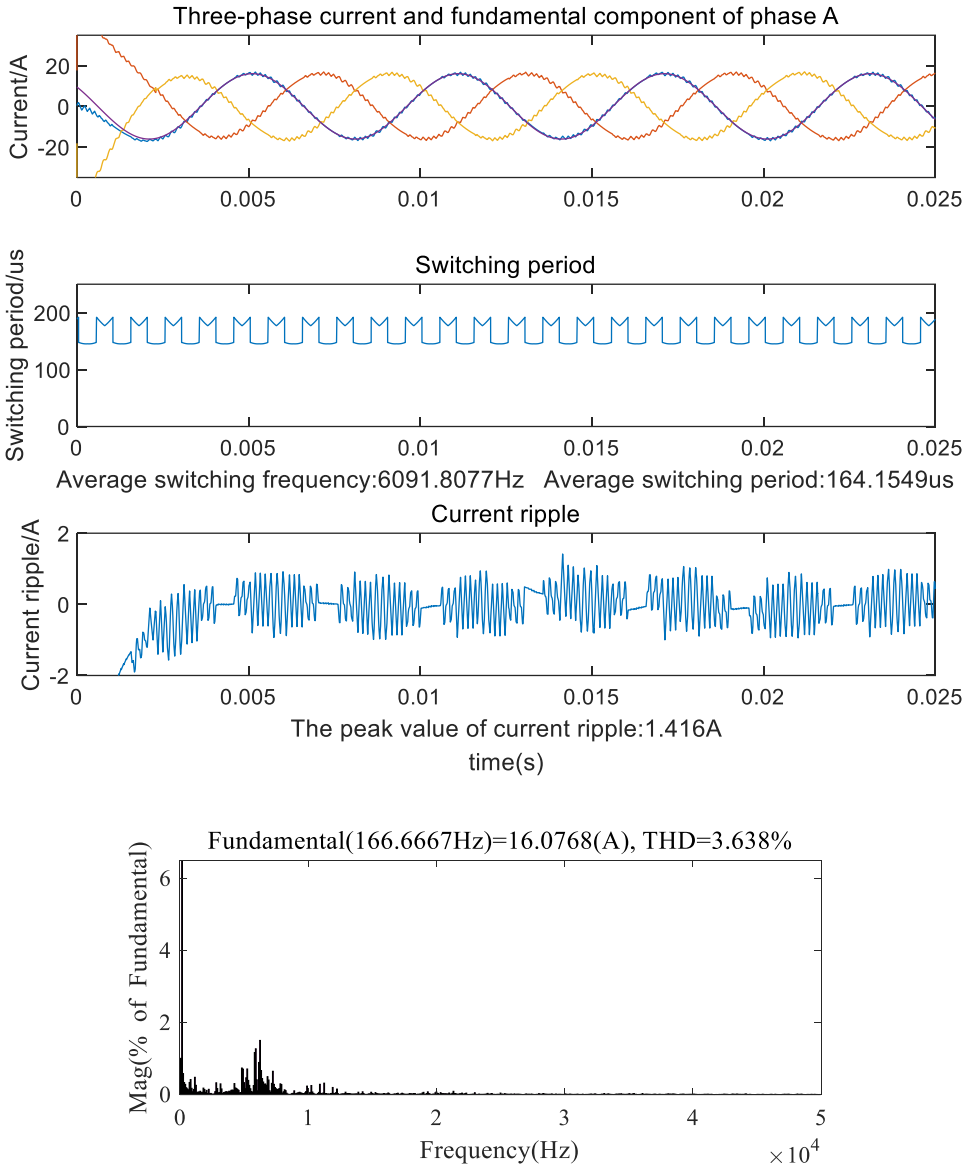


Figure 5.16 Three-phase current, A-phase fundamental current, switching period, A-phase current ripple, and A-phase current spectrum for AZSPWM/NSPWM hybrid modulation with varied switching frequency according to RMS value of flux linkage for the small-signal motor model.

By utilizing a hybrid variable-frequency modulation with ASPWM and NSPWM, the switching frequency periodically fluctuates between 5000Hz and 7500Hz, resulting in six fluctuations per fundamental period. The average number of switching actions is equal to that of a constant switching frequency. The spectral peak at the switching frequency is effectively suppressed.

The waveform displayed below depicts the common mode voltage $U_{no}$ for the techniques of SVPWM and the hybrid modulation techniques of AZSPWM/NSPWM, which shows that the common mode voltage magnitude can be reduced without employing zero vectors.

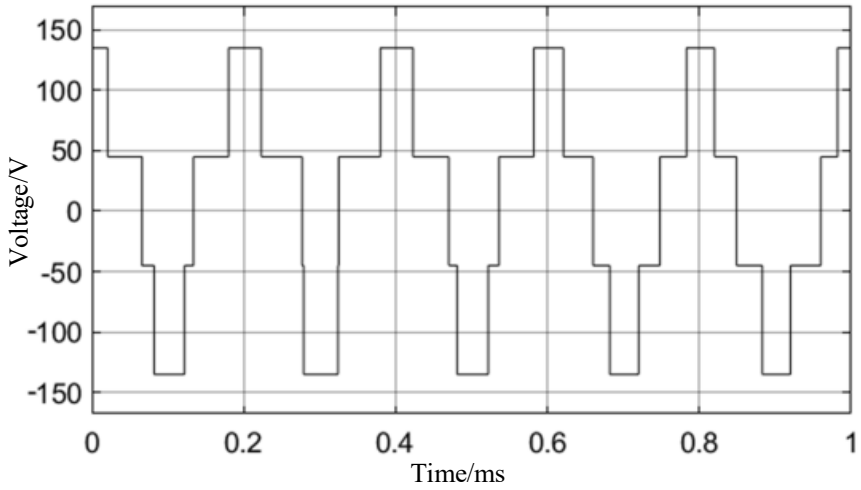


(a) SVPWM method.

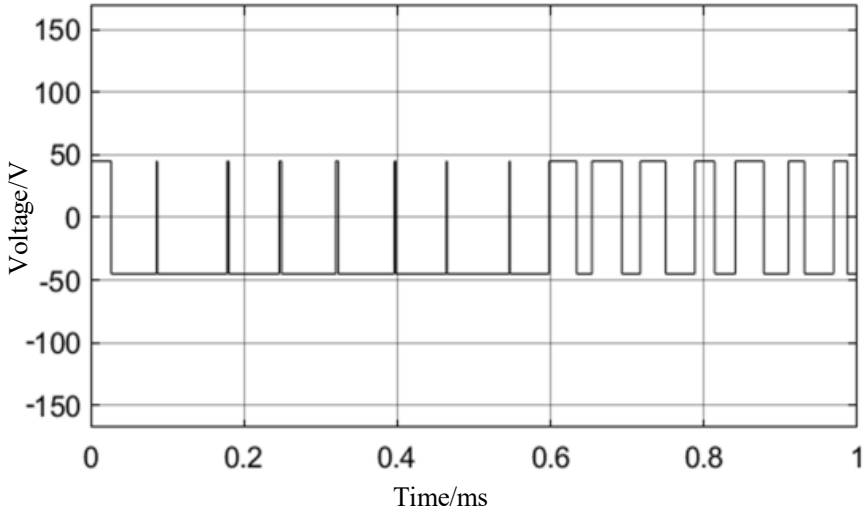


(b) AZSPWM/NSPWM method.

Figure 5.17 The common mode voltage $U_{no}$ for the techniques of SVPWM and the hybrid modulation techniques of AZSPWM/NSPWM.

The aforementioned verification is conducted without considering saturation, where it is observed that the current ripple can be maintained without the need to increase the average switching frequency. But if saturation is considered, the average switching frequency must be increased to suppress the increased current ripple.

## 5.3.2 Simulation results considering both cross-saturation and slotting effects

5.3.2.1 Space Vector Pulse Width Modulation

*A. SVPWM with constant switching frequency*

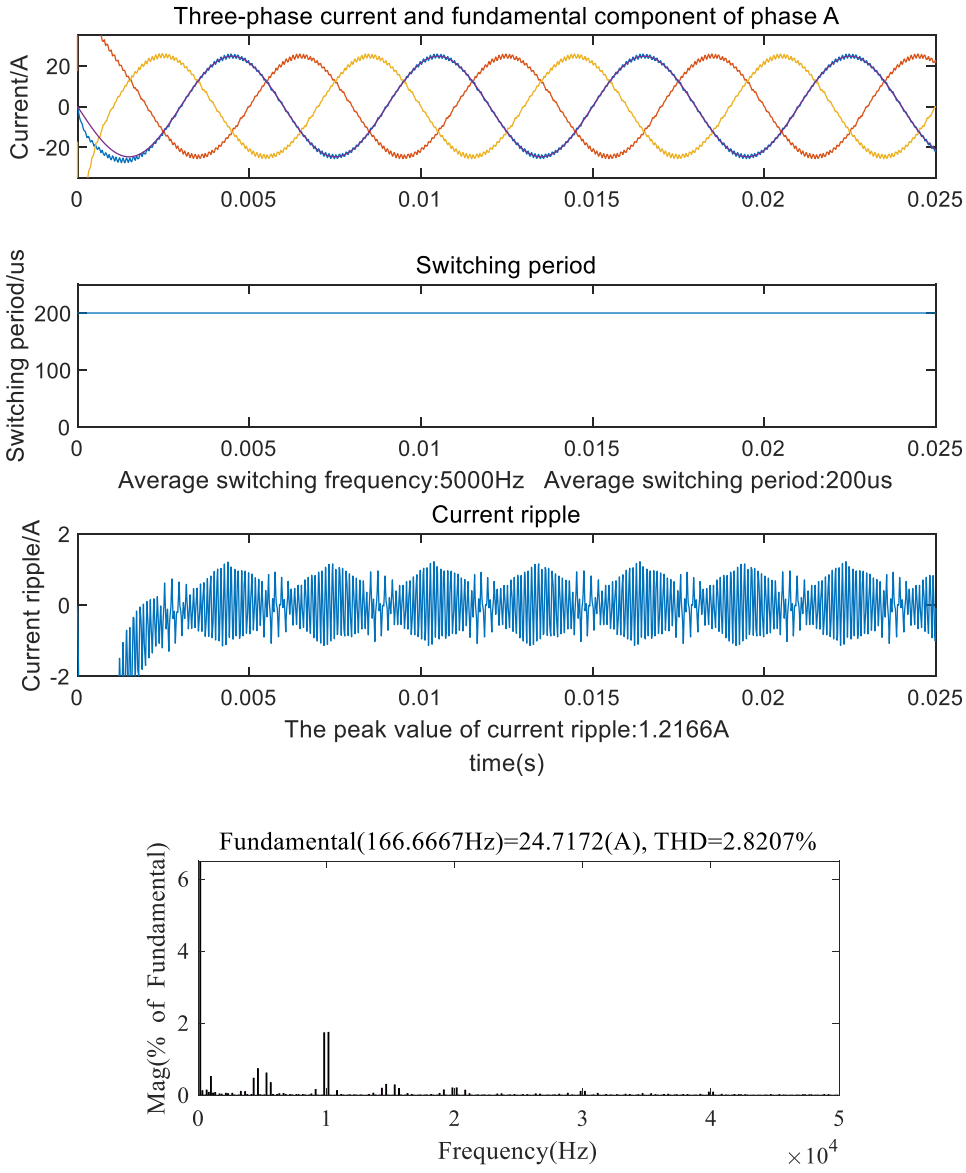


Figure 5.18 Three-phase current, A-phase fundamental current, switching period, A-phase current ripple, and A-phase current spectrum for SVPWM with constant switching frequency considering both cross-saturation and slotting effects.

When applying SVPWM with the constant switching frequency to a saturated motor, the fundamental current significantly increases compared to when it is applied to an unsaturated motor. This is attributed to the reduction in static inductance under the same voltage, leading to a decrease in armature reaction voltage. Additionally, the decrease in dynamic inductance leads to an increase in current ripple and harmonic distortion caused by PWM voltage harmonics. In the spectrum, the peak at 1000Hz corresponds to the current harmonic caused by the slots at 1000rpm.

*B. Variable switching frequency according to RMS value of flux linkage*

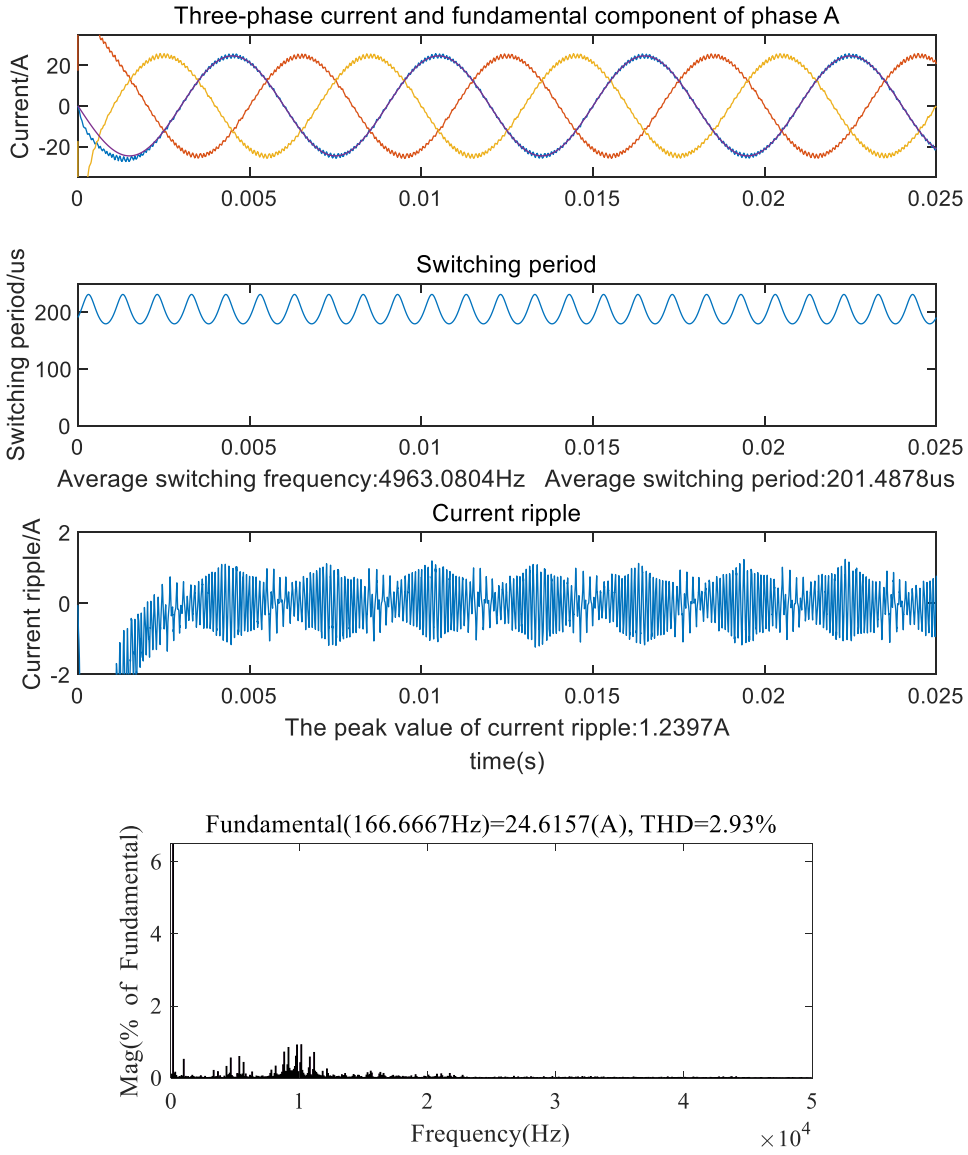


Figure 5.19 Three-phase current, A-phase fundamental current, switching period, A-phase current ripple, and A-phase current spectrum for SVPWM with varied switching frequency according to RMS value of flux linkage considering both cross-saturation and slotting effects.

The look-up table of variable switching frequencies calculated by SVPWM harmonic analysis still suits the motor model that considers cross-saturation and slotting. By searching and using this table based on $M_i$ and $\alpha$, it is possible to reduce harmonic peaks, maintain current ripple, and spread the spectrum. However, it is worth noting that the modulation of switching frequency does not take into account the decrease in dynamic inductance, which leads to higher levels of current ripple and harmonic distortion compared to the corresponding SVPWM modulation results in Section 5.3.1.1.B.

*C. Variable switching frequency considering cross-saturation of PMSM*

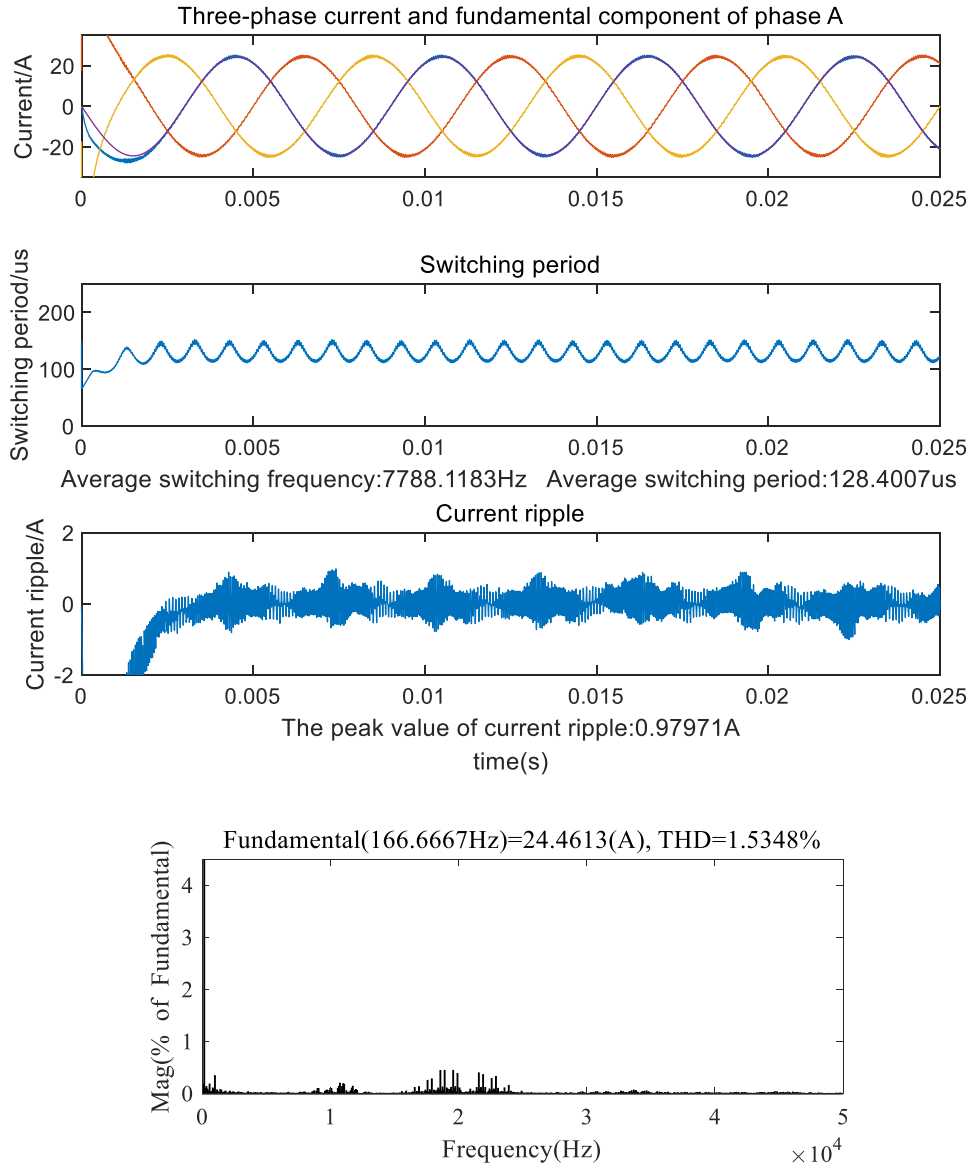


Figure 5.20 Three-phase current, A-phase fundamental current, switching period, A-phase current ripple, and A-phase current spectrum for SVPWM with varied switching frequency according to cross-saturation inductance table considering both cross-saturation and slotting effects.

By referring to the voltage harmonic look-up table and motor cross-saturation inductance look-up table, the switching period $T_{s1}{}_{,}\left(M_i, \alpha, i_d, i_q\right)$ is calculated using (5.25). During the process of increasing the feedback current from its rated state $i_{d0} = 0A, i_{q0} = 5A$ to $i_d = 0A, i_q = 24.46A$, the $q$-axis dynamic inductance decreases by 65%, and the switching frequency gradually increases to around 1.5 times the constant switching frequency. This results in a significant reduction in the current ripple and current harmonic distortion, which are slightly higher than the results of the SVPWM modulation with variable switching frequency for the small-signal motor model in Section 5.3.1.1.B. From the spectrum graph, it is evident that the spectrum shifts towards higher frequencies. However, the spectrum still shows a peak at 1000Hz caused by the slot.

*D. Variable switching frequency considering cross-saturation and slotting effect of PMSM*

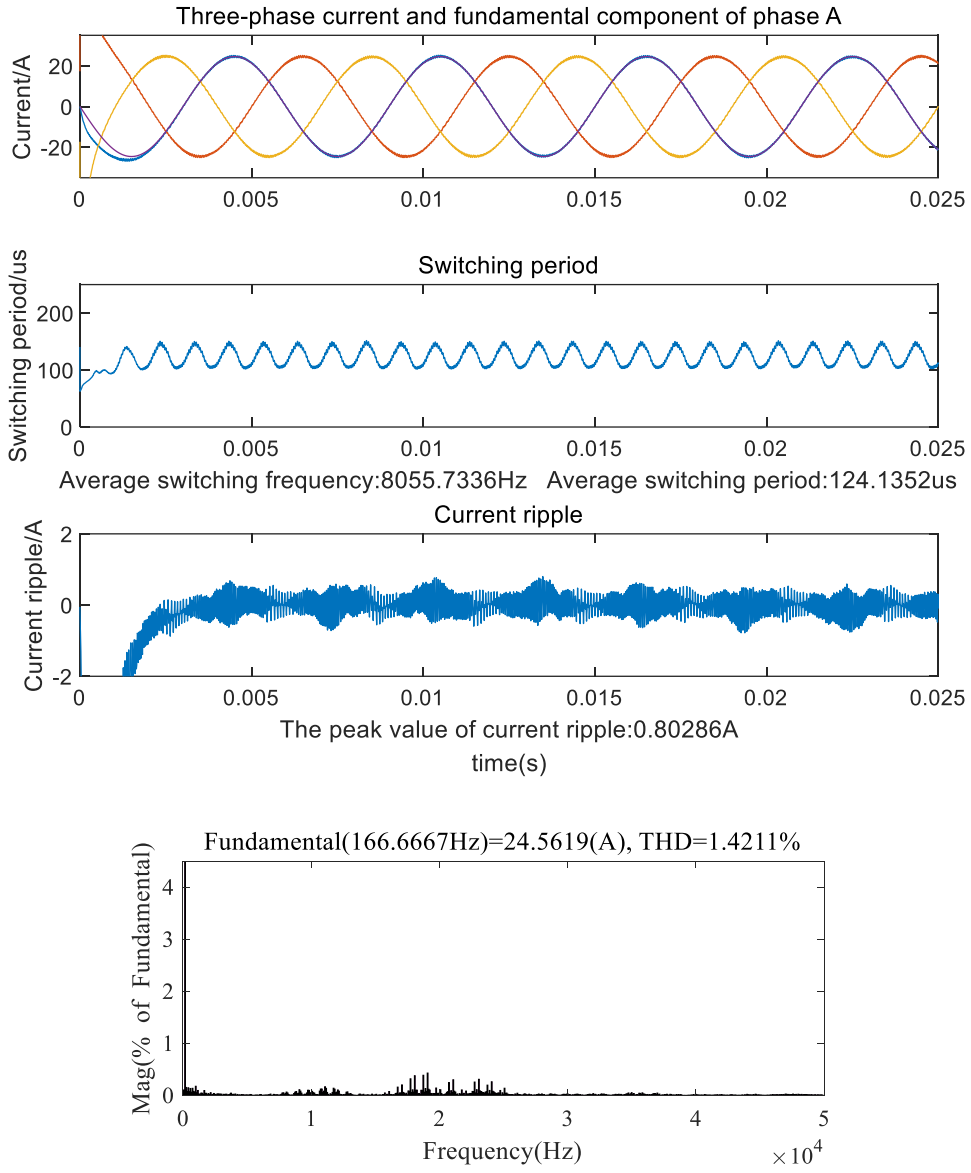


Figure 5.21 Three-phase current, A-phase fundamental current, switching period, A-phase current ripple, and A-phase current spectrum for SVPWM with varied switching frequency according to inductance table considering cross-saturation and slotting effect .

By referring to the voltage harmonic look-up table and the look-up table of cross-saturation and slot inductances for the motor, the switching period $T_{s1}$,$\left(M_i, \alpha, i_d, i_q, \theta\right)$ is calculated by using (5.23). The switching frequency is 3% more than when using the method that only considers cross-saturation. As a result of slot compensation, the harmonic peak at 1000Hz is suppressed. Additionally, there is a further reduction in the current ripple and harmonic distortion, bringing the results closer to those by using SVPWM modulation with variable switching frequency on the small-signal motor model in Section 5.3.1.1.B.

5.3.2.2 AZSPWM and NSPWM

*A. AZSPWM/NSPWM hybrid modulation with the same equivalent switching frequencies*

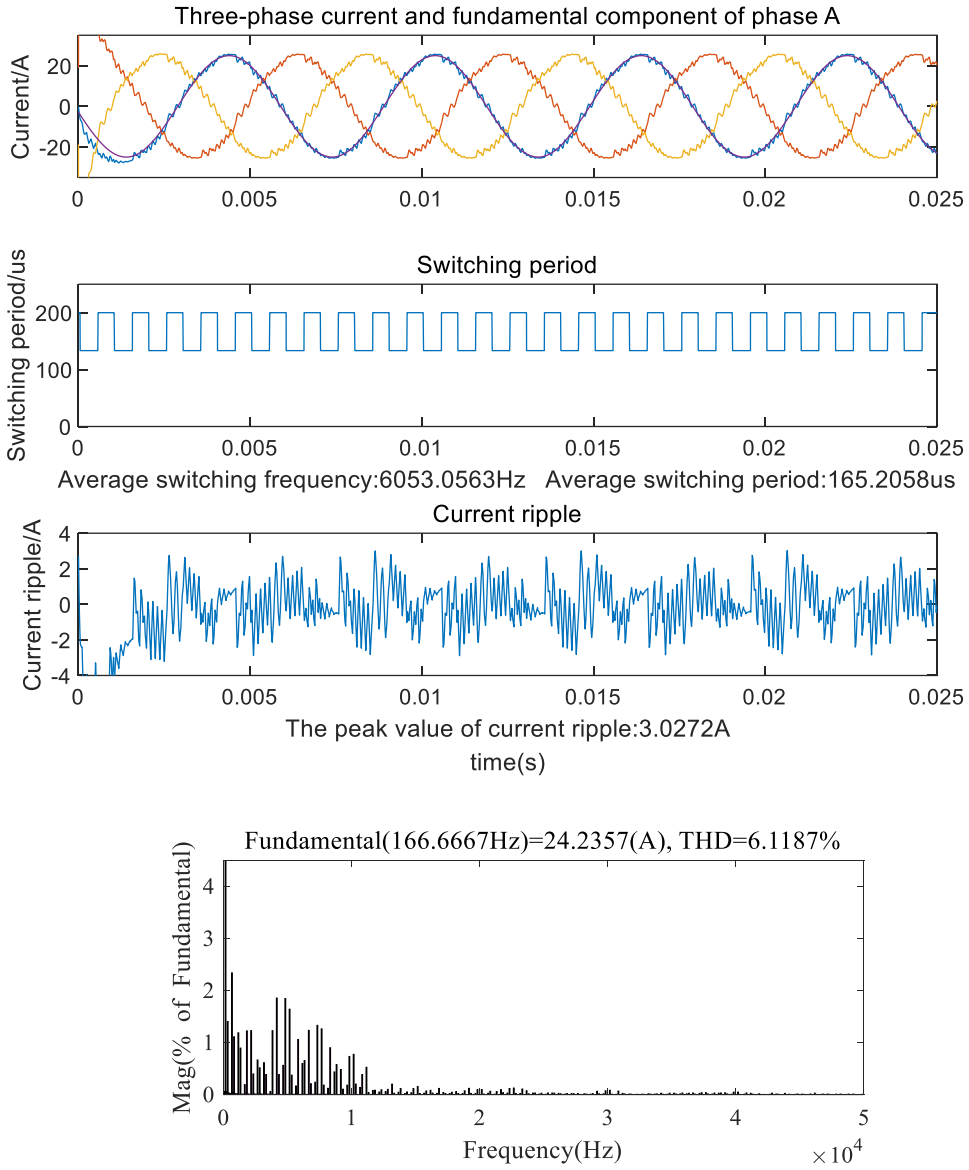


Figure 5.22 Three-phase current, A-phase fundamental current, switching period, A-phase current ripple, and A-phase current spectrum for AZSPWM/NSPWM hybrid modulation with the same equivalent switching frequencies considering both cross-saturation and slotting effects.

When using NSWPM, only high $M_i$ voltage vectors can be outputted, so it is commonly used together with AZSPWM. The switching frequency alternates between 7500Hz and 5000Hz. As a result of saturation, the fundamental current increases.

*B. AZSPWM/NSPWM hybrid modulation with the variable switching frequencies according to RMS value of flux linkage*

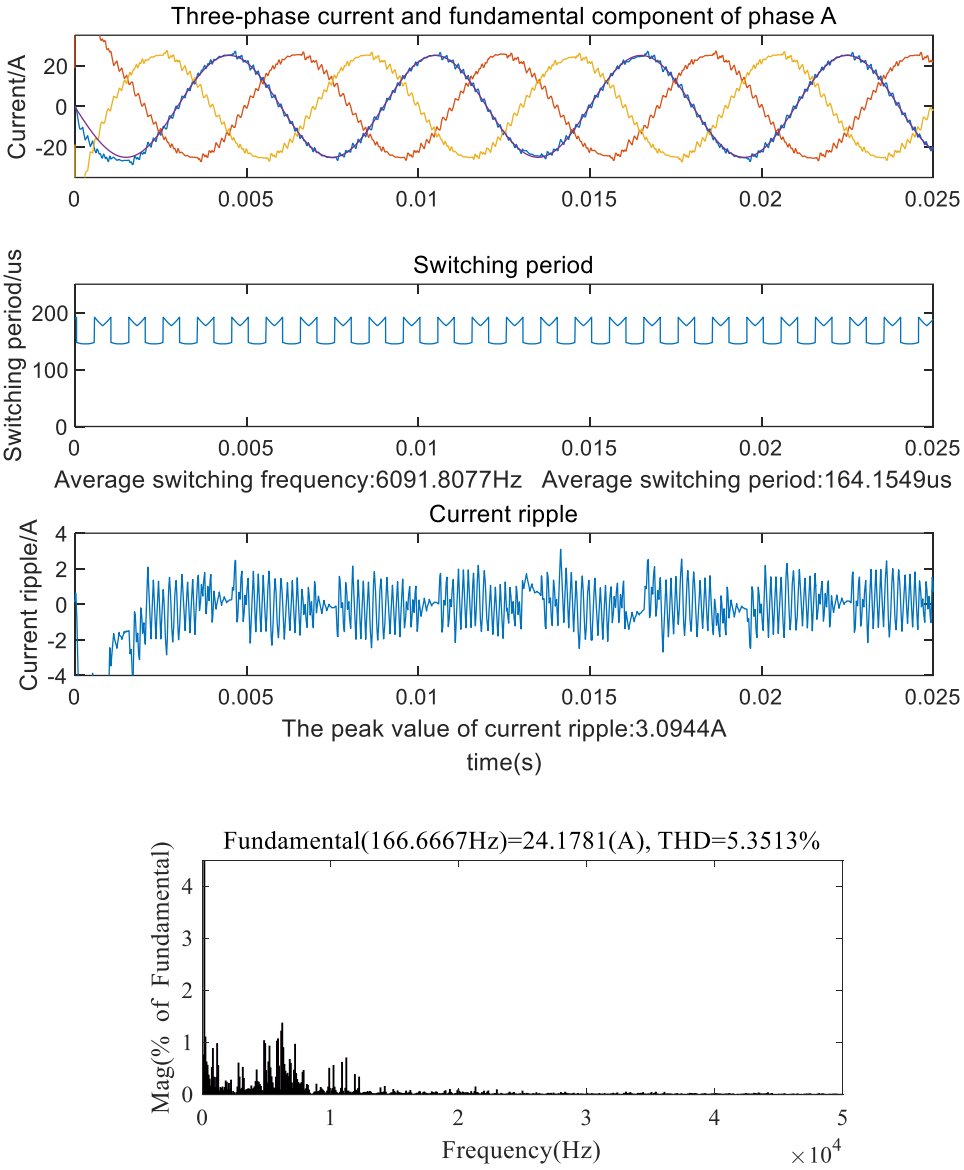


Figure 5.23 Three-phase current, A-phase fundamental current, switching period, A-phase current ripple, and A-phase current spectrum for AZSPWM/NSPWM hybrid modulation with variable switching frequency according to RMS value of flux linkage considering both cross-saturation and slotting effects.

By changing the switching frequency based on the voltage magnitude and angle, periodic variations in the switching frequency can be observed, i.e., six fluctuations of switching frequency per switching cycle. This variable switching frequency method leads to current ripple and harmonics closer to those from the fixed switching frequency method shown in Figure 5.22. It produces a more dispersed spectrum and lower peak ripple with the same average switching frequency. However, due to the saturation effect of the iron core, current ripple and harmonic distortion are increased unavoidably, compared to the simulation result of the unsaturated model in Figure 5.16.

*C. AZSPWM/NSPWM hybrid modulation considering cross-saturation of PMSM*

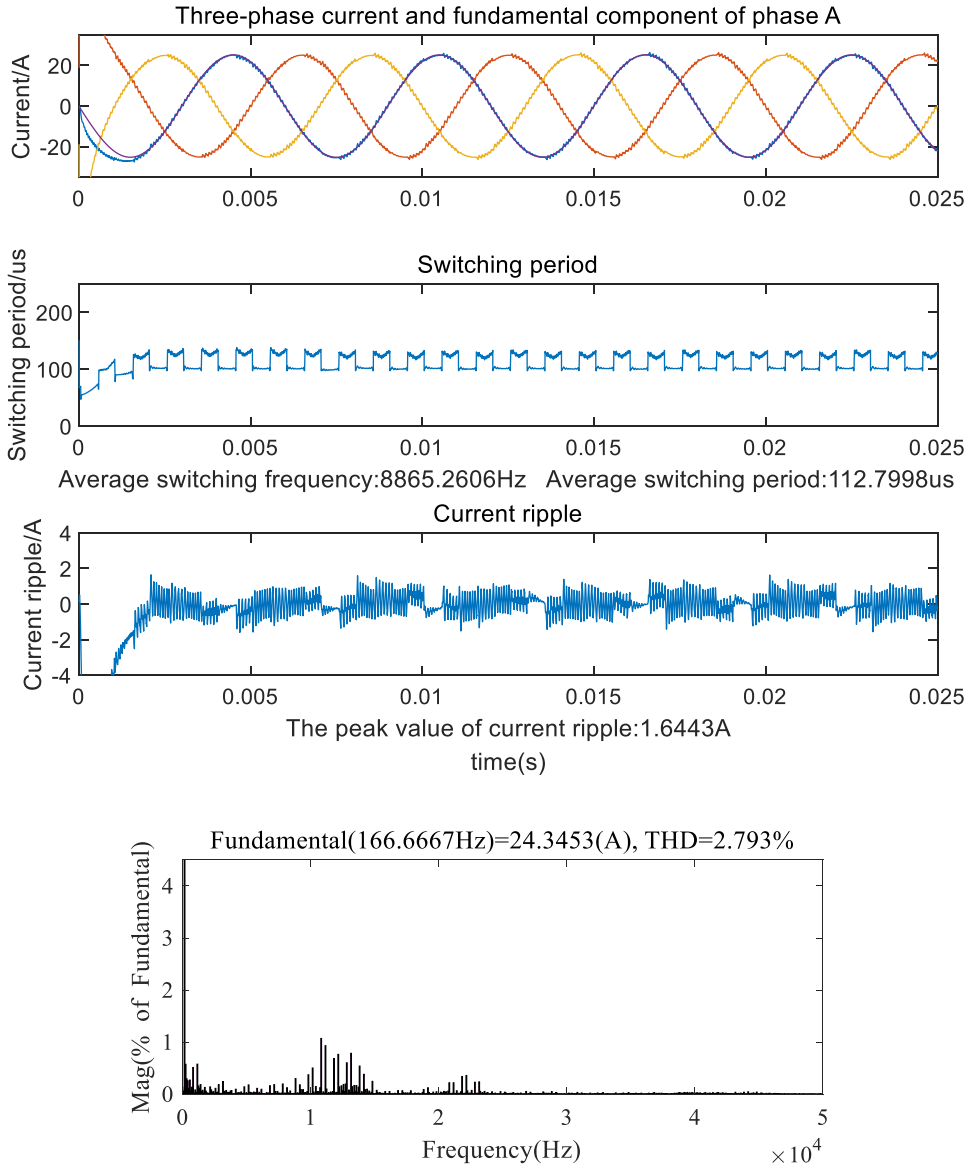


Figure 5.24 Three-phase current, A-phase fundamental current, switching period, A-phase current ripple, and A-phase current spectrum for AZSPWM/NSPWM hybrid modulation with variable switching frequency according to inductance table considering both cross-saturation and slotting effects.

By using the queried voltage harmonic spectral table and motor cross-saturation inductance table based on the voltage magnitude and angle, the simulation results for the given switching period $T_{s2\prime\prime}(M_i, \alpha, i_d, i_q)$ calculated by (5.26) are as shown in the above figure. Compared with Figure 5.23 without using the inductance table, the switching frequency is about 1.5 times higher than that with using the inductance table. This increase in switching frequency has resulted in significant reductions in ripple and harmonics. The harmonics are slightly higher than the simulation result of hybrid modulation with variable switching frequency based on the small-signal model in Section 5.3.1.2.C.Additionally, the spectrum is dispersed and moves towards higher frequency.

*D. AZSPWM/NSPWM hybrid modulation considering cross-saturation and slotting effect of PMSM*

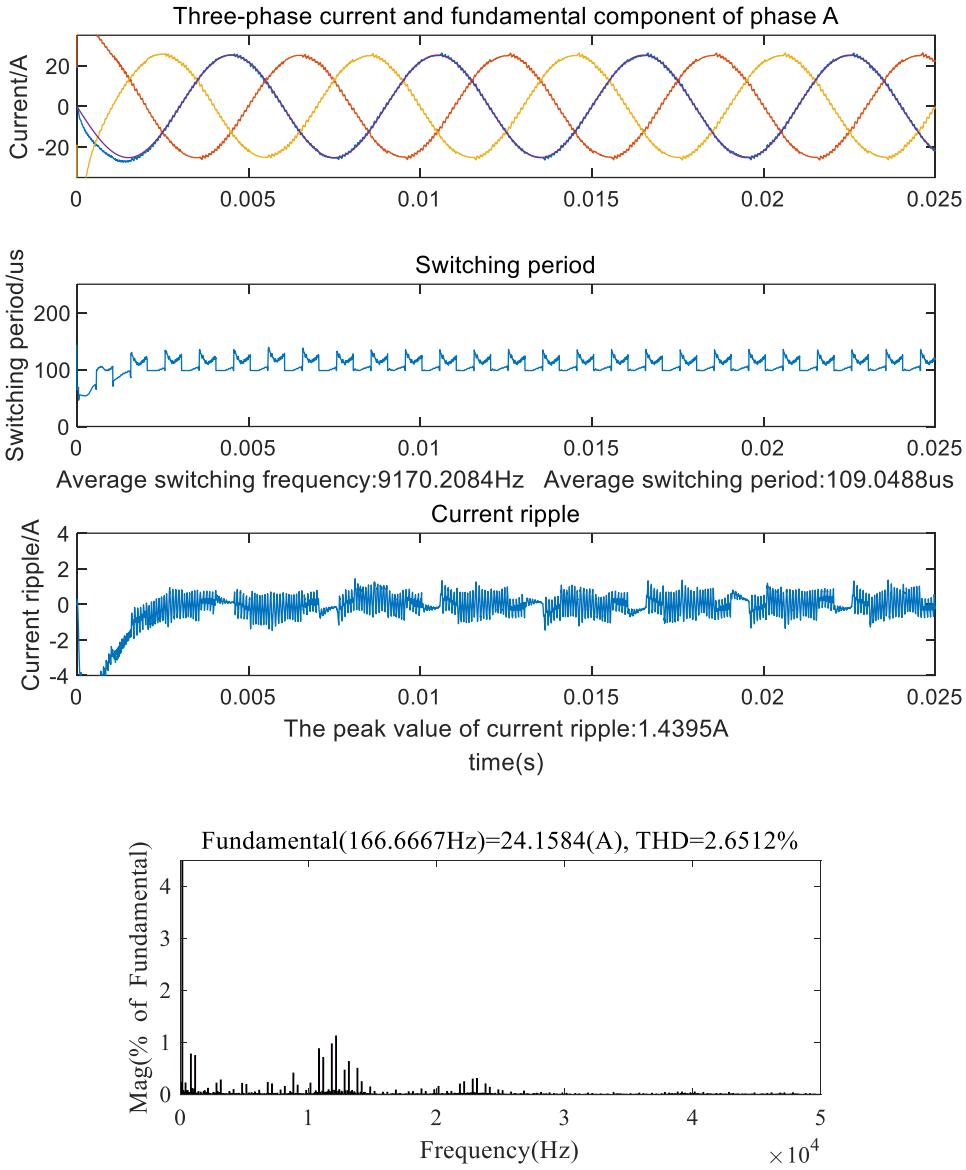


Figure 5.25 Three-phase current, A-phase fundamental current, switching period, A-phase current ripple, and A-phase current spectrum for AZSPWM/NSPWM hybrid modulation with variable switching frequency according to inductance table considering cross-saturation and slotting effect.

Through referencing the voltage harmonic spectrum table and the inductance table considering cross-saturation and slot, the switching period $T_{s2}$,$\left(M_i, \alpha, i_d, i_q, \theta\right)$ is calculated using (5.24). The modulation of the switching frequency is performed with consideration of the slot effect, resulting in the introduction of higher frequency components and an increase in the average switching frequency. Compensating for the inductance variation caused by the slot also leads to a slight reduction in harmonic and current ripple. Additionally, the harmonic and ripple of current are reduced compared to that considering only the cross-saturation effect. The result is similar to that using hybrid modulation with variable frequency on the small-signal model in Section 5.3.1.2.C.

## 5.4 EXPERIMENTAL RESULT

### 5.4.1 Experiment Platform

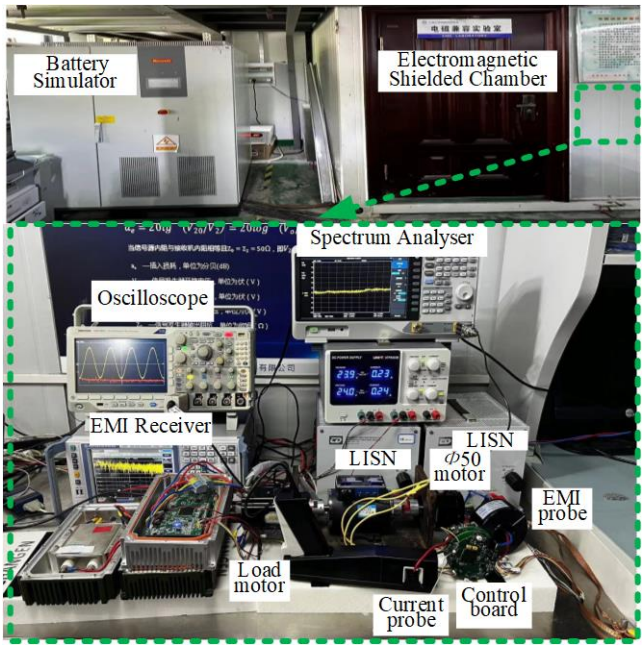


Figure 5.26 Experiment platform.

The experimentation was carried out in an electromagnetic shielded chamber. Outside the chamber, the DC bus power was provided by a battery simulator connected via two Line Impedance Stabilization Networks (LISNs). The equipment models employed are EVS-150-800, MDO3024, SVA1015X, R&S ESRP, MYCP01, TCP0150, and LNM-100, as shown in Figure 5.26. The experimental conditions were set to match the simulation conditions, and tests were conducted using a high-power density motor.

### 5.4.2 SVPWM Experimental Results

For SVPWM, tests were conducted under two scenarios: fixed switching frequency and variable switching frequency based on flux linkage ripple. Figure 5.27 shows the A-phase current and FFT analysis results. The results indicate that using a variable switching frequency can distribute the SVPWM harmonics at multiples of the switching frequency, reducing the harmonic peak by approximately 7%.

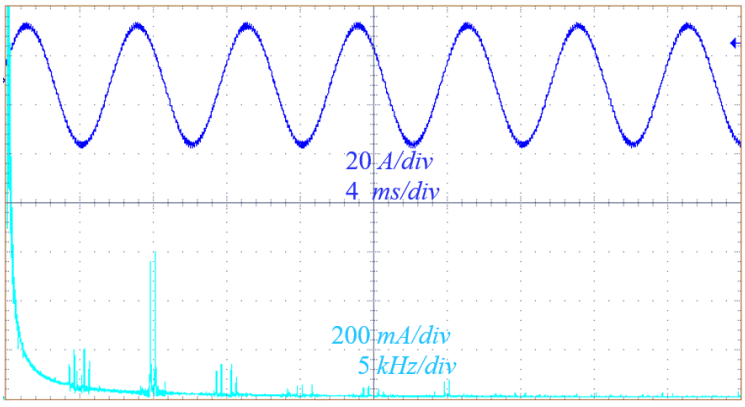


(a) Constant switching frequency.

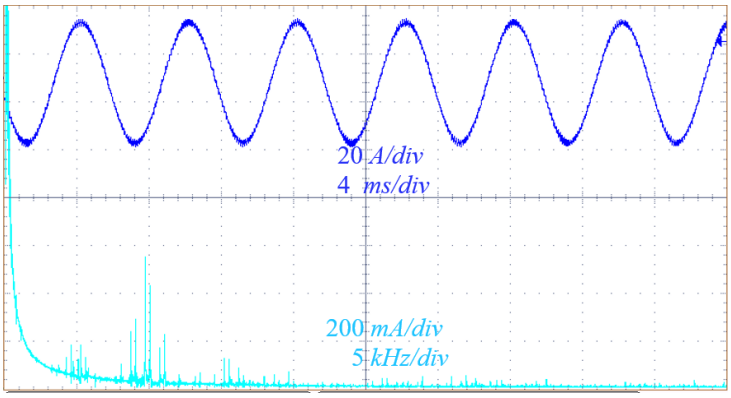


(b) Switching frequency variation based on the RMS value of flux linkage ripple.

Figure 5.27 A-phase current and spectrum of SVPWM modulation.

### 5.4.3 Hybrid Modulation Experimental Results

The experiments were conducted with four types of AZSPWM/NSPWM hybrid modulation algorithms: constant equivalent switching frequency, switching frequency variation based on the RMS value of flux linkage ripple, switching frequency variation considering cross-saturation inductance, and switching frequency variation considering slotting effects. Figure 5.28 shows the A-phase current and FFT analysis results.

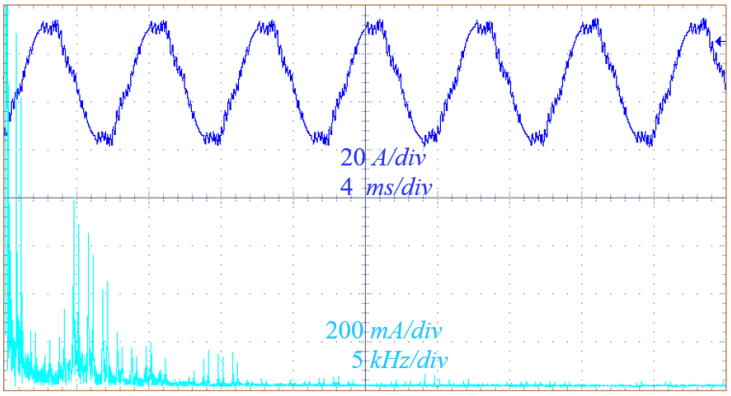


(a) Constant equivalent switching frequency.

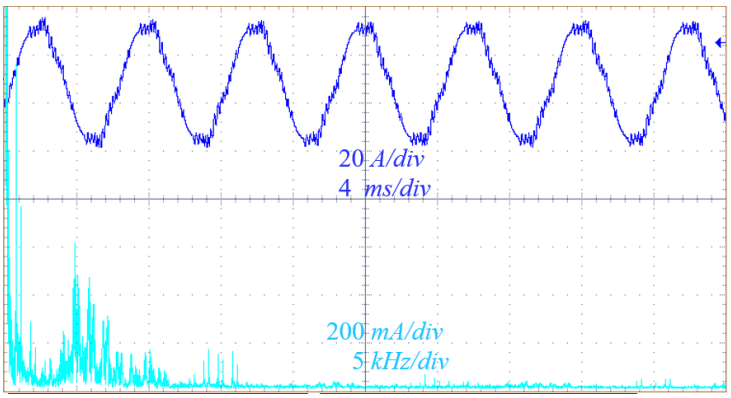


(b) Switching frequency variation based on the RMS value of flux linkage ripple.

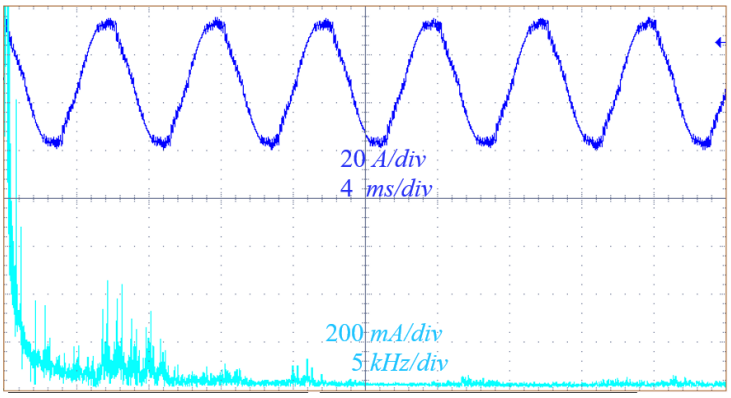


(c) Switching frequency variation considering cross-saturation.

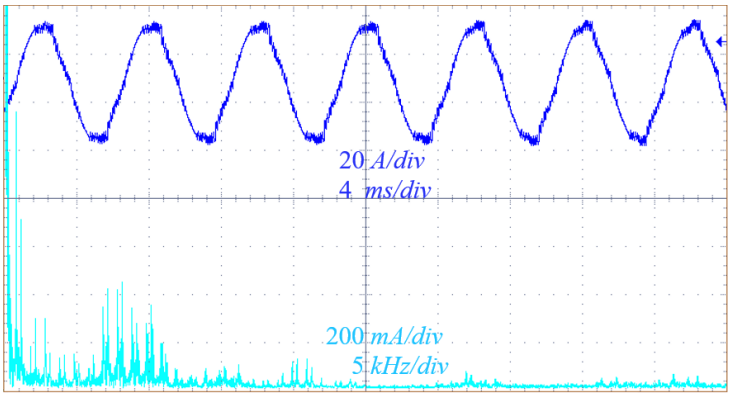


(d) Switching frequency variation considering slotting effects.

Figure 5.28 A-phase current and spectrum of AZSPWM/NSPWM hybrid modulation.

The experimental results show that, under the same number of switching events, AZSPWM/NSPWM modulation produces more harmonic content compared to modulation methods using zero vectors. However, the AZSPWM/NSPWM modulation method demonstrates certain spectrum spreading effects under constant equivalent switching frequency. The method of varying the switching frequency based on the RMS value of flux linkage harmonics increases the dispersion of the spectrum and reduces harmonic peaks without increasing the switching frequency. Additionally, the switching frequency variation method considering cross-saturation inductance reduces current ripple and further broadens the spectrum. The method considering slotting effects enhances the sinusoidal quality of the current.

### 5.4.4 Comparison of Experimental Results

Figure 5.29 presents a comparison of low-frequency current harmonics for different modulation methods. It can be observed that the method of varying the switching frequency based on the RMS value of flux linkage harmonics has limited effectiveness in improving low-frequency harmonics.

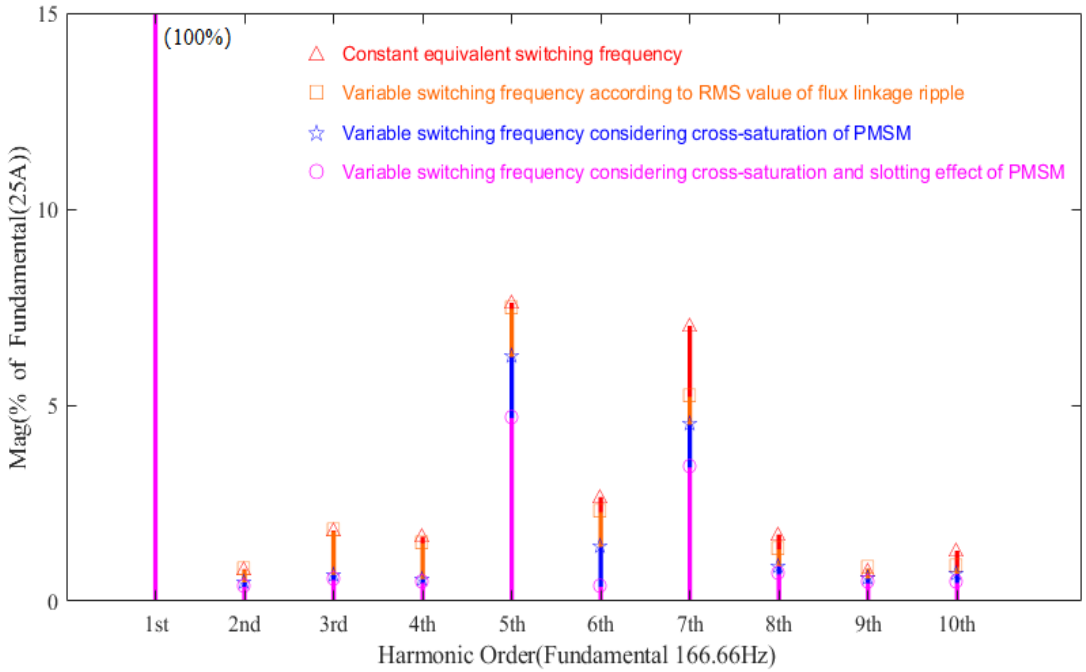


Figure 5.29 Low-order current harmonic comparison of AZSPWM/NSPWM hybrid modulation.

However, the switching frequency variation methods that consider cross-saturation and slotting effects significantly improve low-order harmonics. Notably, the method considering slotting effects shows marked improvement in the sixth harmonic around 1000 Hz, corresponding to the six instances of inductance fluctuation per electrical cycle (6 ms) caused by slotting in the finite element simulation of the designed motor.

Figure 5.30 presents the conducted emission EMI currents for different modulation methods. As the experimental results show, within the frequency range of 10–150 kHz, the application of hybrid PWM—combining AZSPWM and NSPWM—with variable switching frequencies considering slotting effects, as well as fixed equivalent switching frequencies, leads to EMI peak reductions of approximately 15 dB and 10 dB, respectively, compared to the traditional constant switching frequency SVPWM. This improvement is primarily attributed to the use of active vectors in place of zero vectors, which reduces the CMV amplitude by about 66%. Additionally, simulation results indicate that across the entire frequency range, the variable switching frequency method considering slotting effects alone can reduce conducted EMI currents by approximately 3 dB, while the hybrid AZSPWM/NSPWM modulation achieves around 9 dB reduction due to the aforementioned CMV suppression. However, beyond 150 kHz, the effectiveness of EMI suppression becomes less pronounced.

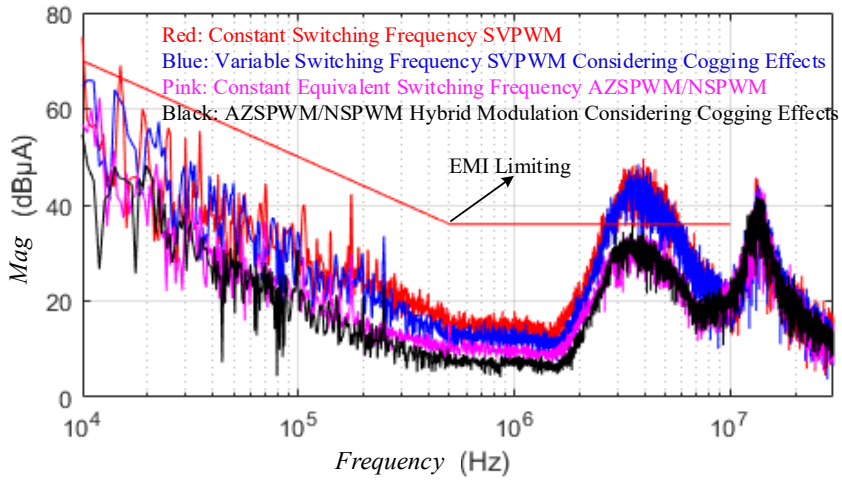


Figure 5.30 Conducted emission EMI currents of different modulation methods.

## 5.5 SUMMARY

This study proposes a novel programmed hybrid spreading spectrum modulation method for three-phase two-level VSI to mitigate EMI emission. The proposed method employs offline look-up tables to acquire switching frequency, which enables the extension of EMI current to a wideband spectrum while maintaining the current ripple unaltered. This approach takes into account the motor's saturation and slotting effects and is applicable to the control of synchronous reluctance machines, surface permanent magnet synchronous machines, and induction machines. The simulation and experiment are carried out on a deeply saturated surface permanent magnet synchronous machine. It has been found that the proposed method has the advantages of low computational complexity and a good harmonic averaging effect, and it can significantly reduce the peak value of EMI current.

# Chapter 6: Conclusions and Future Work

## 6.1 CONCLUSIONS

To meet the demands for miniaturization and light weighting of high-speed, high-overload electric drive systems, this study establishes a nonlinear motor model considering saturation and slotting effects and proposes a high-frequency motor model that accounts for skin effects. Based on these precise models, voltage modulation and current control algorithms suitable for high-overload PMSMs are developed. The main contributions and work are summarized as follows:

(1) Addressing the nonlinear challenges of high-speed, high-overload motors, this paper thoroughly analyzes the preconditions for the validity of the average linear model of PMSMs and examines the impact of core saturation and stator slotting on motor performance. A nonlinear model incorporating cross-saturation and slotting effects is derived. Using finite element simulation data, a nonlinear motor model was built in Simulink, and its accuracy was validated using measurement data from a high-overload PMSM, laying a solid foundation for subsequent research.

(2) To address the issue of high power density electromagnetic interference, this study proposes a high-frequency motor model based on external characteristics, considering the impact of skin effects on high-frequency impedance. This model accurately captures the second resonance point of impedance and is suitable for both frequency-domain and time-domain simulations. Additionally, a full-system high-frequency model incorporating the controller and cables was constructed, enabling an EMC forward design tool based on Simulink/SIwave/Simplorer joint simulation is mentioned. The tool successfully predicts common-mode conduction currents, providing effective support for validating hybrid spread spectrum modulation algorithms.

(3) For the saturation-induced saliency effects in high-overload conditions, a simplification method is proposed to globally linearize the motor model using current-flux mapping, reducing the asymmetric salient-pole motor model to a dq-axis symmetric complex vector model. To address incomplete decoupling at high speeds, a delay compensation element was introduced. Furthermore, a discrete complex vector controller based on flux data was designed by solving state-space equations, avoiding errors caused by discretizing transfer functions in the frequency domain. Experimental validation on a high-overload motor showed that the proposed controller outperforms a proportional-integral controller with an internal model, achieving higher bandwidth and decoupling performance. It expanded the stable peak current output range under high-speed conditions, increasing the stable peak output power by 39%.

(4) In the synchronous rotating reference frame with specified voltage orientation, this study derives and simplifies the voltage error vector expressions for SVPWM, DPWM, AZSPWM, and NSPWM. A normalized root mean square index, $\Delta\psi_{pu}^{rms}(M_i, \alpha)$, is proposed to evaluate the flux ripple of these modulation methods. Based on this index, a modulation algorithm is developed that utilizes the control freedom of switching frequency for spread spectrum. The proposed algorithm is computationally efficient and achieves good harmonic averaging.

Experiments on the high-overload PMSM developed in the laboratory demonstrated that, compared to traditional SVPWM, the proposed algorithm reduces the THD of current by 1.36%, and for AZSPWM/NSPWM, the reduction is 6.18%.

(5) The influence of flux fluctuations on current ripple in high-overload conditions is analyzed, and a hybrid spread spectrum modulation algorithm considering cross-saturation and slotting effects is proposed. This method utilizes finite element simulation to tabulate motor inductance as a function of current and rotor position, effectively reducing computational complexity. By accounting for dq-axis inductance variations, it is applicable not only to salient-pole motors with saturation effects but also to non-salient-pole motors. Experiments on the high-overload PMSM demonstrated that, compared to traditional fixed switching frequency modulation, the AZSPWM/NSPWM hybrid modulation with switching frequency adjustments based on cross-saturation and slotting effects significantly reduces the current THD by 23.93% and 34.13%, respectively. Additionally, the spread spectrum algorithm considering slotting effects reduces the peak value of EMI emission currents by 13 dB.

## 6.2 FUTURE WORK

The miniaturization and light weighting of power drive systems hold vast application potential. Against this backdrop, this study focuses on the control systems of high-speed, high-overload permanent magnet synchronous motors and proposes innovative current control and spread spectrum modulation algorithms. Supported by the motors and controllers designed and manufactured in this study, the effectiveness of the proposed control algorithms has been validated. Due to time constraints, however, there remain many areas for further in-depth research:

(1) Power drive systems involve the interaction of multiple physical fields, including electric, magnetic, thermal, and stress fields. This study examines the impact of magnetic saturation on motor performance and establishes a PMSM model based on finite element simulation results that consider cross-saturation and slotting effects. However, the current research does not account for the influence of thermal fields on parameters such as motor resistance, inductance, and permanent magnet flux linkage. Future research should focus on observing and measuring motor temperature and integrating this thermal information into the control system to further enhance system performance.

(2) In studying current loop control algorithms for high-overload motors, the verification scheme sets the d-axis current to -0.2 times the q-axis current. While this validates the effectiveness of the proposed discrete complex vector controller based on flux linkage data, it does not achieve torque output with minimal copper losses. To ensure the long-term operation of high-overload motors, current allocation should follow the maximum torque per ampere principle. Traditional MTPA control treats motor parameters as constants, which can result in significant errors when applied to high-overload motors. Compared to online optimization algorithms such as minimum current search and signal injection, MTPA algorithms based on nonlinear motor models have lower computational costs and faster convergence, making them a promising avenue for further research to improve the power density of electric drive systems.

(3) This study proposes an improved pulse-width modulation algorithm aimed at mitigating electromagnetic interference in the medium- and low-frequency ranges without increasing hardware costs or sacrificing low-frequency current harmonics. The algorithm has been experimentally validated on an embedded hardware platform. Experimental results demonstrate that this spread spectrum method reduces the concentration of harmonic frequencies and effectively redistributes harmonic energy in the frequency domain. In the 10 kHz to 12 MHz range, it reduces the EMI amplitude caused by PWM modulation. Further research should investigate the quantitative relationship between EMI test results at specific frequencies and the harmonic dispersion of switching frequencies to better reveal the coupling mechanism between EMI spectra and switching frequencies. This could provide more direct value to electromagnetic compatibility engineering practices.

(4) In this study, a flux linkage–current lookup table is constructed to transform the nonlinear and strongly coupled model of a synchronous machine into a single-input single-output representation. Based on this simplified model, a current controller is designed using classical control theory. However, the accuracy of torque control is affected by the errors inherent in the offline lookup table. Future work will explore the application of adaptive control strategies or modern control methods based on artificial intelligence to enhance the dynamic performance of current regulation and improve torque control accuracy. Moreover, although the theoretical analysis indicates that the proposed current control approach is also applicable to synchronous reluctance machines, no simulation or experimental validation has been conducted in this regard. Subsequent research will aim to evaluate the effectiveness of the proposed method for SynRM control to broaden its applicability.

# Bibliography


[1] Hori Y. Future Vehicle Driven by Electricity and Control[J]. IEEE Transactions on Industrial Electronics, 2004,51(5):954-962.

[2] Pusca R, Ait-Amirat Y, Berthon A, et al. Fuzzy-logic-based control applied to a hybrid electric vehicle with four separate wheel drives[J]. IEE Proceedings-Control Theory and Applications, 2004, 151(1):73-81.

[3] Vehicle body stable control method, system and automobile：CN201510516313.7 [P]. 2019-06-07.

[4] Cui J L, Wu A B, Zhou H Z,et al. Distributed Torque Distribution Control Method, System, and Vehicle for Four-Wheel-Drive Electric Vehicles：CN201910803286.X[P] 2019-12-24.

[5] Lv R L. Annual Development Research Report on Civil Unmanned Aerial Vehicles[M]. China Civil Aviation Publishing House,2020.

[6] Chen Yang. Research on Fault-tolerant Flight Control of Hexa-copters[D]. Nanjing University of Aeronautics and Astronautics,2014

[7] Xinhua News Agency. Scientific research team successfully cracks the problem of multi-rotor unmanned aerial vehicles losing control during flight. [EB/OL]. (2024.01.16)[2024.01.16].http://www.news.cn/tech/20240116/437c4abac29d4fb7b76215ce9ffa5cc1/c.html.

[8] Ke C, Cai K Y, Quan Q. Uniform passive fault-tolerant control of a quadcopter with one, two, or three rotor failure[J]. IEEE Transactions on Robotics, 39[2024-03-08].

[9] Li L, Chen Z, Hong R, et al. Research Status and Development Trend of Lower-Limb Squat-Assistant Wearable Devices[J]. Biomimetics, 2025, 10(5): 258.

[10] Zhou X H. In-depth Research on the Robotics Industry [EB/OL].(2022-08-19) [2024-03-01]. https://pdf.dfcfw.com/pdf/H3_AP202208181577346167_1.pdf.

[11] Cheng Bing, Qiu Shiliang. "Examining the Development of the Humanoid Robot Industry through CyberOne: Major Advancements in the Industrial Chain"[EB/OL](2022-08-14) [2024-03-01] https://pdf.dfcfw.com/pdf/H3_AP202208241577559671_1.pdf.

[12] Chen S K. Motor design. [M]. China Machine Press,1982.

[13] Liao J, Chen Q, Xu G, et al. Back EMF Harmonics Suppression of a Rotor Permanent Magnet Flux-Switching Motor Through Air-gap Harmonic Design[J]. IEEE Transactions on Industry Applications, 2025.

[14] Fan T, Li Q, Wen X. Development of a high power density motor made of amorphous alloy cores[J]. IEEE Transactions on Industrial Electronics, 2013, 61(9): 4510-4518.

[15] Van der Geest M, Polinder H, Ferreira J A, et al. Power density limits and design trends of high-speed permanent magnet synchronous machines[J]. IEEE Transactions on Transportation Electrification, 2015, 1(3): 266-276.

[16] Li Y., Wu J.-X., Ma P.-C., et al. Analysis of power density and prospects of future technology requirement of permanent magnet motors used in aircrafts [J]. Dianji yu Kongzhi Xuebao/Electric Machines and Control, 2022, 26(2): 1-9.

[17] Hoffmann, N.; Fuchs, F.W.; Kazmierkowski, M.P.; Schröder, D. Digital current control in a rotating reference frame-Part I: System modeling and the discrete time-domain current controller with improved decoupling capabilities. IEEE Transactions on Power Electron. 2015, 31, 5290–5305.

[18] Weihua, W.; Xi, X. An improved pi regulator for current loop of PMSM taking one-step-delay into consideration. Proc. CSEE 2014, 34, 1882–1888.

[19] Guo J, Fan T, Li Q, et al. Coupling and digital control delays affected stability analysis of permanent magnet synchronous motor current loop control[C]//2019 IEEE Vehicle Power and Propulsion Conference (VPPC). IEEE, 2019: 1-5.

[20] Rovere, L.; Formentini, A.; Zanchetta, P. FPGA implementation of a novel oversampling deadbeat controller for PMSM drives. IEEE Transactions on Industrial Electronics 2018, 66, 3731–3741.

[21] Y. Lu, J. Huang, Z. Jiang, T. Tang, H. Tang and L. Shi, PID Adaptive Feedback Motor System Based on Neural Network, in IEEE Access, vol. 12, pp. 60149-60154, 2024

[22] S. -H. Chang, P. -Y. Chen and H. -C. Kao, "Robust current control for PMSMs using sliding mode control with uncertainties estimation," 2010 IEEE International Conference on Industrial Technology, Via del Mar, Chile, 2010, pp. 117-122

[23] Z. Li, F. Wang, D. Ke, J. Li and W. Zhang, "Robust Continuous Model Predictive Speed and Current Control for PMSM With Adaptive Integral Sliding-Mode Approach," in IEEE Transactions on Power Electronics, vol. 36, no. 12, pp. 14398-14408, Dec. 2021

[24] Li S, Won H, Fu X, et al. Neural-network vector controller for permanent-magnet synchronous motor drives: Simulated and hardware-validated results[J]. IEEE transactions on cybernetics, 2019, 50(7): 3218-3230.

[25] Zhang K, Wang K W, Chung H S H. High-Attenuation wideband active common-mode EMI filter section[J]. IEEE Transactions on Power Electronics, 2021, 37(5): 5479-5490.

[26] Mainali K, Oruganti R. Conducted EMI mitigation techniques for switch-mode power converters: a survey[J]. IEEE Transactions on Power Electronics, 2010, 25(9): 2344-2356.

[27] Zheng Z, Weihua S, Borong H. Chances and challenges of photovoltaic inverters with silicon carbide devices[J]. Proceedings of the CSEE, 2017, 37(1): 221-232.

[28] Christopoulos, Christos. Principles and techniques of electromagnetic compatibility. CRC press, 2022.

[29] Paul C R, Scully R C, Steffka M A. Introduction to electromagnetic compatibility[M]. John Wiley & Sons, 2022.

[30] Jiang D, Shen Z, Li Q, et al. Advanced pulse-width-modulation: with freedom to optimize power electronics converters[M]. Springer Nature, 2021.

[31] Zhang W, Zhang Z, Wen L, et al. Multi-Gain Online Autotuning technique-based discrete-time current regulator for permanent magnet synchronous motors[J]. IEEE Transactions on Power Electronics, 2023.

[32] Liu J, Zhang Y. Current pulsation suppression method based on power current closed-loop control for a PMSM under fluctuating DC-link voltage[J]. IEEE Transactions on Power Electronics, 2021, 37(1): 761-770.

[33] Zhuang Y, Du Q, Huang W, et al. Model predictive current control for PMSM drives with calculation delay compensation[C]//2022 IEEE 5th International Electrical and Energy Conference. IEEE, 2022: 2687-2692.

[34] Chen Z, Fang H, Wu D, et al. Deadbeat current predictive control for PMSM drives based on a single FPGA with digital implementation optimization[C]//2021 IEEE International Conference on Predictive Control of Electrical Drives and Power Electronics. IEEE, 2021: 686-691.

[35] Young, H.A.; Perez, M.A.; Rodriguez, J. Analysis of finite-control-set model predictive current control with model parameter mismatch in a three-phase inverter. IEEE Transactions on Industrial Electronics 2016, 63, 3100–3107.

[36] Gonçalves, P.; Cruz, S.; Mendes, A. Finite control set model predictive control of six-phase asymmetrical machines—An overview. Energies 2019, 12, 4693.

[37] Li S, Wang H, Yang C, et al. Current decoupling control of permanent magnet synchronous motor based on improved nonlinear extended state observer[J]. Journal of Vibration and Control, 2024, 30(23-24): 5401-5417.

[38] Kiyota, K.; Kakishima, T.; Sugimoto, H.; Chiba, A. Comparison of the test result and 3D-FEM analysis at the knee point of a 60 kW SRM for a HEV. IEEE Transactions on Magnetics 2013, 49, 2291–2294.

[39] Astrom K J. Adaptive control around 1960[J]. IEEE Control Systems Magazine, 1996, 16(3): 44-49.

[40] Jung, J.W.; Leu, V.Q.; Do, T.D.; Kim, E.K.; Choi, H.H. Adaptive PID speed control design for permanent magnet synchronous motor drives. IEEE Transactions on Power Electron. 2014, 30, 900–908.

[41] Jung J W, Choi Y S, Leu V Q, et al. Fuzzy PI-type current controllers for permanent magnet synchronous motors[J]. IET electric power applications, 2011, 5(1): 143-152.

[42] Chang S H, Chen P Y, Ting Y H, et al. Robust current control-based sliding mode control with simple uncertainties estimation in permanent magnet synchronous motor drive systems[J]. IET Electric Power Applications, 2010, 4(6): 441-450.

[43] Liu, Jing, Hongwen Li, and Yongting Deng. "Torque ripple minimization of PMSM based on robust ILC via adaptive sliding mode control." IEEE Transactions on Power Electronics 33.4 (2017): 3655-3671.

[44] Xia, C.; Yan, Y.; Song, P.; Shi, T. Voltage disturbance rejection for matrix converter-based PMSM drive system using internal model control. IEEE Transactions on Industrial Electronics 2011, 59, 361–372.

[45] Fu, X.; He, H.; Xu, Y.; Fu, X. A Strongly Robust and easy-tuned current controller for PMSM considering parameters variation. IEEE Access 2020, 8, 44228–44238.

[46] Economou C G, Morari M, Palsson B O. Internal model control: Extension to nonlinear system[J]. Industrial & Engineering Chemistry Process Design and Development, 1986, 25(2): 403-411.

[47] Zhong, Z.F.; Jin, M.J.; Shen, J.X. Full speed range sensorless control of permanent magnet synchronous motor with phased PI regulator-based model reference adaptive system. Proc. CSEE 2018, 38, 1203–1211.

[48] Novotny, D.W.; Lipo, T.A. Vector control and dynamics of AC drives; oxford university press: New York, NY, USA, 1996.

[49] Yuan, X.; Chen, J.; Jiang, C.; Lee, C.H. Discrete-time current regulator for AC machine drives. IEEE Transactions on Power Electron. 2021, 37, 5847–5858.

[50] Awan HA, A.; Saarakkala, S.E.; Hinkkanen, M. Flux-linkage-based current control of saturated synchronous motors. IEEE Transactions on On Industry Applications 2019, 55, 4762–4769.

[51] Kim, H.; Degner, M.W.; Guerrero, J.M.; Briz, F.; Lorenz, R.D. Discrete-time current regulator design for AC machine drives. IEEE Transactions on On Industry Applications 2010, 46, 1425–1435.

[52] Yang X, Yuan Y, Zhang X, et al. Shaping high-power IGBT switching transitions by active voltage control for reduced EMI generation[J]. IEEE Transactions on Industry Applications, 2014, 51(2): 1669-1677.

[53] Boone T G. Software as a tool for controlling EMI/EMC[C]//IEEE 1991 International Symposium on Electromagnetic Compatibility. IEEE, 1991: 198-199.

[54] Zhang P, Wang S, Li Y. Performance and Analysis of N-State Random Pulse Position SVPWM With Constant Sampling Frequency[J]. IEEE Transactions on Power Electronics, 2022, 37(11): 13606-13625.

[55] Deng W, Huang J, Qian Z, et al. A random pulse position-based selective noise cancellation modulation method for SVPWM driven PMSMs[J]. IEEE Transactions on Energy Conversion, 2022, 37(3): 2190-2198.

[56] Bhattacharya S, Mascarella D, Joos G, et al. Reduced switching random PWM technique for two-level inverters[C]//2015 IEEE Energy Conversion Congress and Exposition. IEEE, 2015: 695-702.

[57] Gamoudi R, Chariag D E, Sbita L. A review of spread-spectrum-based PWM techniques—A novel fast digital implementation[J]. IEEE Transactions on Power Electronics, 2018, 33(12): 10292-10307.

[58] Trzynadlowski A M, Legowski S, Lynn Kirlin R. Random pulse-width modulation technique for voltage-controlled power inverters[J]. International Journal of Electronics Theoretical and Experimental, 1990, 68(6): 1027-1037.

[59] Sadhu N L, Teegala B R, Marapu V K. Constant and variable switching frequency random PWM strategies for open-end winding induction motor drive[J]. Journal of Power Electronics, 2020, 20: 1488-1495.

[60] Xu Y, Yuan Q, Zou J, et al. Sinusoidal periodic carrier frequency modulation in reducing electromagnetic noise of permanent magnet synchronous motor[J]. IET Electric Power Applications, 2013, 7(3): 223-230.

[61] Huang Y, Xu Y, Zhang W, et al. Hybrid periodic carrier frequency modulation technique based on modified SVPWM to reduce the PWM noise[J]. IET Power Electronics, 2019, 12(3): 515-520.

[62] Natarajan S, Padmavathi P, Kalvakurthi J R, et al. Conducted electromagnetic interference spectral peak mitigation in LUO-converter using FPGA-based chaotic PWM technique[J]. Electric Power Components and Systems, 2019, 47(9-10): 838-848.

[63] Kim J H, Jung Y G. Spreading power spectrum of an induction motor drive system by chaotic pulse width modulation method[J]. Journal of Electrical Engineering & Technology, 2021, 16(5): 2685-2694.

[64] Chiasson J N, Du Z, Özpineci B, et al. High dynamic performance programmed PWM control of a multilevel inverter with capacitor DC sources[C]//Proceedings of the 48h IEEE Conference on Decision and Control held jointly with 2009 28th Chinese Control Conference. IEEE, 2009: 6561-6568.

[65] Wilson B, Diong B, Kalaria C, et al. Programmed PWM of symmetric and asymmetric multilevel inverters for minimal output distortion[C]//SoutheastCon 2022. IEEE, 2022: 501-506.

[66] Jiang D, Wang F. Current-ripple prediction for three-phase PWM converters[J]. IEEE Transactions on Industry Applications, 2013, 50(1): 531-538.

[67] Jiang D, Li Q, Han X, et al. Variable switching frequency PWM for torque ripple control of AC motors[C]//2016 19th International Conference on Electrical Machines and Systems. IEEE, 2016: 1-5.

[68] Yang F, Taylor A R, Bai H, et al. Using d–q transformation to vary the switching frequency for interior permanent magnet synchronous motor drive systems[J]. IEEE Transactions on Transportation Electrification, 2015, 1(3): 277-286.

[69] Li Q, Jiang D, Zhang Y. Analysis and calculation of current ripple considering inductance saturation and its application to variable switching frequency PWM[J]. IEEE Transactions on Power Electronics, 2019, 34(12): 12262-12273.

[70] Li Q, Jiang D, Zhang Y, et al. The impact of VSFPWM on DQ current control and a compensation method[J]. IEEE Transactions on Power Electronics, 2020, 36(3): 3563-3572.

[71] Ismail M M, Xu W, Wang X, et al. Analysis and optimization of torque ripple reduction strategy of surface-mounted permanent-magnet motors in flux-weakening region based on genetic algorithm[J]. IEEE Transactions on Industry Applications, 2021, 57(4): 4091-4106.

[72]Kumar A C B, Narayanan G. Variable-switching frequency PWM technique for induction motor drive to spread acoustic noise spectrum with reduced current ripple[J]. IEEE Transactions on Industry Applications, 2016, 52(5): 3927-3938.

[73] Chang L, Jahns T M. Prediction and evaluation of PWM-induced current ripple in IPM machines incorporating slotting, saturation, and cross-coupling effects[C]//2017 20th International Conference on Electrical Machines and Systems . IEEE, 2017: 1-6.

[74] Chang L, Jahns T M. Prediction and evaluation of PWM-induced current ripple in IPM machines incorporating slotting, saturation, and cross-coupling effects[J]. IEEE Transactions on Industry Applications, 2018, 54(6): 6015-6026.

[75] Narayanan G, Zhao D, Krishnamurthy H K, et al. Space vector based hybrid PWM techniques for reduced current ripple[J]. IEEE Transactions on Industrial Electronics, 2008, 55(4): 1614-1627.

[76] Ibrahim A, Sujod M Z. Variable switching frequency hybrid PWM technique for switching loss reduction in a three-phase two-level voltage source inverter[J]. Measurement, 2020, 151: 107192.

[77] Bhattacharya S, Sharma S K, Mascarella D, et al. Subfundamental cycle switching frequency variation based on output current ripple analysis of a three-level inverter[J]. IEEE Journal of Emerging and Selected Topics in Power Electronics, 2017, 5(4): 1797-1806.

[78] Bhattacharya S, Sharma S K, Mascarella D, et al. Subfundamental cycle switching frequency variation for switching losses reduction of a two-level inverter traction drive[J]. IEEE Transactions on Transportation Electrification, 2017, 3(3): 646-655.

[79] Zhang J, He Y, Hang L. A Novel Interleaved Parallel Cascaded Three-Level PFC With Low Inductance Volt-Second and Low Common-Mode Noise[J]. IEEE Transactions on Power Electronics, 2022, 38(1): 17-21.

[80] Shaikh M S, Maurya R. Performance investigation on SVPWM sequences based on reduced common-mode voltage in dual three-phase asymmetrical machine[J]. IEEE Transactions on Energy Conversion, 2021, 36(4): 2884-2893.

[81] Xu L, Zhu Z Q. Novel SVPWM for Open Winding PMSM Drives with Simultaneous Common Mode Voltage Control and Full Frequency Zero Sequence Current Suppression[J]. IEEE Journal of Emerging and Selected Topics in Power Electronics, 2023.

[82] Aizawa N, Kubota H. Analysis of common-mode voltage elimination of PWM inverter with auxiliary inverter[C]//2010 International Conference on Electrical Machines and Systems. IEEE, 2010: 889-893.

[83] Aizawa N, Kikuchi M, Kubota H, et al. Dead-time effect and its compensation in common-mode voltage elimination of PWM inverter with auxiliary inverter[C]//The 2010 International Power Electronics Conference-ECCE ASIA-. IEEE, 2010: 222-227.

[84] Hava A M, Ün E. Performance analysis of reduced common-mode voltage PWM methods and comparison with standard PWM methods for three-phase voltage-source inverters[J]. IEEE Transactions on Power Electronics, 2009, 24(1): 241-252.

[85] Hava A M, Ün E. A high-performance PWM algorithm for common-mode voltage reduction in three-phase voltage source inverters[J]. IEEE Transactions on Power Electronics, 2010, 26(7): 1998-2008.

[86] Mohammed O A, Ganu S, Abed N, et al. High frequency PM synchronous motor model determined by FE analysis[J]. IEEE transactions on magnetics, 2006, 42(4): 1291-1294.

[87] Birnkammer F, Chen J, Pinhal D B, et al. Influence of the modeling depth and voltage level on the ac losses in parallel conductors of a permanent magnet synchronous machine[J]. IEEE Transactions on Applied Superconductivity, 2018, 28(3): 1-5.

[88] Taran N, Ionel D M, Rallabandi V, et al. An overview of methods and a new three-dimensional FEA and analytical hybrid technique for calculating AC winding losses in PM machines[J]. IEEE Transactions on Industry Applications, 2020, 57(1): 352-362.

[89] CISPR S C. D: CISPR 25 Vehicles, boats and internal combustion engines–Radio disturbance characteristics–Limits and methods of measurement for the protection of on-board receivers[J]. Standard, IEC, 2008.

[90] Sarrió J E R, Martis C, Chauvicourt F. Numerical computation of parasitic slot capacitances in electrical machines[C]//2020 International Conference and Exposition on Electrical And Power Engineering . IEEE, 2020: 146-150.

[91] Mirafzal B, Skibinski G L, Tallam R M, et al. Universal induction motor model with low-to-high frequency-response characteristics[J]. IEEE Transactions on Industry Applications, 2007, 43(5): 1233-1246.

[92] Li Z, Ma X, Dong K, et al. Study and discussion on the problems of shaft voltage and bearing current in wind power generation system[C]//2014 9th IEEE Conference on Industrial Electronics and Applications. IEEE, 2014: 1696-1700.

[93] Wu Y, Bi C, Jia K, et al. High-frequency modelling of permanent magnet synchronous motor with star connection[J]. IET Electric Power Applications, 2018, 12(4): 539-546.

[94] Gries M A, Mirafzal B. Permanent magnet motor-drive frequency response characterization for transient phenomena and conducted EMI analysis[C]//2008 Twenty-Third Annual IEEE Applied Power Electronics Conference and Exposition. IEEE, 2008: 1767-1775.

[95] Cai M, Craddock T, Wasynczuk O. High-frequency modeling, parameterization, and simulation of IPM motor drive systems[C]//2017 IEEE Power and Energy Conference at Illinois (PECI). IEEE, 2017: 1-8.

[96] Yang Y M, Peng H M, Wang Q D. Common model EMI prediction in motor drive system for electric vehicle application[J]. Journal of Electrical Engineering and Technology, 2015, 10(1): 205-215.

[97] Hoffmann A, Ponick B. Statistical deviation of high-frequency lumped model parameters for stator windings in three-phase electrical machines[C]//2020 International Symposium on Power Electronics, Electrical Drives, Automation and Motion (SPEEDAM). IEEE, 2020: 85-90.

[98] Weston D. Electromagnetic Compatibility: Principles and Applications, Revised and Expanded[M]. CRC Press, 2017.

[99] Wang Y, Ma J, Liu C, et al. Reduction of magnet eddy current loss in PMSM by using partial magnet segment method[J]. IEEE Transactions on Magnetics, 2019, 55(7): 1-5.

[100] Wang C Y, Xia J K, Sun Y B. Modern Electric Motor Control Technology [M]. China Machine Press, 2009.

[101] Guglielmi P, Pastorelli M, Vagati A. Cross-saturation effects in IPM motors and related impact on sensorless control[J]. IEEE Transactions on Industry Applications, 2006, 42(6): 1516-1522.

[102] Li S, Han D, Sarlioglu B. Modeling of interior permanent magnet machine considering saturation, cross coupling, spatial harmonics, and temperature effects[J]. IEEE Transactions on Transportation Electrification, 2017, 3(3): 682-693.

[103] B Mirafzal, G Skibinski, and R Tallam. Determination of parameters in the universal induction motor model[J]. IEEE Transactions on Industry Applications,2009,45(1):142-151.

[104] Suresh G, Toliyat H A, Rendusara D A, et al. Predicting the transient effects of PWM voltage waveform on the stator windings of random wound induction motors[J]. IEEE Transactions on Power Electronics, 2002, 14(1):23-30.

[105] Wang L, Ngai-Man Ho, C Canales, F Jatskevich. High-Frequency Modeling of the Long-Cable-Fed Induction Motor Drive System Using TLM Approach for Predicting Overvoltage Transients[J]. IEEE Transactions on Power Electronics, 2010, 25(10):2653-2664.

[106] Schinkel M, Weber S, Guttowski S, et al. Efficient HF modeling and model parameterization of induction machines for time and frequency domain simulations[C]. IEEE Applied Power Electronics Conference and Exposition, 2008.

[107] Toulabi M S, Wang L, Bieber L, et al. A Universal High-Frequency Induction Machine Model and Characterization Method for Arbitrary Stator Winding Connections[J]. IEEE Transactions on Energy Conversion, 2019, 34(3):1164-1177.

[108] Moreira A F, Lipo T A, Venkataramanan G, et al. High-frequency modeling for cable and induction motor overvoltage studies in long cable drives[J]. IEEE Transactions on Industry Applications, 2002, 38(5):1297-1306.

[109] Harnefors L, Nee H P. Model-based current control of AC machines using the internal model control method[J]. IEEE Transactions on Industry Applications, 1998, 34(1): 133-141.

[110] Luo G, Zhang R, Chen Z, et al. A novel nonlinear modeling method for permanent-magnet synchronous motors[J]. IEEE Transactions on Industrial Electronics, 2016, 63(10): 6490-6498.

[111] Yang S, Wang Q, Xie Z, et al. Digital current controller with a novel active damping design for IPMSM[J]. IEEE Transactions on Energy Conversion, 2021, 37(1): 185-197.

[112]Dead-Time Compensation Method for Vector-Controlled VSI Drives Based on Qorivva Family. Available online: https://www.nxp.com/docs/en/application-note/AN4863.pdf (accessed on 16th March 2022).

[113] Feng C, Wang P, Huang S, et al. A Novel Torque Harmonics Suppression PWM Method of High-Speed PMSG for Microturbine Power Generation System[J]. IEEE Transactions on Transportation Electrification, 2023, 10(3): 7275-7285.

[114] Leoncini M, Bertolini A, Melillo P, et al. Spread-Spectrum Frequency Modulation in a DC/DC Converter with Time-Based Control[J]. IEEE Transactions on Power Electronics, 2022.

[115] Chen J, Jiang D, Sun W, et al. A family of spread-spectrum modulation schemes based on distribution characteristics to reduce conducted EMI for power electronics converters[J]. IEEE Transactions on Industry Applications, 2020, 56(5): 5142-5157.

[116] Jung H S, Hwang C E, Kim H S, et al. Minimum torque ripple pulse width modulation with reduced switching frequency for medium-voltage motor drive[J]. IEEE Transactions on Industry Applications, 2018, 54(4): 3315-3325.

# Appendices

## A. Normalizing flux linkage harmonic of the single voltage vector

The DQ axis flux linkage harmonic, $\Delta\psi_x^D$ and $\Delta\psi_x^Q$, of the fundamental voltage vector x ($x = 1,2,3,4,5,6,z$) is normalized with $\Delta\psi_{base}^{DQ} = \frac{2}{3}U_{dc}T_{ss}$. The results are shown in Table A.1.

Table A.1 Normalized flux linkage harmonic on the DQ-axis

| Voltage Vector | Normalized flux linkage harmonic on the D-axis | Normalized flux linkage harmonic on the Q-axis |
|---|---|---|
| Vector 1 | $\Delta\psi_{1pu}^D = sin(\alpha)\frac{T_1}{T_{ss}}$ | $\Delta\psi_{1pu}^Q = [cos(\alpha) - M_i]\frac{T_1}{T_{ss}}$ |
| Vector 2 | $\Delta\psi_{2pu}^D = sin\left(\frac{\pi}{3} - \alpha\right)\frac{T_2}{T_{ss}}$ | $\Delta\psi_{2pu}^Q = \left[cos\left(\frac{\pi}{3} - \alpha\right) - M_i\right]\frac{T_2}{T_{ss}}$ |
| Vector 3 | $\Delta\psi_{3pu}^D = sin\left(\frac{2\pi}{3} - \alpha\right)\frac{T_3}{T_{ss}}$ | $\Delta\psi_{3pu}^Q = \left[cos\left(\frac{2\pi}{3} - \alpha\right) - M_i\right]\frac{T_3}{T_{ss}}$ |
| Vector 4 | $\Delta\psi_{4pu}^D = sin(\pi - \alpha)\frac{T_4}{T_{ss}}$ | $\Delta\psi_{4pu}^Q = [cos(\pi - \alpha) - M_i]\frac{T_4}{T_{ss}}$ |
| Vector 5 | $\Delta\psi_{5pu}^D = sin\left(\frac{4\pi}{3} - \alpha\right)\frac{T_5}{T_{ss}}$ | $\Delta\psi_{5pu}^Q = \left[cos\left(\frac{4\pi}{3} - \alpha\right) - M_i\right]\frac{T_5}{T_{ss}}$ |
| Vector 6 | $\Delta\psi_{6pu}^D = sin\left(\frac{5\pi}{3} - \alpha\right)\frac{T_6}{T_{ss}}$ | $\Delta\psi_{6pu}^Q = \left[cos\left(\frac{5\pi}{3} - \alpha\right) - M_i\right]\frac{T_6}{T_{ss}}$ |
| Vectors 0 and 7 | $\Delta\psi_{zpu}^D = 0$ | $\Delta\psi_{zpu}^Q = -M_i\frac{T_z}{T_{ss}}$ |

## B. Normalizing flux linkage harmonic of a voltage vector

The flux linkage harmonic $\Delta\psi^{rms}(M_i,\ \alpha,\ U_{dc},\ T_{ss})$ of the PWM methods are normalized with $\Delta\psi_{base}^{DQ}$, namely,

$$\Delta\psi_{pu}^{rms}(M_i,\ \alpha) = \frac{3}{2U_{dc}T_{ss}}\Delta\psi^{rms}(M_i,\ \alpha,\ U_{dc},\ T_{ss}) \quad (A.1)$$

The results are shown in Table A.2。

Table A. Normalized value of the PWM flux linkage harmonic.

| PWM Method | Normalized value of the flux linkage harmonic $\Delta\psi_{pu}^{rms}(M_i,\ \alpha)$ |
|---|---|

| | |
|---|---|
| SVPWM | $\Delta\psi_{0127pu}^{rms} = sqrt\left\{\frac{1}{3}\left(0.5\Delta\psi_{zpu}^{Q}\right)^2\frac{T_z}{2T_{ss}} + \frac{1}{3}\left[\left(0.5\Delta\psi_{zpu}^{Q}\right)^2 + 0.5\Delta\psi_{zpu}^{Q}\left(0.5\Delta\psi_{zpu}^{Q} + \Delta\psi_{1pu}^{Q}\right) + \left(0.5\Delta\psi_{zpu}^{Q} + \Delta\psi_{1pu}^{Q}\right)^2\right]\frac{T_1}{T_{ss}} + \frac{1}{3}\left[\left(0.5\Delta\psi_{zpu}^{Q} + \Delta\psi_{1pu}^{Q}\right)^2 - 0.5\Delta\psi_{zpu}^{Q}\left(0.5\Delta\psi_{zpu}^{Q} + \Delta\psi_{1pu}^{Q}\right) + \left(-0.5\Delta\psi_{zpu}^{Q}\right)^2\right]\frac{T_2}{T_{ss}} + \frac{1}{3}\left(-0.5\Delta\psi_{zpu}^{Q}\right)^2\frac{T_z}{2T_{ss}} + \frac{1}{3}\left(\Delta\psi_{1pu}^{D}\right)^2\frac{T_1+T_2}{T_{ss}}\right\}$ |
| AZSPWM | $\Delta\psi_{3216pu}^{rms} = sqrt\left\{\frac{1}{3}\left(\Delta\psi_{3pu}^{Q}\right)^2\frac{T_3}{T_{ss}} + \frac{1}{3}\left[\left(\Delta\psi_{3pu}^{Q}\right)^2 + \Delta\psi_{3pu}^{Q}\left(\Delta\psi_{3pu}^{Q} + \Delta\psi_{2pu}^{Q}\right) + \left(\Delta\psi_{3pu}^{Q} + \Delta\psi_{2pu}^{Q}\right)^2\right]\frac{T_2}{T_{ss}} + \frac{1}{3}\left[\left(\Delta\psi_{3pu}^{Q} + \Delta\psi_{2pu}^{Q}\right)^2 - \Delta\psi_{6pu}^{Q}\left(\Delta\psi_{3pu}^{Q} + \Delta\psi_{2pu}^{Q}\right) + \left(\Delta\psi_{6pu}^{Q}\right)^2\right]\frac{T_1}{T_{ss}} + \frac{1}{3}\left(\Delta\psi_{6pu}^{Q}\right)^2\frac{T_6}{T_{ss}} + \frac{1}{3}\left(\Delta\psi_{3pu}^{D}\right)^2\frac{T_3}{T_{ss}} + \frac{1}{3}\left[\left(\Delta\psi_{3pu}^{D}\right)^2 + \Delta\psi_{3pu}^{D}\left(\Delta\psi_{3pu}^{D} + \Delta\psi_{2pu}^{D}\right) + \left(\Delta\psi_{3pu}^{D} + \Delta\psi_{2pu}^{D}\right)^2\right]\frac{T_2}{T_{ss}} + \frac{1}{3}\left[\left(\Delta\psi_{3pu}^{D} + \Delta\psi_{2pu}^{D}\right)^2 - \Delta\psi_{6pu}^{D}\left(\Delta\psi_{3pu}^{D} + \Delta\psi_{2pu}^{D}\right) + \left(\Delta\psi_{6pu}^{D}\right)^2\right]\frac{T_1}{T_{ss}} + \frac{1}{3}\left(\Delta\psi_{6pu}^{D}\right)^2\frac{T_6}{T_{ss}}\right\}$ |
| DPWM012 | $\Delta\psi_{012pu}^{rms} = sqrt\left\{\frac{1}{3}\left(\Delta\psi_{zpu}^{Q}\right)^2\frac{T_z}{T_{ss}} + \frac{1}{3}\left[\left(\Delta\psi_{zpu}^{Q}\right)^2 + \Delta\psi_{zpu}^{Q}\left(\Delta\psi_{zpu}^{Q} + \Delta\psi_{1pu}^{Q}\right) + \left(\Delta\psi_{zpu}^{Q} + \Delta\psi_{1pu}^{Q}\right)^2\right]\frac{T_1}{T_{ss}} + \frac{1}{3}\left(\Delta\psi_{zpu}^{Q} + \Delta\psi_{1pu}^{Q}\right)^2\frac{T_2}{T_{ss}} + \frac{1}{3}\left(\Delta\psi_{1pu}^{D}\right)^2\frac{T_1+T_2}{T_{ss}}\right\}$ |

| | |
|---|---|
| DPWM721 | $\Delta\psi_{721pu}^{rms} = sqrt\left\{\frac{1}{3}\left(\Delta\psi_{zpu}^{Q}\right)^2\frac{T_z}{T_{ss}} + \frac{1}{3}\left[\left(\Delta\psi_{zpu}^{Q}\right)^2 + \Delta\psi_{zpu}^{Q}\left(\Delta\psi_{zpu}^{Q} + \Delta\psi_{1pu}^{Q}\right) + \left(\Delta\psi_{zpu}^{Q} + \Delta\psi_{1pu}^{Q}\right)^2\right]\frac{T_2}{T_{ss}} + \frac{1}{3}\left(\Delta\psi_{zpu}^{Q} + \Delta\psi_{1pu}^{Q}\right)^2\frac{T_1}{T_{ss}} + \frac{1}{3}\left(\Delta\psi_{1pu}^{D}\right)^2\frac{T_1+T_2}{T_{ss}}\right\}$ |
| NSPWM | $\Delta\psi_{321pu}^{rms} = sqrt\left\{\frac{1}{3}\left(\Delta\psi_{3pu}^{Q}\right)^2\frac{T_3}{T_{ss}} + \frac{1}{3}\left[\left(\Delta\psi_{3pu}^{Q}\right)^2 + \Delta\psi_{3pu}^{Q}\left(\Delta\psi_{3pu}^{Q} + \Delta\psi_{2pu}^{Q}\right) + \left(\Delta\psi_{3pu}^{Q} + \Delta\psi_{2pu}^{Q}\right)^2\right]\frac{T_2}{T_{ss}} + \frac{1}{3}\left(\Delta\psi_{3pu}^{Q} + \Delta\psi_{2pu}^{Q}\right)^2\frac{T_1}{T_{ss}} + \frac{1}{3}\left(\Delta\psi_{3pu}^{D}\right)^2\frac{T_3}{T_{ss}} + \frac{1}{3}\left[\left(\Delta\psi_{3pu}^{D}\right)^2 + \Delta\psi_{3pu}^{D}\left(\Delta\psi_{3pu}^{D} + \Delta\psi_{2pu}^{D}\right) + \left(\Delta\psi_{3pu}^{D} + \Delta\psi_{2pu}^{D}\right)^2\right]\frac{T_2}{T_{ss}} + \frac{1}{3}\left(\Delta\psi_{3pu}^{D} + \Delta\psi_{2pu}^{D}\right)^2\frac{T_1}{T_{ss}}\right\}$ |

**C. Common and Differential Mode Impedance and High-Frequency Model Parameterization Results for High Overload Motors.**

The common and differential mode impedance of the highly overloaded PMSM designed in this study was tested using an impedance analyzer HP 4294A. The test results are shown in Figure C.1, where points A to G represent key characteristic points required for model parameterization. Due to the limited accuracy of the test equipment at low frequencies, the results below 10 kHz may exhibit slight inaccuracies. Therefore, when selecting characteristic parameter points, it is advisable to avoid this frequency range as much as possible.

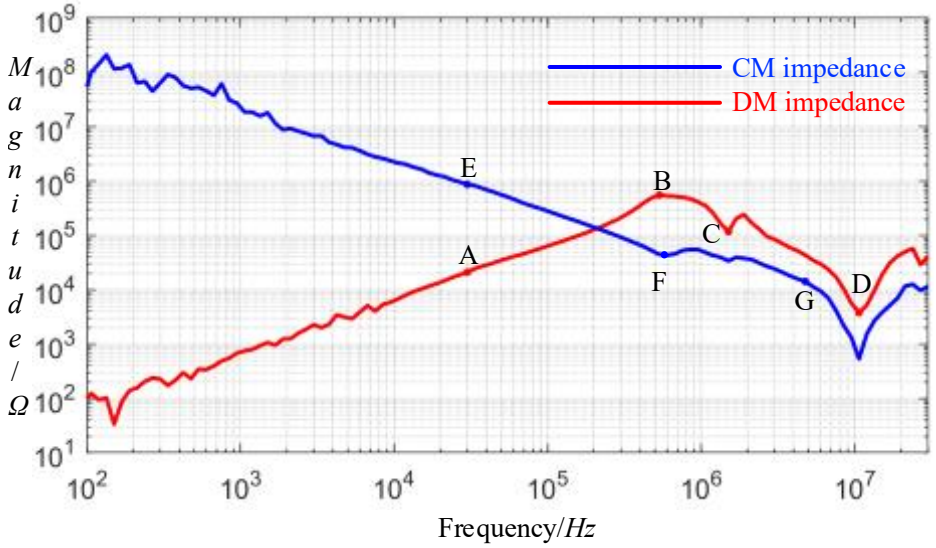


Figure C.1 Common-mode and differential-mode impedance measurement results.

The parameterization results of the high-frequency model are shown in Table C.1.

Table C.1 Model parameterization results.

| Parameter | Result | Parameter | Result |
|---|---|---|---|
| $C_{g1}$ | 371pF | $C_{g2}$ | 662pF |
| $R_{g1}$ | 13.33Ω | $R_{g2}$ | 750Ω |
| $L_d$ | 4.1mH | $R_{e1}$ | 1.8kΩ |
| $R_{ad}$ | 1.4kΩ | $R_{e2}$ | 0.63kΩ |
| $C_{ad}$ | 109pF | $L_c$ | 0.66μA |